

INVESTIGATION AND PREDICTION OF
HURRICANE EYEWALL REPLACEMENT CYCLES

By

Matthew Sitkowski

A dissertation submitted in partial fulfillment of
the requirements for the degree of

Doctor of Philosophy

(Atmospheric and Oceanic Sciences)

at the

UNIVERSITY OF WISCONSIN-MADISON

2012

Date of final oral examination: 4/9/12

The dissertation is approved by the following members of the Final Oral Committee:

James P. Kossin, Affiliate Professor, Atmospheric and Oceanic Sciences

Daniel J. Vimont, Professor, Atmospheric and Oceanic Sciences

Steven A. Ackerman, Professor, Atmospheric and Oceanic Sciences

Jonathan E. Martin, Professor, Atmospheric and Oceanic Sciences

Gregory J. Tripoli, Professor, Atmospheric and Oceanic Sciences

Abstract

Flight-level aircraft data and microwave imagery are analyzed to investigate hurricane secondary eyewall formation and eyewall replacement cycles (ERCs). This work is motivated to provide forecasters with new guidance for predicting and better understanding the impacts of ERCs. A Bayesian probabilistic model that determines the likelihood of secondary eyewall formation and a subsequent ERC is developed. The model is based on environmental and geostationary satellite features. A climatology of secondary eyewall formation is developed; a 13% chance of secondary eyewall formation exists when a hurricane is located over water, and is also utilized by the model. The model has been installed at the National Hurricane Center and has skill in forecasting secondary eyewall formation out to 48 h.

Aircraft reconnaissance data from 24 ERCs are examined to develop a climatology of flight-level structure and intensity changes associated with ERCs. Three phases are identified based on the behavior of the maximum intensity of the hurricane: intensification, weakening and reintensification. Despite a large oscillation of intensity, with a weakening of $\sim 10 \text{ m s}^{-1}$ occurring during most of the ERC, the net intensity change is near zero. However, a broadening of the wind field is observed, and the eye rarely contracts back to the radius prior to the ERC. The expanding storm size increases the storm's integrated kinetic energy.

Thermodynamic fluctuations are also documented during an ERC. Flight-level temperature, dewpoint, relative humidity, and θ_e are all found to increase within the inner-core over the course of an ERC, except for a decrease of mean relative humidity in the moat region. Near the end of an ERC, high values of inertial stability are associated with the relict inner eyewall circulation and create a "containment vessel" that confines the old-eye air mass. This is evident

by the difference in θ_e values (> 10 K) between the old-eye air mass and the adjacent moat at the end of and following an ERC. The relict inner eyewall circulation is found to be an important feature that can impact the secondary circulation of the inner-core, the intensification of the outer eyewall, and the pressure-wind relationship of the storm.

Acknowledgments

No University, it seemed to me, could be more admirably situated, and as I sauntered about it, charmed with its fine lawns and trees and beautiful lakes, and saw the students going and coming with their books, and occasionally practicing with a theodolite in measuring distances, I thought that if I could only join them it would be the greatest joy of life. I was desperately hungry and thirsty for knowledge and willing to endure anything to get it.

– *John Muir describing the University of Wisconsin-Madison*

I arrived at Madison, Wisconsin during the summer of 2007 bringing with me the lessons and wisdoms I acquired from my previous experiences at Florida State University and the University of Hawai'i. I wish to thank Dr. Henry E. Fuelberg and Dr. Gary M. Barnes for providing a solid foundation for my Ph.D. work at the University of Wisconsin-Madison. The support received from the faculty and students at those institutions is also much appreciated. My friends and colleagues at the National Hurricane Center and Honolulu Forecast Office should also be recognized. My experiences with the National Weather Service, which I cherish, were extremely valuable and served as motivation for much of this work.

I am indebted to my current research advisor, Dr. James P. Kossin, for his support and mentorship. He is patient, a great teacher, and a superb scientist. We had numerous, beneficial conversations and he made sure my career aspirations aligned with my research goals. He was committed to my progress and I am very thankful for his guidance and advice. I am also grateful for the many discussions and interactions I have had with my committee members: Drs. Dan Vimont, Steven A. Ackerman, Jonathan Martin, and Greg Tripoli. The department staff also deserves recognition for answering all of my questions answered regarding deadlines, paperwork, and computer support.

A number of colleagues are also deserving of praise, especially Dr. Chris Rozoff. I am a better scientist because of his assistance and teaching skills. Howard Berger, Will Lewis, Chris Velden, Jeff Hawkins, John Knaff, and Mark DeMaria were also a tremendous help during the past 5 years.

Juggling the commitments of a graduate student, research and otherwise, can at times be overwhelming. The support provided by my friends over the years has been a huge part of my successes and accomplishments. My appreciation of their unquestionable loyalty, trust, and honesty cannot be understated. I am very grateful to have met all of them and look forward to the countless memories that lie ahead, especially at Millibar!

I have arrived at this juncture in my life because of the love, encouragement, and support I have received from my family. They are the very best. I love them and thank them for shaping me into the person I am today.

List of Acronyms

AMSR	advanced microwave scanning radiometer
ERC	eyewall replacement cycle
GOES	geostationary operational environmental satellite
HRD	Hurricane Research Division
HURDAT	hurricane data
HURSAT	hurricane satellite
IKE	integrated kinetic energy
JHT	Joint Hurricane Testbed
LMI	lifetime maximum intensity
NASA	National Aeronautics and Space Administration
NCDC	National Climatic Data Center
NHC	National Hurricane Center
NOAA	National Oceanic and Atmospheric Administration
RMW	radius of maximum wind
ROC	relative operating characteristic
SEF	secondary eyewall formation
SHIPS	Statistical Hurricane Intensity Prediction Scheme
SSMI	special sensor microwave imager
TMI	TRMM microwave imager
TRMM	tropical rainfall measuring mission
USAF	United States Air Force

Table of Contents

Abstract	ii
Acknowledgements	iv
List of Acronyms	vi
Table of Contents	vii
List of Tables	ix
List of Figures	x
Chapter 1 Introduction	1
Chapter 2 Secondary Eyewall Formation	8
<i>a.</i> Database	8
<i>b.</i> Climatology.....	10
Chapter 3 Model Development	19
<i>a.</i> Naïve Bayes Classifier.....	20
<i>b.</i> Environmental Features	24
<i>i.</i> Feature Sensitivity	26
Chapter 4 Model Performance	32
<i>a.</i> Diagnostic Model	Error! Bookmark not defined.
<i>i.</i> Optimal Decision Threshold.....	38
<i>b.</i> Operational Model.....	40
Chapter 5 Eyewall Replacement Cycle Database	49
<i>a.</i> Flight-level Dataset.....	50
<i>b.</i> Rankine Fits	52
<i>c.</i> Microwave Imagery Dataset	56

Chapter 6 Kinematic Climatology	59
<i>a.</i> Hurricane Diana 1984.....	59
<i>b.</i> Microwave Imagery.....	62
<i>c.</i> Intensity and Structure Changes	64
<i>i.</i> Multiple Eyewall Replacement Cycles.....	69
<i>ii.</i> Wind Field Expansion	71
Chapter 7 Thermodynamic Analysis	90
Chapter 8 Relict Inner Eyewall Circulation	99
<i>a.</i> Hurricane Wilma	100
Chapter 9 Summary and Outlook	108
Appendix	112
References	116

List of Tables

Table 2.1 Number of North Atlantic hurricanes, major hurricanes, hurricanes that exhibited at least one secondary eyewall during their lifetime, and number of individual SEF events from 1997-2010.	13
Table 3.1 SHIPS features applied to the Bayes probabilistic model in the North Atlantic.	29
Table 4.1 Four 2×2 contingency tables for classification of SEF events in the North Atlantic. The top 2×2 table is based on the climatological probability of SEF. The next table is based on the probability estimated from the new algorithm using current intensity as the sole feature. The next table shows how the inclusion of the SHIPS environmental features improves the algorithm performance. The bottom table is based on the addition of the GOES satellite-derived features. All values are based on cross validation of the model.	43
Table 4.2 Performance metrics of the model applied to the North Atlantic.	43
Table 4.3 2×2 contingency tables for two different decision rules applied to the North Atlantic.	44
Table 4.4 Performance metrics of the model under two decision rules.	44
Table 4.5 Operational brier skill scores.	44
Table 5.1 Start and end times for all 24 ERC events as defined in flight-level aircraft data.	57
Table 6.1 Mean and standard deviations for r_1 , r_2 , v_1 , and v_2 changes during each ERC phase. The mean and standard deviation is also given for the time required to complete each phase, the time to complete an entire ERC, and the amount of time until concentric eyewalls first appear on microwave imagery.	76

List of Figures

- Figure 1.1** Satellite (a) microwave and (b) infrared images of Hurricane Frances near 1710 UTC 30 Aug. 2004. Although not evident in the infrared imagery, concentric convective rings make up the hurricane inner-core. The primary eyewall (marked PE) is weakening while convection in the secondary eyewall (marked SE) is strengthening. The warm (blue) ring between the primary and secondary eyewalls identifies the moat, which is associated with warm and dry subsiding air. 7
- Figure 2.1** Satellite microwave images of Hurricane Frances (2004) taken near (a) 1200 UTC 31 Aug., (b) 1800 UTC 31 Aug., and (c) 0000 UTC 01 Sept. 14
- Figure 2.2** Locations of SEF events in the North Atlantic from 1997-2010. 14
- Figure 2.3** The bar graph displays the percent of SEF events by month from 1997-2010. The percent of major hurricanes per month, regardless of whether SEF occurred, for the same period is shown by the black line. 15
- Figure 2.4** Ratio (%) of SEF hurricanes per month divided by the number of total hurricanes per month. Numbers at the bottom of each column indicate the number of hurricanes per month. Hurricanes that cross from one month to another are counted in both months. 16
- Figure 2.5** Frequency of SEF events binned by mean current intensity during the 12 h period of an event. 17
- Figure 2.6** Climatological probability, based on counts, of SEF as a function of current intensity (grouped by Saffir-Simpson category). The values reflect the climatological probability for any time that a hurricane is over water, that SEF is imminent. 18
- Figure 3.1** Smoothed kernel density estimations for the 12 features used in SEF model. The SEF yes (no) cases appear as a red (blue) line. 30
- Figure 3.2** Posterior probabilities from the controlled experiment when each feature ranges from ± 2 their standard deviations, while the remaining features remain fixed at their mean. The red rings represent the observed maximum and minimum values for each feature from the SHIPS database. 31

Figure 3.3 *Top*, Smoothed kernel density estimation for the SHRD feature, as in Fig. 3.1. *Bottom*, Posterior probabilities from the controlled experiment, as in Fig. 3.2..... 32

Figure 4.1 Attributes diagram for the Bayes probabilistic model for 3 different choices of features: current intensity only (VMX), current intensity plus SHIPS environmental features (VMX plus ENV), and current intensity plus SHIPS environmental features plus infrared-based features (VMX plus ENV plus IR). The posterior probabilities given by the model were placed in 6 bins of varying ranges with each point plotted at the bin center. The bin ranges were chosen *ad hoc* to reduce sampling fluctuations. The counts within each bin, from least to greatest probability, are {633, 454, 325, 43, 1, 3} for VMX only, {1089, 137, 95, 82, 24, 6} for VMX plus ENV, and {1134, 87, 68, 47, 34, 15} for VMX plus ENV plus IR. 45

Figure 4.2 Cumulative probability of the model-estimated probability of imminent SEF using (a) VMX as the sole feature, (b) VMX plus the SHIPS environmental features, and (c) with the final addition of the infrared satellite-based features. Solid curves: probability of SEF assigned to cases that were observed to form secondary eyewalls. Dashed curves: probability of SEF assigned to storms that were *not* observed to form secondary eyewalls..... 46

Figure 4.3 Evolution of current intensity (solid black line, left axis), VMX-model estimated probability of SEF (dashed line, right axis), and VMX plus ENV plus IR model-estimated probability of SEF (stem plot, right axis) in Hurricanes Katrina (2005), Ike (2008), Floyd (1999), and Earl (2005). Probabilities are not assigned when the intensity is less than 65 kt or when the storm center is over land. Each gray shaded region denotes a period that a SEF event was observed within. 47

Figure 4.4 SEF model output as it appears at the end of the SHIPS output text file. SHIPS Guidance was run at 1200 UTC 24 August, when Matt Sitkowski and Chris Rozoff were aboard a NOAA-P3 aircraft in the eye of Hurricane Irene (2011). The probability for SEF over the next 12 h was 29%, which is 7% greater than the intensity-based climatology. Higher probabilities were forecast out to 48 h, with a cumulative probability of 99%. Two SEF events did verify. One was at the time guidance was run, 1200 UTC 24 August, and the other was 54 h later at 1800 UTC 26 August. 48

Figure 4.5 As in Fig. 4.1, but for 4 forecast periods of the 2008-2011 operational model. The counts within each bin, from least to greatest probability, are roughly {1235, 95, 20, 20, 12}... 48

Figure 5.1 a) A double modified Rankine vortex with all eight parameters labeled. The radius is from storm center. b) A complete profile (inbound and outbound radial legs) of tangential wind (gray line) for Hurricane Gilbert (1988). The inbound pass is fit with a double modified Rankine

vortex, capturing both wind maxima. The outbound pass is fit with a single modified Rankine vortex which only allows for the detection of a single wind maximum. 58

Figure 5.2 A complete profile (inbound and outbound radial legs) of tangential wind for Hurricane Frances (2004). Three wind maxima, identified by number, are observed for each leg. The aircraft was near the storm center at 1815 UTC 30 August. The radius is from storm center. 58

Figure 6.1 *Top panel:* The evolution of radii parameters r_1 (red) and r_2 (blue). *Bottom panel:* The evolution of intensity parameters v_1 (red) and v_2 (blue) for Hurricane Diana (1984). 77

Figure 6.2 As in Fig. 6.1, but only during the ERC. Each time series of wind profile parameters is fit with a polynomial best fit (solid lines). Vertical dashed lines separate phases of the ERC, determined from the evolution of the maximum intensity. 78

Figure 6.3 *Top,* as in Fig. 6.2, but for a Hurricane Floyd (1999) ERC. The lettered vertical lines correspond to the times when the inner-core was observed by microwave instrumentation. *Bottom panel,* 300 x 300 km storm-centered 85 GHz SSM/I imagery of brightness temperatures (K) taken at *a)* 2340 UTC 12 September, *b)* 2240 UTC 13 September, and *c)* 2228 UTC 14 September for Hurricane Floyd (1999). White range rings denote radial distances from storm center of 50, 100, and 150 km. 79

Figure 6.4 a) Composite analysis of intensity changes associated with the inner wind maximum (v_1 , solid black line) and outer wind maximum (v_2 , dashed black line) for 24 ERC events. The ERC is broken into 3 phases: intensification, weakening, and reintensification. Associated with each ERC phase are vertical boxplots depicting the spread of the intensity changes, in m s^{-1} , for each phase. Horizontal boxplots depict the range of time (h) associated with each phase. The bottom horizontal boxplot represents the range of time required to complete an entire ERC. The red M is the average of the best estimated time when double eyewalls with a well-defined moat first appear on microwave imagery after an outer wind maximum has been detected. b) As in (a), but for radii changes of r_1 and r_2 measured in km. 80

Figure 6.5 Schematic of the maximum intensity evolution during 3 phases of an ERC. The average amount of time to complete each phase, along with the average values of the Rankine parameters, as determined from the third-order polynomial fits, are listed for the start and end of the ERC, as well as the transition of phases. 81

Figure 6.6 a) Composite analysis of the intensity changes associated with the inner wind maximum (solid black line) and outer wind maximum (dashed black line) for 24 ERC events for all three ERC phases. The black lines are identical to those that appear in Fig. 6.4. The solid red

line and dashed red line mark the intensity changes for inner and outer wind maximum changes respectively for a single ERC during Ivan (2004) that occurred on 11 and 12 September. The black M is the average of the best estimated time when double eyewalls with a well-defined moat first appear on microwave imagery after an outer wind maximum has been detected. The red M represents when double eyewalls are estimated to have first appeared on microwave imagery for this particular Ivan ERC. b) As in a, but for radii..... 82

Figure 6.7 A phase diagram of r_1/r_2 versus v_1/v_2 for 24 ERC cases. The entire polynomial fits of the Rankine parameters are used. Shading represents the density (%) of an ERC event passing through an existing radius ratio and intensity ratio pair. The red, green, and blue portion of each line represents the intensification, weakening, and reintensification phases respectively. Black dots and X's indicate the start and end time an ERC..... 83

Figure 6.8 Evolution of Rankine parameters r_1 (red dots) and r_2 (blue dots) for Hurricane Ivan (2004). Green dots indicate the location of triple wind maxima. Black lines are linear interpolations of the inner radius, r_1 . The dotted line captures the contraction of r_1 and the solid black line highlights the jump in eye size associated with the transitioning of the outer wind maximum to the primary wind maximum. 84

Figure 6.9 As in Fig. 6.3, but for an ERC in Hurricane Ivan (2004). *Top*, the green dots represent the radius (top panel) and intensity (bottom panel) of the decaying innermost eyewall. *Bottom*, Microwave images are from 1828 UTC 10 September (AMSRE), 1348 UTC 11 September (TMI), and 1252 UTC 12 September (TMI)..... 85

Figure 6.10 Hovmöller diagram of flight-level radial profiles of tangential wind for Hurricane Ivan (2004) during the month of September. Radial leg profiles extend from storm center (0 km) out to 150 km. Time increases toward the origin on the y-axis..... 86

Figure 6.11 Composite analysis of flight-level radial legs and for each of the 3 phases of an ERC and their corresponding IKE values. The dashed line represents hurricane intensity, 33 m s^{-1} . .. 87

Figure 6.12 Comparison of intensity changes associated with ERCs and a climatology of hurricane intensity changes. The black line represents the difference between the mean pre-SEF profile, all available radial legs 12 h before SEF, compared with the mean post-SEF profile, all available radial legs 12 h after SEF for 15 10 km bins. The 15 boxplots display the distribution of 5000 random hurricane intensity changes that followed the same procedure, i.e. 5000 random times were selected and all available radial legs 12 h before and after this time were used in the analysis..... 88

Figure 6.13 a) As in Fig. 6.10 but for Hurricane Wilma (2005) during the month of October. b) Evolution of Wilma (2005) flight-level intensity (dashed line) and IKE (solid line). Time increases toward the origin on the y-axis. 95% of data from each radial leg was required to calculate IKE. Gray boxes indicate when Wilma was over land. 89

Figure 7.1 Storm-centered 85 GHz imagery of brightness temperatures (K) of Hurricane Ioke (2006) taken at (a) 1455 UTC 01 Sep. (AMSR-E) and (b) 0924 UTC 02 Sep. (TRMM-TMI). The typical changes in the convective presentation of the inner-core during an ERC and its relationship to the three regions are shown. The letters E, M, and F represent the eye, moat, and far-field regions respectively. The relict inner eyewall circulation (contained within the white dashed ring) and moat region together make up the developing post-ERC eye..... 95

Figure 7.2 Comparisons of flight-level thermodynamic data at the start and end of the 24 SKR11 ERCs. All plots are based on the mean flight-level measurements along the 700 mb level within each region. For each region, the boxplot on the left (right) is based on the first (last) 3 h of the ERC. The medians at the start and end of an ERC in each region are significantly different at the 5% significance level if the widths of the notches centered on the medians do not overlap. The blue diamond represents the mean of the data. The four panels show changes in flight-level (a) temperature, (b) dewpoint, (c) relative humidity, and (d) θ_e 96

Figure 7.3 Comparisons of flight-level (700 mb) composite temperature (red) and dewpoint (blue) profiles. The solid (dashed) line indicated that v_1 (v_2) was the maximum intensity of the radial leg. The profiles are normalized by r_1 97

Figure 7.4 Hurricane Rita (2005) flight-level measurements along the 700 mb level from storm center out to 75 km. The top panels display tangential wind (gray) and θ_e (black). The bottom panels display temperature (red), dewpoint (blue) and inertial stability (black). Measurements were taken during the (a) intensification phase at 1937 UTC 21 Sep. (the inertial stability near storm center exceeds the maximum value of the y-axis), (b) weakening phase at 1619 UTC 22 Sep., (c) reintensification phase at 0145 UTC 23 Sep., and (d) post-ERC period at 0600 UTC 23 Sep. 98

Figure 8.1 (a) Hurricane Wilma (2005) flight-level measurements along the 700 mb level taken near 0834 UTC 20 Oct. *Top*, tangential wind (gray) and θ_e (black). *Middle*, tangential wind (gray) and inertial stability (black). Inertial stability near storm center exceeds the maximum value of the y-axis. *Bottom*, temperature, dewpoint, and tangential wind appear as red, blue and gray lines respectively. A small portion of thermodynamic data from 30-50 km contained large wetting errors and were removed. (b) As in (a), but for 1020 UTC 20 Oct..... 104

Figure 8.2 Hurricane Wilma (2005) flight-level (700 mb) tangential wind (gray line) and surface pressure (black line). The aircraft was near storm center at (a) 2140 UTC 19 Oct., (b) 0650 UTC 20 Oct., (c) 1020 UTC 20 Oct., and (d) 2017 UTC 20 Oct. As noted in the text, the actual surface pressure is likely lower than shown here. 105

Figure 8.3 300 x 300 km storm-centered 85 GHz imagery of brightness temperatures (K) of Wilma (2005) taken at (a) 0152 UTC 20 Oct. (TRMM-TMI), (b) 1845 UTC 20 Oct. (AMSR-E), and (c) 0056 UTC 21 Oct. (TRMM-TMI). White range rings denote radial distances from storm center of 50, 100, and 150 km..... 106

Figure 8.4 (a) As in Fig. 8.1, but for 2017 UTC 20 Oct. (b), As in Fig. 8.1. but for 1011 UTC 21 Oct..... 107

Figure 9.1 Number of times the word ‘hurricane’ and ‘eyewall’ have appeared in the abstract of American Meteorological Society journals. The counts cover 12 pentads..... 111

Chapter 1 Introduction

Suddenly we broke into the eye of the storm. This was not the purpose of the flight, but really an accident. The sky was filled with bright clouds and it seemed that we were surrounded by a shower curtain of darker clouds. We looked down and could see the country side. The storm had indeed moved inland.

– *Lt. Colonel Ralph O’Hair, recalling the first-ever flight into a hurricane.*

On the morning of July 27, 1943 Colonel Joe Duckworth received reports that a hurricane was approaching the Texas coast. When he ordered that the AT-6 Texan aircraft be moved to a hanger for shelter during the storm a group of visiting British pilots, in town for “instrument flying” training, questioned the construction of the aircraft. Willing to prove the capability of his fleet, Col. Duckworth persuaded a reluctant navigator Lt. Ralph O’Hair to join him for what turned out to be the first successful flight into the eye of a hurricane. Upon safely returning to Bryan Field, just outside College Station, TX, the base's weather officer insisted he be given the same ride into the eye. The completion of a 2nd flight that day marked the beginning of routine hurricane reconnaissance. By 1946 the United States Navy Weather Reconnaissance Squadron was already referred to as the “Hurricane Hunters”.

Today, the United States Air Force (USAF) and National Oceanic and Atmospheric Administration (NOAA) continue hurricane reconnaissance flights. The data collected during these flights have become an integral component of hurricane forecasting and research. Typically, aircraft fly an alpha pattern that enables sampling of all quadrants within ~200 km of storm center. Onboard radar is used to avoid the fierce convection and turbulence of the eyewall, where the most intense winds are usually located. Occasionally, aircraft encounter spiral

rainbands with active convection far from the eyewall. In an intense hurricane, this convection often organizes into a coherent ring, eventually forming a secondary, outer eyewall.

Secondary eyewalls are generally identified as quasi-circular rings of convective cloud at some distance outward from, and roughly concentric with, the primary eyewall of a hurricane (Fig. 1.1a). Secondary wind maxima are often, but not always, collocated with the convective ring (Samsury and Zipser 1995), analogous to the collocation of the peak winds in a hurricane and the convection in the primary eyewall. The seminal work by Willoughby et al. (1982) explored the axisymmetric physics of secondary eyewall formation (SEF) and the replacement of the primary eyewall by a contraction of the secondary eyewall that often follows its formation. The process of SEF and the replacement of the primary eyewall by the secondary eyewall are typically referred to as an “eyewall replacement cycle” (ERC).

The motivation to understand and forecast ERCs is high, as they can have very serious consequences arising from dramatic intensity and structure changes within the hurricane. ERCs often produce an oscillation of the hurricane’s maximum intensity while serving as a mechanism for storm growth and an increase of integrated kinetic energy (IKE; Maclay et al. 2008). A sudden expansion of hurricane force winds near landfall can impact a larger coastal area while reducing preparation time. When a hurricane is further from shore, an increased hurricane wind field is likely to lead to a greater storm surge due to increased wind fetch (Irish et al. 2008). One of the most damaging direct effects of Hurricane Katrina (2005) was the storm surge resulting from the unusually broad region of significant winds surrounding the eye after the completion of an ERC. For comparison, the storm surge associated with the landfall of very small and compact Hurricane Charley (2004) was much less damaging despite having much greater peak winds than Katrina at landfall. Additionally, the contraction of an outer eyewall near the end of an ERC can

sometimes lead to rapid intensification resulting in a more intense hurricane than when the ERC began. At great cost to life and property, Hurricane Andrew (1992) unexpectedly strengthened to a Category 5 hurricane while making landfall in southeastern Florida immediately following an eyewall replacement event (Willoughby and Black 1996; Landsea et al. 2004).

Microwave instrumentation aboard polar orbiting satellites provides a view of the inner-core convective structure of a hurricane. This allows for the identification of SEF that would have previously been masked by a cirrus canopy. These microwave images and an expanding collection of aircraft data, have revealed that ERCs occur often, especially for major hurricanes (e.g., Hawkins et al. 2006) and recent work has documented their behavior. Hawkins and Helveston (2008) outlined a variety of common inner-core structure changes that can occur with ERCs in intense (> 120 kt) tropical cyclones, including the ‘classic’ ERC evolution laid out by Willoughby et al. (1982), the possibility for multiple ERCs for a single storm, the existence of a double eyewall configuration that lasts for days, and the transitioning of the storm to an annular eyewall configuration (Knaff et al. 2003). Kuo et al. (2009) used microwave data and the “best-track”, a record of 6 h tropical cyclone location and maximum intensity estimates during the entire lifetime of a tropical cyclone (HURDAT; Jarvinen et al. 1984) to examine the intensity changes associated with ERCs and characteristics of the moat of low-echo reflectivity between concentric eyewalls. Like many previous observational studies (Willoughby et al. 1982; Willoughby 1988; Willoughby 1990; Hawkins et al. 2006; Black and Willoughby 1992; Houze et al. 2006; Houze et al. 2007; Dodge et al. 1999), they found that concentric eyewalls can have a profound impact on a tropical cyclone’s intensity and that there is large variability associated with the intensity changes.

A complete description of the physics responsible for SEF and ERCs has not yet been established despite successful theoretical and numerical modeling experiments (e.g., Zhang et al. 2005; Wang 2008a, b; Wang 2009; Hogsett and Zhang 2009; Zhou and Wang 2009; Hill and Lackmann 2009; Qiu et al. 2010; Judt and Chen 2010; Fang and Zhang 2011; Martinez et al. 2011; Abarca and Corbosiero 2011). One physical explanation focuses on small-scale disturbances, or “vortex Rossby waves”, that develop as a result of the horizontal shear at the primary eyewall (Montgomery and Kallenbach 1997; Terwey and Montgomery 2008; Abarca and Corbosiero 2011; Martinez et al. 2010). A new outer eyewall may develop when these disturbances become phase locked with the horizontal wind of the hurricane, grow, and propagate radially outward to a critical radius where angular momentum may concentrate and coalesce.

Other studies suggest that large-scale environmental conditions, such as relative humidity, can affect the orientation of spiral rainbands, which may merge together and lead to a second eyewall formation (Nong and Emanuel 2003; Hill and Lackmann 2009; Wang 2009; Kossin and Sitkowski 2009). The spiral rainbands eventually organize into a ring and form a “moat” between the primary and secondary eyewalls (Fig. 1.1a). The moat region is characterized by subsiding air, little if any precipitation, and strain-dominated flow (Rozoff et al. 2006, 2008). The characteristics of the moat, along with the intensity of the hurricane, are dependent on the evolutions of the transverse circulations¹ of both the primary and secondary eyewalls (Dodge et al. 1999; Kossin et al. 2000; Camp and Montgomery 2001; Zhu et al. 2004; Wu et al. 2006; Terwey and Montgomery 2006; Houze et al. 2007; Rozoff et al. 2008; Wang

¹ The transverse circulation in a tropical cyclone describes the combination of radial (toward/away from storm center) and vertical (ascent/subsidence) air flow.

2008a). The disruption of the primary, inner eyewall transverse circulation likely plays a role in its demise. Willoughby et al. (1982) and Willoughby (1988) theorized that a portion of the outer eyewall's transverse circulation moves inward toward the storm's center at upper levels and impinges on the outflow of the inner eyewall. In an alternative hypothesis, Rozoff et al. (2008) derived an analytical solution of the transverse circulation equation associated with a balanced vortex model and showed that the inertial stability of the developing outer eyewall impedes the outflow from the inner eyewall, which they hypothesized would reduce inner eyewall convection. Similarly, Rappin et al. (2011) found that weaker intensification rates occur when a storm's outflow interacts with a region of high inertial stability.

Near the end of an ERC, as the outer eyewall transitions to a larger, primary eyewall its transverse circulation seems to be impacted by the high inertial stability of the decaying inner eyewall, or relict inner eyewall circulation. This feature lingers in the larger post-ERC eye and may appear to be an unimportant residual of an ERC, but observational analysis and model results suggest this feature can play an important role in the evolution of a hurricane inner-core (Zhu et al. 2004; Chen et al. 2011; Zhou and Wang 2009, 2011).

Despite their dramatic impact on the intensity and structure evolution of the inner-core, Kossin and Sitkowski (2009) provide the only objective guidance to forecast SEF and ensuing ERCs. They developed a climatology of SEF events in the North Atlantic basin and used this information, in combination with current intensity and large-scale environmental conditions near the time of SEF, to develop a Bayesian probabilistic model that alerts forecasters when SEF is imminent. Chapters 2-4 review this work, discuss recent updates, and assess the most recent skill of the model. As ERC research progresses, detailed documentation of in-situ measured intensity

and structure changes associated with ERCs is highly desirable. To address this need and supplement the Bayesian model, chapters 5-6 discuss the creation of a flight-level dataset that was utilized to develop a climatology of intensity and structure changes associated with ERCs. Chapter 7 presents an analysis of flight-level thermodynamics of ERCs and chapter 8 explains the ramifications of the relict inner eyewall circulation on the evolution of the inner core. A summary and outlook appears in chapter 9.

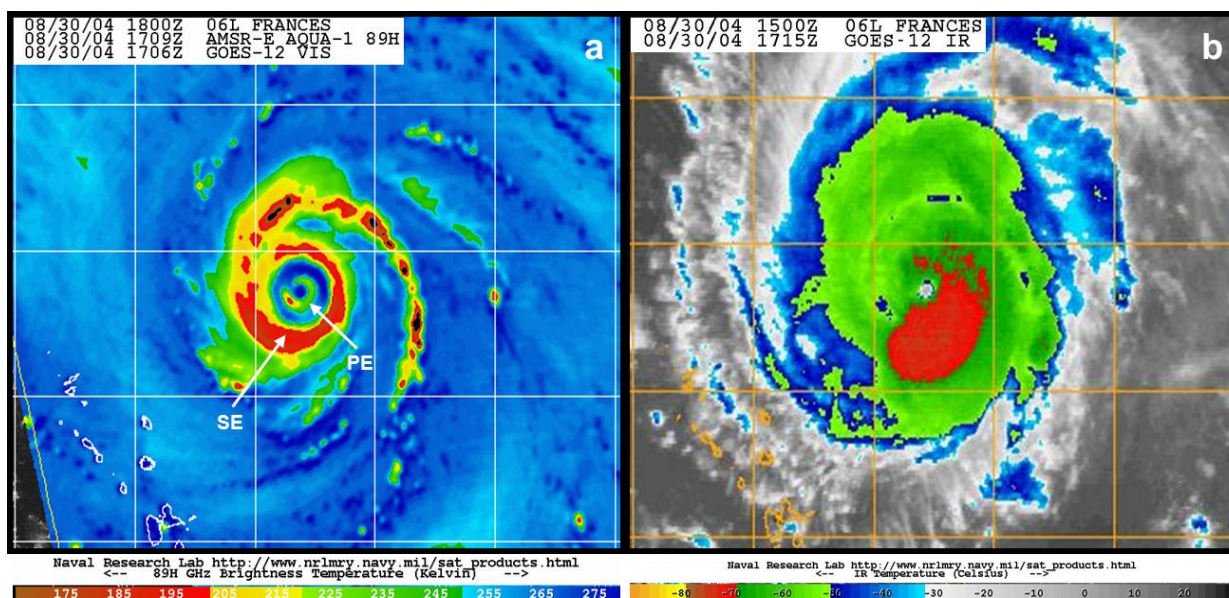


Figure 1.1 Satellite (a) microwave and (b) infrared images of Hurricane Frances near 1710 UTC 30 Aug. 2004. Although not evident in the infrared imagery, concentric convective rings make up the hurricane inner-core. The primary eyewall (marked PE) is weakening while convection in the secondary eyewall (marked SE) is strengthening. The warm (blue) ring between the primary and secondary eyewalls identifies the moat, which is associated with warm and dry subsiding air.

Chapter 2 Secondary Eyewall Formation

Of course... internal dynamics also play a role in what the intensity of a hurricane will be... and we have no skill in forecasting eyewall replacement cycles beyond about 6-12 hours... at best.

- *Stacy Stewart, Hurricane Specialist*
National Hurricane Center Hurricane Rita Discussion
11 p.m. EDT Wed. Sep. 21, 2005

The formation of a secondary eyewall in a tropical cyclone was first described more than 50 years ago by Fortner (1958) for the case of Typhoon Sarah (1956). Project STORMFURY, a research program from the early 60's through the early 80's, investigated hurricane modification and elevated the interest and importance of studying SEF and ERCs (Willoughby et al. 1985). Several studies have since concluded that ERCs have profound impacts on the structure and intensity of a hurricane. Objective guidance to diagnose or forecast these phenomena did not exist until Kossin & Sitkowski (2009) developed a naïve Bayes probabilistic model to determine the likelihood of imminent SEF. This chapter discusses an essential component of the SEF model, the construction of an SEF database and development of a climatology.

***a.* Database**

Identification of a SEF event is typically a subjective assessment that depends primarily on the structure of convective elements within a hurricane inner-core. Microwave imagery is the most common platform for identifying SEF because the instrumentation aboard polar orbiting satellites has the capability to view the inner-core convective structure beneath a cirrus canopy that would otherwise be obscured in visible or infrared satellite imagery (Fig. 1.1). Over 4,000

microwave satellite images from over 50 hurricanes (available at the website of the Naval Research Laboratory in Monterey, CA) covering the period 1997–2010 were examined in this study. Since SEF has never been observed in a tropical storm or over land, only hurricanes centered over water are considered in this study (cf. Hawkins and Helveston 2004; Hawkins et al. 2006). Here, an event is described by the occurrence of SEF, but there is no guarantee that these events are always followed by a complete ERC. Occasionally, a secondary eyewall was explicitly identified in an aircraft vortex message, NHC forecast statement, or was clearly visible on radar imagery. These reports and observations were also used in developing the database.

There is presently no formal objective definition of what constitutes a SEF event. Key features such as the symmetry and completeness of a convective ring and how well separated it is from the primary eyewall are considered. This work requires a convective ring to be roughly “closed,” that is, the convection had to form at least 75% of a complete circle. Well-defined moats with warm brightness temperatures were also helpful in identifying SEF events. Given the highly variable temporal sampling of satellite microwave and aircraft data and the fact that SEF is not an instantaneous event, determining the exact time of SEF is not a realistic expectation. Here an attempt is made to identify when these events are “imminent”, which in this case means that a secondary eyewall formed at *some* time in the following 12 hours. The starts of these events are also anchored to synoptic times to exploit the existing developmental dataset constructed for the Statistical Hurricane Intensity Prediction Scheme (SHIPS; DeMaria and Kaplan 1994, 1999). The SHIPS dataset generally describes the mean axisymmetric environmental conditions centered on each hurricane, and contains information about the infrared satellite presentation of the storms deduced from Geostationary Operational Earth

Satellites (GOES) (DeMaria et al. 2005). The SHIPS features are available every 6 h during the lifetime of each storm.

Three microwave images of Hurricane Frances (2004) taken near 1200 UTC 31 Aug., 1800 UTC 31 Aug., and 0000 UTC 01 Sept. are shown to illustrate the microwave structure for one SEF event. Even though the final image taken at 0000 UTC 01 Sept. is the only image with a clear double eyewall structure all 3 times constitute one SEF event (Fig. 2.1). During this period, however, outer wind maxima are prevalent in the flight-level data and this 12 h time range appears to be an adequate length to capture the development of a coherent outer wind maximum. A comparison of flight-level data and microwave imagery is discussed in chapter 6.

***b.* Climatology**

The SEF database constructed for the North Atlantic contains 66 unique SEF events during the 14-year period (Table 2.1). Each year contained an event and one-third of all hurricanes developed a secondary eyewall at least once during their lifetime. Comparatively, 78% of major hurricanes (Saffir-Simpson Category 3–5) were observed to form secondary eyewalls at least once during their lifetimes. The high number of individual events in 2004 is largely due to the multiple-formation events observed in Hurricanes Ivan and Frances, both of which were long-lived Cape Verde systems. The locations of SEF² are plotted in Fig. 2.2. There does not appear to be a favored location for SEF, but nearly all of the events occur west of 30° W and south of 30° N (Fig. 2.2).

In the period 1997–2010, secondary eyewalls were observed to form during each month of the hurricane season with September containing more than half of all events (Fig. 2.3). The

² The final synoptic time of the 12 h range of SEF is used as an instantaneous SEF time. For example, the SEF time for Frances in Fig. 2.1 is 0000 UTC 01 Sept.

monthly distribution is very similar to the distribution of major hurricanes during the season and highlights the role of storm intensity on the formation of a secondary eyewall (Fig. 2.3). When the number of hurricanes per month that formed secondary eyewalls is normalized by the number of hurricanes per month, the percentage of hurricanes that form secondary eyewalls ranges from about 20% in November to about 43% in July (this ignores the 100% in June, which only contained one hurricane that contained an SEF event) (Fig. 2.4). That is, a hurricane is apparently more likely to form a secondary eyewall in July or September (38%) than in any other month.

The high July percentage may indicate systematically more favorable environmental conditions in that month, but this is unclear given the constraints of our dataset. The mean maximum lifetime intensities for July hurricanes is lower (~89 kt) than August, September, and October, which are all around 100 kt. This suggests that the environmental conditions in July may be more favorable for SEF than during the most active portion of the hurricane season. The small sample size in July (only 9 hurricanes and 4 that formed a secondary eyewall over the 14-yr period) may not be representative of the larger population that is being sampled from, and the meaning of the relatively high percentage of SEF hurricanes in July should be considered with caution.

The 66 SEF events consist of 196 6-hourly best-track data points in which SEF occurred at some time in the following 12 hours while the hurricane remained over water. Similarly, there were 1,196 fixes at hurricane intensity and over water, but no secondary eyewall formed in the following 12 hours. The range of intensities for these 66 events was broad (Fig. 2.5), but 65% of

SEF intensities were greater than or equal to 100 kt. The average intensity during an event was 111 kt (57 m s^{-1}), which denotes a strong Saffir-Simpson Category-3 hurricane.

When the ratio of the best-track data point for the two classes, the occurrence and non-occurrence of SEF, are grouped by Saffir-Simpson category we find that the intensity of the storm is linked strongly with the occurrence of SEF events. The probability of imminent SEF at any time during Category-5 status is about 53%, so that it is more likely than not that an event is about to occur (if an event is not already underway) (Fig. 2.6). This probability is reduced to about 33% for Category-4 hurricanes, 23% for Category-3 hurricanes, 10% for Category-2 hurricanes, and is less than 5% for Category-1 hurricanes (Fig. 2.6). The probability of any hurricane is 13%. This is the climatology applied to the Kossin and Sitkowski (2009) model, which is discussed in the next two chapters.

Table 2.1 Number of North Atlantic hurricanes, major hurricanes, hurricanes that exhibited at least one secondary eyewall during their lifetime, and number of individual SEF events from 1997-2010.

Year	Hurricanes	Major Hurricanes	SEF Hurricanes	SEF Events
1997	3	1	2	3
1998	10	3	3	3
1999	8	5	2	3
2000	8	3	1	1
2001	9	4	3	3
2002	4	2	2	2
2003	7	3	2	4
2004	9	6	5	16
2005	15	7	5	9
2006	5	2	1	1
2007	6	2	2	5
2008	8	5	3	4
2009	13	2	2	3
2010	12	5	6	9
Total	107	50	39	66

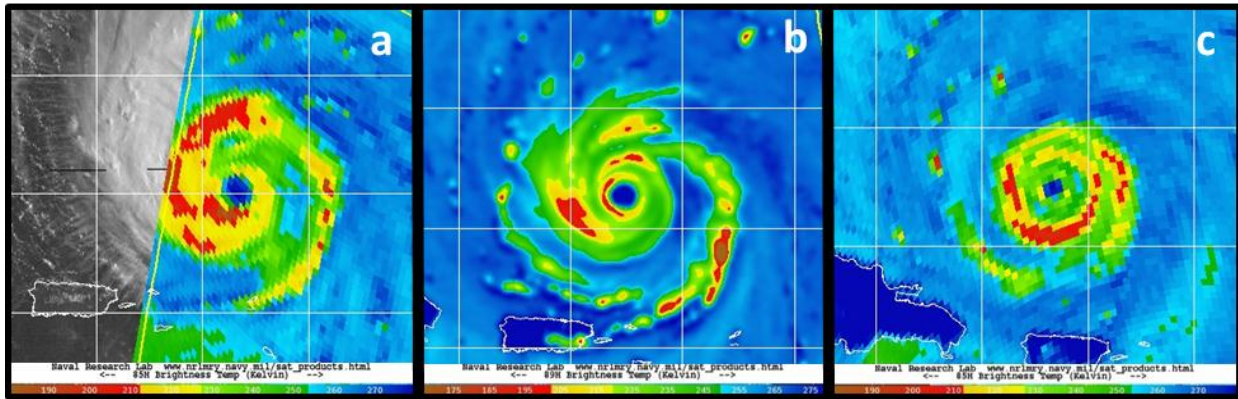


Figure 2.1 Satellite microwave images of Hurricane Frances (2004) taken near (a) 1200 UTC 31 Aug., (b) 1800 UTC 31 Aug., and (c) 0000 UTC 01 Sept.

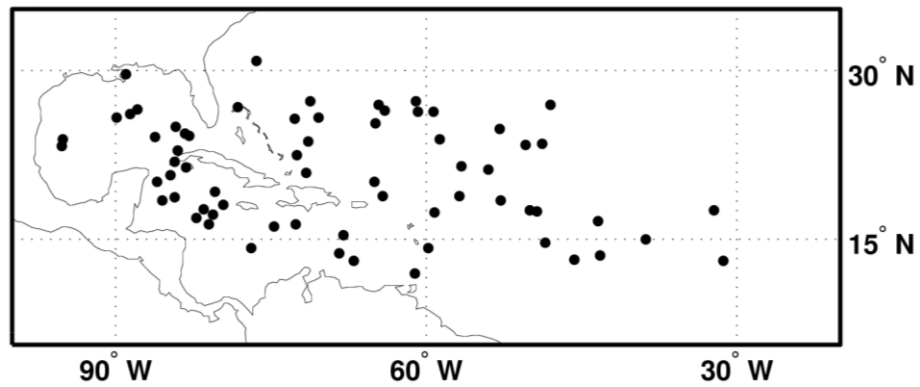


Figure 2.2 Locations of SEF events in the North Atlantic from 1997-2010.

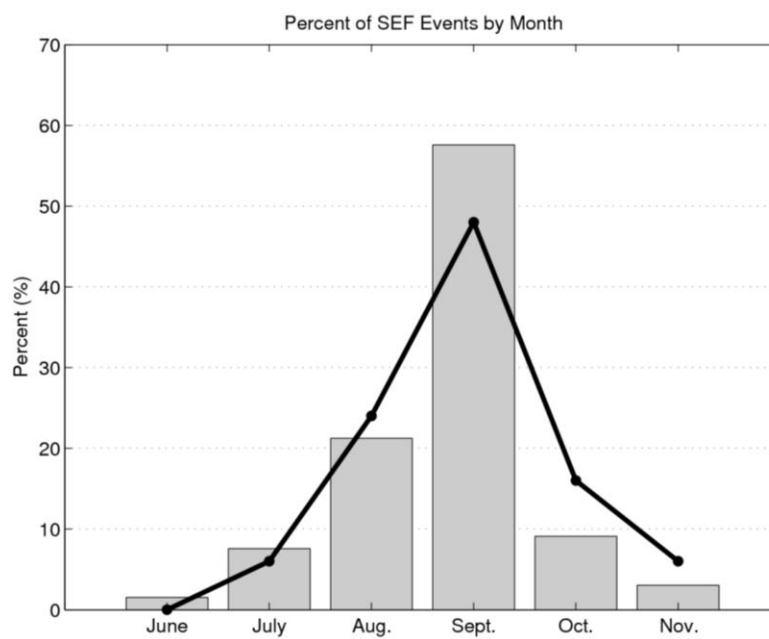


Figure 2.3 The bar graph displays the percent of SEF events by month from 1997-2010. The percent of major hurricanes per month, regardless of whether SEF occurred, for the same period is shown by the black line.

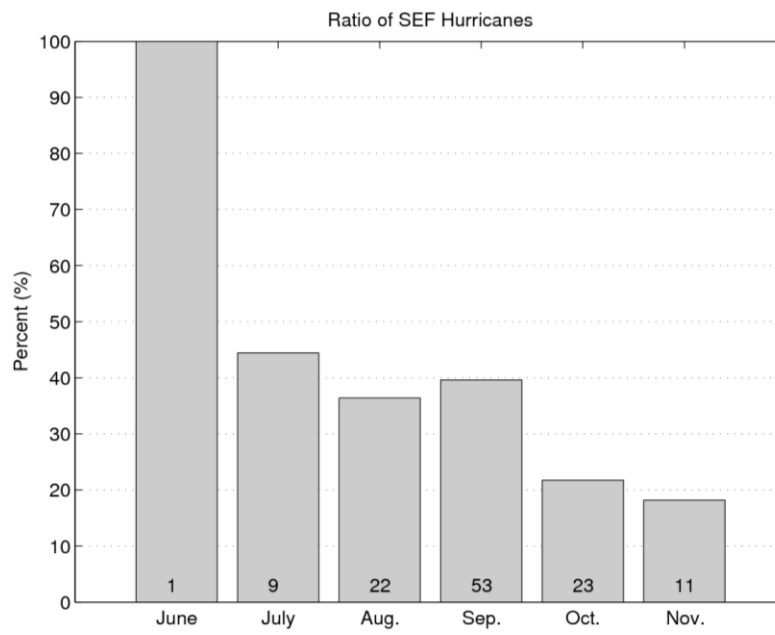


Figure 2.4 Ratio (%) of SEF hurricanes per month divided by the number of total hurricanes per month. Numbers at the bottom of each column indicate the number of hurricanes per month. Hurricanes that cross from one month to another are counted in both months.

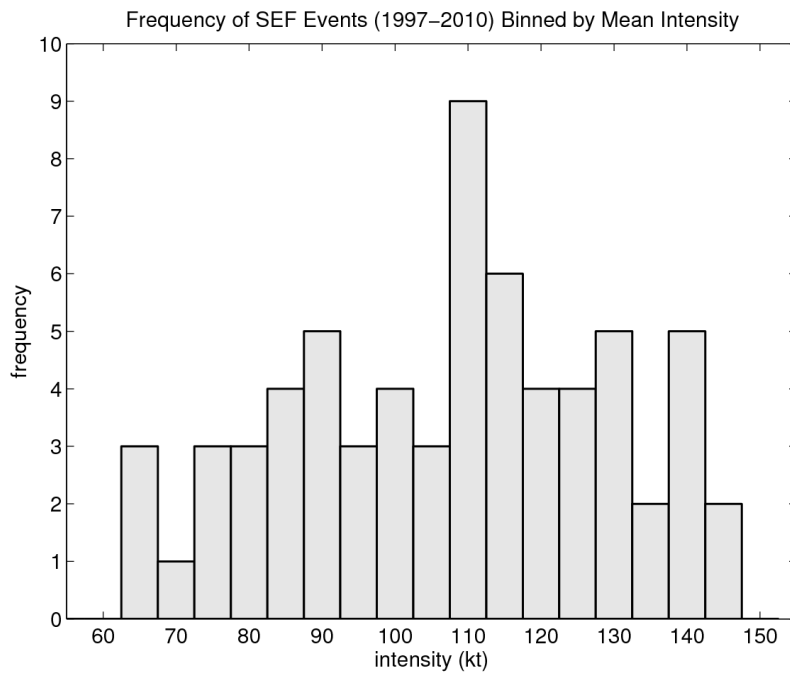


Figure 2.5 Frequency of SEF events binned by mean current intensity during the 12 h period of an event.

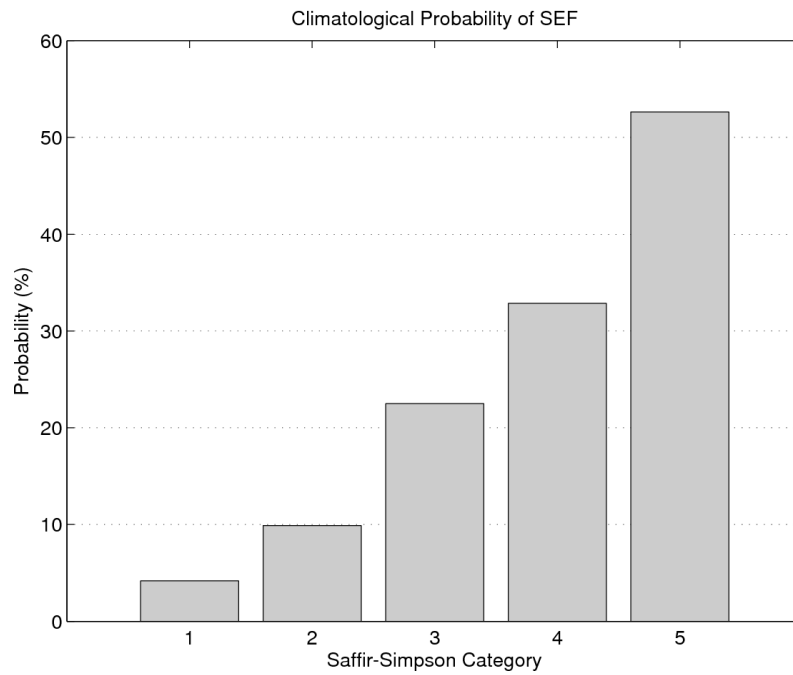


Figure 2.6 Climatological probability, based on counts, of SEF as a function of current intensity (grouped by Saffir-Simpson category). The values reflect the climatological probability for any time that a hurricane is over water, that SEF is imminent.

Chapter 3 Model Development

Prediction is very difficult, especially about the future.

– *Niels Bohr, Danish physicist (1885 – 1962).*

In this chapter, observed storm-centered environmental conditions that are associated with the formation of secondary eyewalls are utilized to construct a diagnostic/predictive algorithm based on a Bayesian probabilistic model. The climatology that was calculated in the previous chapter provides a necessary baseline against which the skill of the model will be evaluated.

There is some debate on the role of environmental conditions versus internal dynamics in controlling SEF events. Nong and Emanuel (2003) argue that SEF requires some external forcing from the ambient environment of the storm, and that once initiated, the survival of the nascent outer eyewall further depends on the ambient environmental conditions. Asymmetries in the storm's ambient environment may contribute to SEF through axisymmetrization processes (Kuo et al. 2004) and internal dynamics in the form of outward propagating vortex Rossby waves may play a role (Montgomery and Kallenbach 1997) in the formation of an secondary eyewall. Molinari and Vollaro (1989) suggest that SEF in Hurricane Elena (1984) might have been forced by interactions with upper-level momentum sources in the environment that the storm was moving into. Terwey and Montgomery (2006) argue that SEF can be initiated in a steady and homogeneous environment in the absence of a coherent external forcing. In this case, the environment may still modulate SEF, but without the presence of asymmetries, and without the occurrence of temporal changes.

In this study, the assumption is made that internal dynamics such as Rossby wave forcing and axisymmetrization processes occur quasi-uniformly via convective forcing in the primary eyewall, and the ambient hurricane environment then modulates whether this forcing is realized in the initiation of a secondary eyewall.

***a.* Naïve Bayes Classifier**

The algorithm is based on application of the SHIPS features using a “naïve Bayes” probabilistic model and classifier (Zhang 2006; Domingos and Pazzani 1997). The model provides a conditional probability of class membership that depends on a set of measurable features. Two classes, C_{yes} and C_{no} , represent the occurrence or absence of SEF respectively. The set of features is expressed as a vector \mathbf{F} of length N (i.e., N is the number of features in the set). Using Bayes’ theorem³, the probability of SEF conditional on the features \mathbf{F} (or, equivalently, the probability of SEF when a particular set of features \mathbf{F} is observed) can be described by

$$P(C_{\text{yes}}|\mathbf{F}) = \frac{P(C_{\text{yes}})P(\mathbf{F}|C_{\text{yes}})}{P(\mathbf{F})} . \quad (3.1)$$

The output of the model, $P(C_{\text{yes}} | \mathbf{F})$, is typically referred to as the “posterior probability”. The “prior probability” $P(C_{\text{yes}})$ is the climatology that was presented in chapter 2 and is the number of C_{yes} cases divided by the total number of cases ($C_{\text{yes}} + C_{\text{no}}$). If no other information was available the posterior probability would always be assigned a 13% probability that SEF will occur in the next 12 h whenever a hurricane is over water. It is this defined climatology that our algorithm must out-perform to be skillful. The skill of the model is discussed in chapter 4.

³ Further detail on Bayes’ theorem and a meteorological application can be found in Wilks (2006). There is also an excellent discussion in Bishop (1995) using an example of text classification.

The likelihood of observing the feature set \mathbf{F} when SEF is imminent is described by the factor $P(\mathbf{F} | C_{\text{yes}})$ in equation (3.1). This is referred to as a “class-conditional probability”. For comparison, the factor $P(\mathbf{F})$ in equation (3.1) gives the probability of observing the set of features \mathbf{F} regardless of class membership. Formulating the probability density functions that will provide values for the class-conditional probability $P(\mathbf{F} | C_{\text{yes}})$ and the analogous expression $P(\mathbf{F} | C_{\text{no}})$ constitutes the “supervised learning” (training) part of the algorithm construction. These probability density functions are noted in lower-case as $p(\mathbf{F} | C_{\text{yes}})$ and $p(\mathbf{F} | C_{\text{no}})$.

The feature set \mathbf{F} can be described as points in an N -dimensional space (e.g., a scatter plot when $N = 2$), and the probability density functions $p(\mathbf{F} | C_{\text{yes}})$ and $p(\mathbf{F} | C_{\text{no}})$ that need to be constructed are thus also N -dimensional. Determining likelihoods of the points in this N -dimensional space can be performed using a variety of methods (e.g., K-nearest neighbor) but can become very computationally expensive, even when N is fairly small. For example, if the probability density function for each of the N features was resolved into 100 bins, then $p(\mathbf{F} | C_{\text{yes}})$ and $p(\mathbf{F} | C_{\text{no}})$ would each require 100^N bins. For a set of only 6 features, sampling each of the two probability density functions would then require 8 *terabytes* of computer memory if stored using double-precision values. This has been referred to as “the curse of dimensionality” (Bellman 1957).

An assumption that considerably reduces the dimensionality of the problem is that the features are independent within each class, so that $P(\mathbf{F}|C_{\text{yes}}) = \prod_{i=1}^N P(F_i|C_{\text{yes}})$ where F_i represents a single feature of the set \mathbf{F} . In this case, equation (3.1) can be written as

$$P(C_{\text{yes}} | \mathbf{F}) = \frac{P(C_{\text{yes}}) \prod_{i=1}^N P(F_i | C_{\text{yes}})}{P(\mathbf{F})}. \quad (3.2)$$

Noting that $P(C_{\text{yes}} | \mathbf{F}) + P(C_{\text{no}} | \mathbf{F}) = 1$, the denominator of (3.2) can be written as

$$P(\mathbf{F}) = P(C_{\text{yes}}) \prod_{i=1}^N P(F_i | C_{\text{yes}}) + P(C_{\text{no}}) \prod_{i=1}^N P(F_i | C_{\text{no}}). \quad (3.3)$$

The combinations of equations 3.2 and 3.3 can lead to a further simplified equation

$$P(C_{\text{yes}} | \mathbf{F}) = \frac{1}{1 + \frac{P(C_{\text{no}} | \mathbf{F})}{P(C_{\text{yes}} | \mathbf{F})}}. \quad (3.4)$$

Equations (3.2) and (3.3) reduce the model described by equation (3.1) from an N -dimensional feature space to two sets of N one-dimensional probability density functions $p(F_i | C_{\text{yes}})$ and $p(F_i | C_{\text{no}})$. Now, if the probability density functions were resolved into 100 bins, then $p(F_i | C_{\text{yes}})$ and $p(F_i | C_{\text{no}})$ would each require $100N$ bins, versus 100^N bins. Revisiting the 6-feature example above, the memory requirement for storing and sampling the probability density functions is reduced from 8 terabytes to 4.8 kilobytes!

The features applied to the probabilistic model are chosen from the SHIPS dataset based on the following criteria: The feature must be significantly different, at greater than the 95% confidence level, between the SEF cases and the cases where no secondary eyewall formed. This was determined using a two-sided Student's t -test. There were a number of features in the SHIPS dataset that satisfied this criterion, and these were then reduced to a final feature set. The final choice of features was based on the performance of the naïve Bayes model using a “leave-one-season-out” cross validation technique. Since model performance metrics will typically exhibit

significant inter-annual variability, this type of cross-validation provides a more robust indication of the expected long-term future performance of the model than validating only one or two years. For each of the 14 years (1997–2010), we removed all data from a single year, formed the prior probabilities [$P(C_{\text{yes}})$ and $P(C_{\text{no}})$] and the class-conditional probability density functions for each of the features [$p(F_i | C_{\text{yes}})$ and $p(F_i | C_{\text{no}})$] with the data from the remaining years, and then estimated posterior probabilities of SEF, using equations (3.2) and (3.3), for the year that was removed. This was repeated for each year, and the probabilities for each year were subjoined to ultimately include all 14 years.

The class-conditional probability density functions, $p(F_i | C_{\text{yes}})$ and $p(F_i | C_{\text{no}})$, were constructed from the data for each feature using kernel-based estimation with a normal kernel function and a window parameter that results in a feature-sampling size of 100 bins. The prior probabilities $P(C_{\text{yes}})$ and $P(C_{\text{no}})$ were also subjoined in the cross validation procedure to be used later when the model is tested against climatology. The values remain constant through each year but change between years because they are based on the event counts of the remaining years in the leave-one-out process. In the N. Atlantic the prior probabilities range from 12% to 15% (the lowest occurs when the 2004 season is removed), and their mean is 14%.

The class-conditional feature sets do exhibit serial correlation, which has the potential to inflate t -test scores. The serial correlation results from having sequential 6-hourly SHIPS features within the 12 h window we use to define an “imminent event”, and from multiple sequential periods during non-events. Formal correction for serial correlation is often problematic in statistical hurricane studies because individual hurricane time series are autoregressive but also independent of the other hurricane time series in the larger sample. Here,

we note this caveat, and consider our cross-validation of the algorithm to present an accurate representation of expected model performance. It is also somewhat reassuring that the separation of each feature applied to the North Atlantic is significant at 99.9% confidence. Following the cross validation criteria outlined in Elsner and Schmertmann (1994), the t -tests for significant separation of the features by class were then repeated with each year omitted from the data. This was done to be sure that the choice of features was independent of data in the omitted year. We found no instances where significance fell below the 99.9% confidence threshold, and the set of features was accordingly held fixed in the cross validation.

***b.* Environmental Features**

The feature set applied in the North Atlantic comprises 9 storm/environmental features and 2 satellite-based features from the SHIPS dataset (described in Table 3.1). The most recent complete list of SHIPS features can be found in the Appendix. An additional satellite-derived feature was also included. It was derived from the principal component analysis of storm-centered azimuthally averaged infrared brightness temperature profiles derived from the HURSAT dataset available at the NOAA National Climatic Data Center⁴ (Knapp and Kossin 2007; Kossin et al. 2007a,b). The eigenmodes of the analysis describe varying radial structures of the average storm-centered brightness temperature, and the expansion coefficients associated with the eigenmodes were considered as potential features. We found that the expansion coefficient associated with the radial structure described by the fourth leading eigenmode was

⁴ The 4th principal component from the HURSAT dataset is used for the period 1997-2006. Due to data constraints, the mean value of all the principal components during this period (.06) is used for all fixes in 2007. A similar dataset to HURSAT was used to calculate the principal components for 2008-2010. The future operational model will use a consistent data source to calculate the principal components that will be identical to the training dataset. It is unknown how the inconsistency of this feature impacts the overall skill of the model, but it is believed to be small.

most useful in separating between our two classes. This eigenmode explains only 2% of the symmetric brightness temperature variation but was found to significantly improve model performance, possibly by capturing anomalous subsidence warming of the upper-level cirrus shield in a region beyond 100 km from hurricane center. This may be related to increased inertial stability caused by local acceleration of the tangential wind often associated with a secondary eyewall (Rozoff et al. 2008), but this relationship between brightness temperature and storm dynamics is uncertain.

We find that SEF is associated with higher maximum potential intensity⁵ (VMPI), lower vertical wind shear (SHRD), weaker upper-level zonal winds (U200), a deep layer of underlying warm water (PHCN), and higher middle- to upper-level relative humidity (RHHI). The relationship with higher relative humidity agrees well with the numerical findings of Nong and Emanuel (2003), and with the basic idea that organized convection in the tropics is sensitive to humidity and dry air entrainment above the boundary layer (e.g. Ooyama 1969). The higher MPI suggests that SEF is favored in an environment that is more thermodynamically supportive of persistent deep convection. In typical tangential wind fields in hurricanes, the radial gradient of angular velocity will inherently tend to organize asymmetric convection into a circular ring. The sensitivity of SEF to shear may be an indication that the shear disrupts this symmetrization process, although the relationship between convection and shear is significantly more complicated (e.g., Kwon and Frank 2008). The class-separation of the 200 mb zonal wind suggests that SEF prefers quiescent upper-levels. The upper-level wind is correlated with the shear ($r = 0.7$), but it is included because it contains additional independent information

⁵ In the SHIPS developmental dataset, maximum potential intensity is calculated as described in Bister and Emanuel (1998).

specifically about the upper-levels and was found to lower the false alarm rate of the model. The physical mechanisms underlying the statistical relationships uncovered here are of great interest, and are presently being explored in theoretical and numerical modeling frameworks, but our purpose here is to exploit these relationships to construct an algorithm that may be usefully applied operationally.

The assumption that the features can be treated independently within each class constitutes the “naïve” aspect of the naïve Bayes classifier defined by equations (3.2) and (3.3) combined with a decision rule. Despite this markedly simplifying assumption, the naïve Bayes classifier has been shown to perform as well and in some cases better than more sophisticated models in a variety of applications, even when the independence assumption is strongly violated (Domingos and Pazzani 1997; Hand and Yu 2001; Zhang 2006). In our feature set the worst violators of this assumption are U200 & SHRD, U200 & LAT, and VMPI & LAT, which have correlation coefficients of 0.51, 0.46, and 0.44 respectively.

***i.* Feature Sensitivity**

The kernel densities profiles of each feature in the model are wide ranging in shape (Fig. 3.1). Some features resemble a nearly Gaussian distribution (e.g., 4th principal component) while others contain more complex distributions (e.g., latitude). The kernel density estimator allows for the model to take advantage of these complex shapes since it preserves the actual distribution of the data. Sometimes a small bump in the distribution creates a separation between classes that has a large impact on the posterior probabilities.

The sensitivity and contribution of each feature to the posterior probabilities was determined by running a controlled version of the Bayes algorithm. In this controlled run, the mean value for each feature was fixed, except for one, which was stepped through from ± 2 standard deviations in 100 intervals. The profile of the posterior probabilities for each feature allows us to determine how important a particular feature is and if there is a range of values within a feature that produces a maximum posterior probability (Fig. 3.2). The greatest probability in the controlled experiment, 99%, occurred when the intensity of the storm was 167 kt and the other features were fixed at their means. The high probability at a time when it is known the other features, i.e. environment, is not perfect, emphasizes the importance of intensity in generating high probabilities of SEF.

In the controlled experiment, stepping through a large range of data allows for values to exceed the maximum or minimum values of the smoothed kernel density estimator. When this occurs, the first/last value of the kernel density is used to obtain a probability. This is why all of the posterior probabilities in the control experiment begin and finish as constants. For example, the posterior probabilities for the controlled shear (SHRD) experiment are fixed at 22% for low, even impossible negative values of shear (Fig. 3.3). This constant is a result of hypothetical data falling outside of the minimum value of the smoothed kernel density profile for both classifications.

Continuing with the shear example, the rapid increase in posterior probabilities for high shear values (> 60 kt) results when values exceed the kernel estimates for the SEF cases but not for the non-SEF cases. Eventually, $P(C_{\text{yes}} | \mathbf{F})$ remains fixed and $P(C_{\text{no}} | \mathbf{F})$ gets smaller, the net effect is that the denominator of equation 3.4 gets smaller, so the probability increases.

Eventually both probabilities become constant and the posterior probability is held at 36%. This example showcases how the model's behavior may not necessarily agree with understood physical relationships. However, observing a feature value beyond the endpoints of a smoothed kernel estimator is very unlikely. Typically, the behavior of the model follows expected physical relationships, i.e. probabilities decrease with increasing shear, within the bounds of what has been observed previously, indicated by the red circles (Fig. 3.2). There are instances however, where certain features contain a "sweet spot" for high probabilities. For example, while high probabilities are associated with high values of humidity (RHHI), probabilities begin to decrease for very high humidity values, even for those that have been observed previously (Fig. 3.2). Whether there is a physical explanation for why very high humidity values would hinder SEF, or whether this is just model behavior operating from a limited dataset, is unknown.

Table 3.1 SHIPS features applied to the Bayes probabilistic model in the North Atlantic.

SHIPS feature	Description	Preference for SEF
VMX	Current intensity	Stronger
LAT	Latitude	Further south
PHCN	Estimated ocean heat content	Deeper
U200	200 mb zonal wind (200-800km from center)	Weaker (near zero), very narrow range
RHHI	500-300 mb relative humidity	Moister
TWAC	0-600km average symmetric tangential wind at 850 mb from NCEP analysis	Stronger
PENC	Azimuthally averaged surface pressure at outer edge of vortex	Lower
SHRD	850-200 mb shear magnitude	Weaker, narrow range
VMPI	Maximum potential intensity	Higher, very narrow range
IR00-02	Average GOES infrared brightness temperature between 0-200 km	Colder, narrow range
IR00-04	Average GOES infrared brightness temperature between 100-300 km	Colder

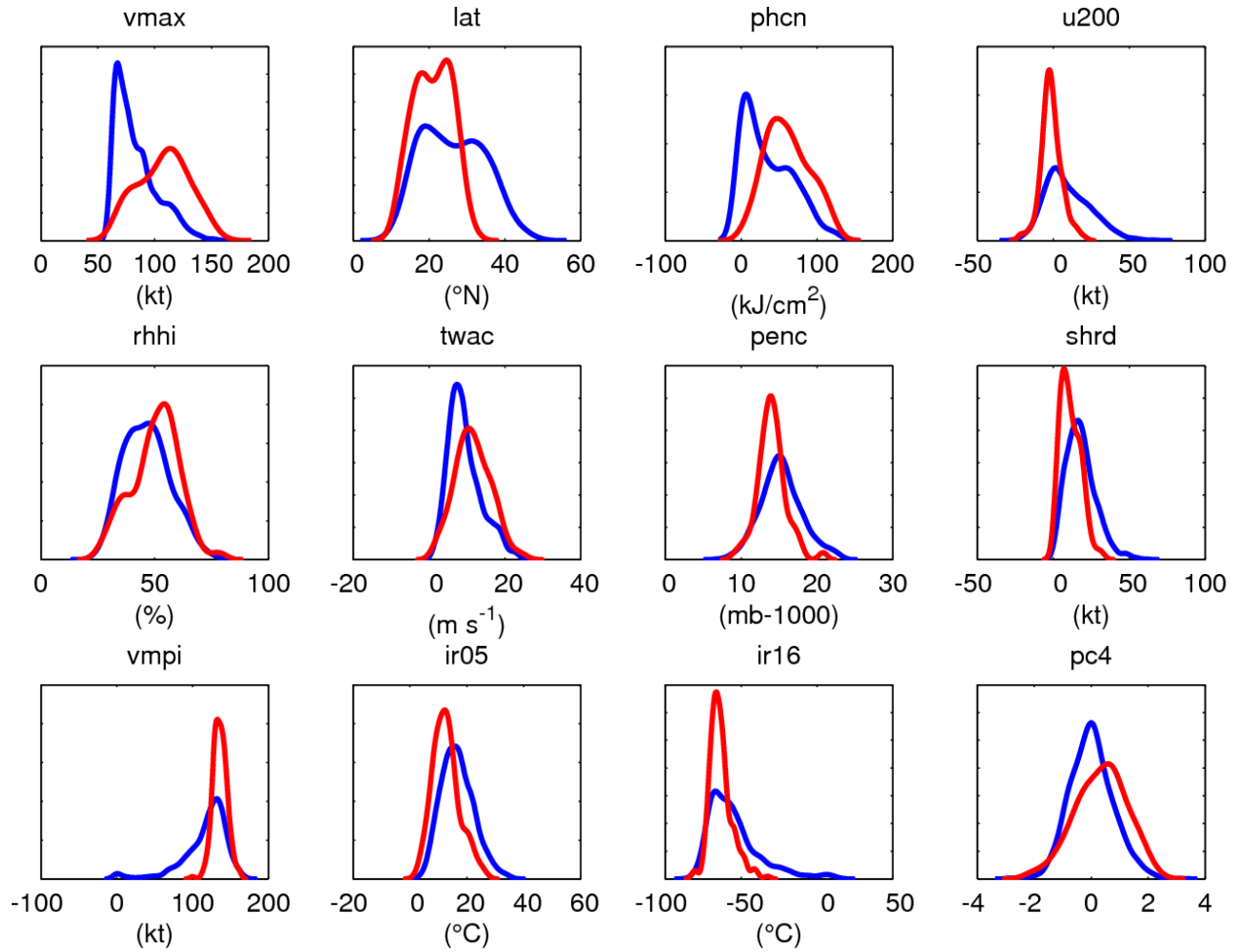


Figure 3.1 Smoothed kernel density estimations for the 12 features used in SEF model. The SEF yes (no) cases appear as a red (blue) line.

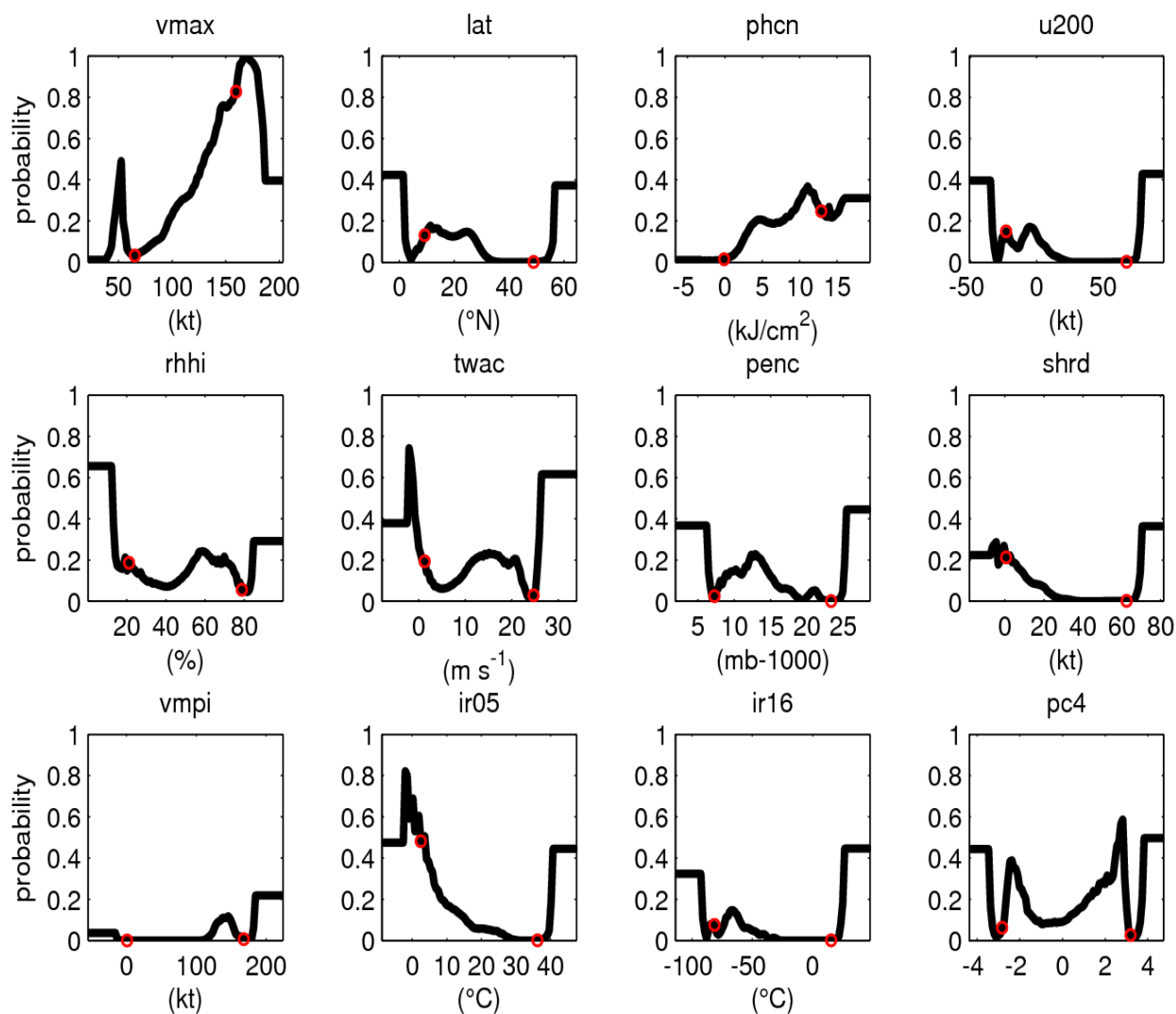


Figure 3.2 Posterior probabilities from the controlled experiment when each feature ranges from ± 2 their standard deviations, while the remaining features remain fixed at their mean. The red rings represent the observed maximum and minimum values for each feature from the SHIPS database.

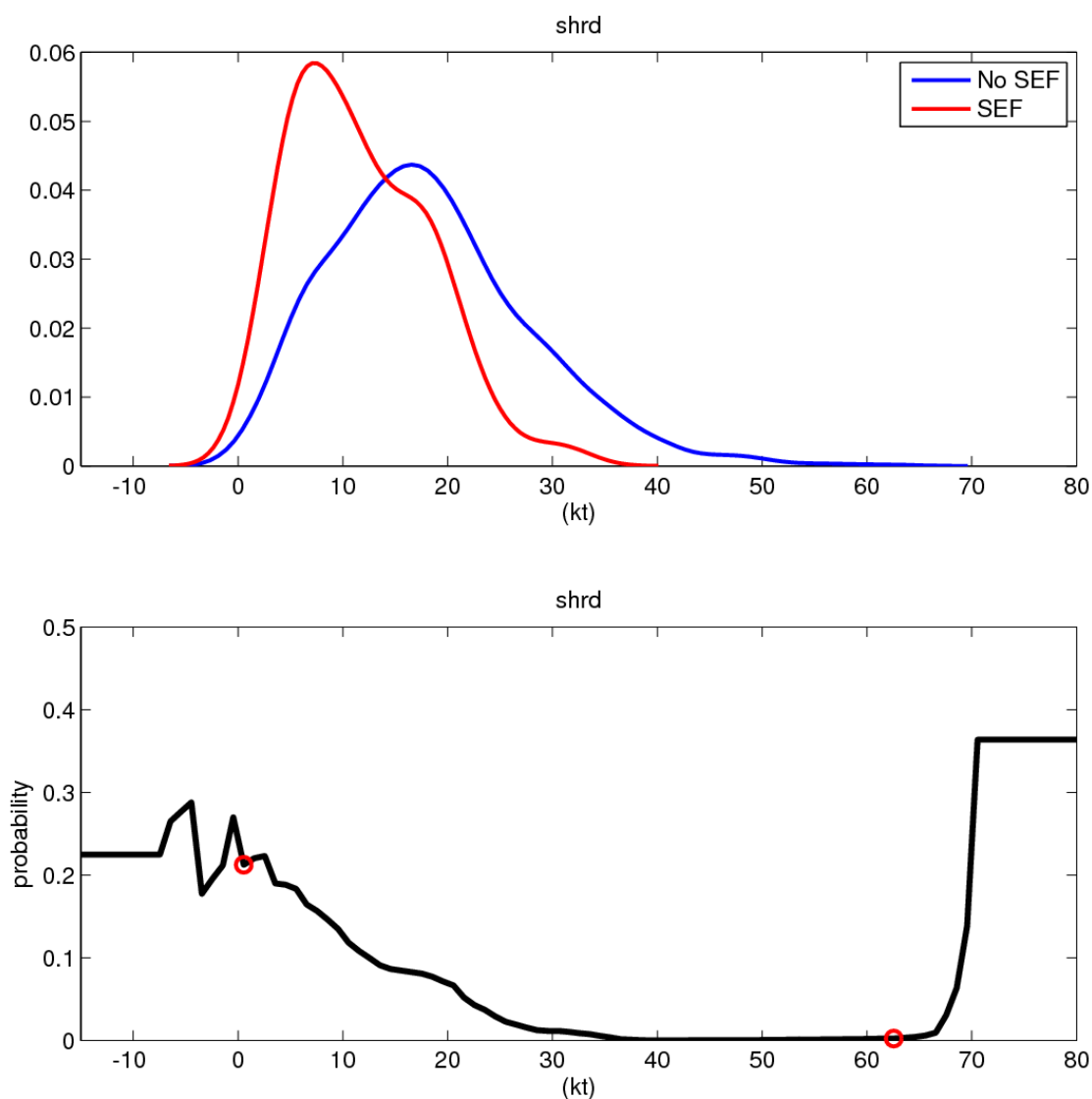


Figure 3.3 *Top*, Smoothed kernel density estimation for the SHRD feature, as in Fig. 3.1. *Bottom*, Posterior probabilities from the controlled experiment, as in Fig. 3.2.

Chapter 4 Model Performance

Some fluctuations in strength could occur in 1 to 2 days due to eyewall replacements. In fact...the UW-CIMSS objective technique shows considerably higher than climatological probability of secondary eyewall formation within 24 to 48 hours.

- *Richard Pasch & Todd Kimberlain, Hurricane Specialists
National Hurricane Center Hurricane Irene Discussion
5 a.m. EDT Wed. Aug. 24, 2011
Matt Sitkowski and Chris Rozoff were aboard a NOAA-P3 aircraft heading toward Hurricane Irene at the time of this advisory.*

In this chapter, the skill of the diagnostic model cross-validated probabilities is measured against climatology. The skill of the model is tested using current intensity as the only feature, using current intensity and the SHIPS environmental features, and using current intensity, SHIPS environmental features, and satellite-derived features (full model). The effect of storm intensity versus storm environment on SEF and the impact of adding the satellite-derived features to the model are assessed when all three versions of the model are tested for skill. A discussion on the skill and development of an operational SEF model is introduced and the reliability of both models is also discussed.

a. Diagnostic Model

A total of 1507 cross-validated posterior probabilities were computed from the Bayesian probabilistic model over the 14 year period. The values ranged from 0 to .99, with the majority of the probabilities, 74%, less than .05 and only 1% greater than 0.9. A variety of metrics, which are outlined here, were applied to assess the cross validated performance of the model.

A number of metrics used to assess skill required that a “decision rule” be applied to the Bayes model output so it can be easily reduced to a *classifier*. One simple decision rule is to

assign the class with the greatest posterior probability given by the model. In a binary “yes or no” classification problem, a probability greater than 50% would be chosen. A slightly more complex procedure is to enforce some optimal decision threshold based on analysis of a Receiver Operating Characteristic (ROC) diagram (see, e.g., Wilks 2006), but it is not always clear how to define an optimal threshold and will generally depend on the priorities of the model users. This will be discussed further in this chapter.

To assess the binary (yes/no) classification algorithm we considered three metrics based on 2×2 contingency tables: the Peirce skill score, the “probability of detection” (or “hit rate”), and the “false alarm rate”. The area under the ROC curve was also used as an additional measure of the model’s overall ability to distinguish SEF events from non-events. All of the tools introduced here are described further in Wilks (2006).

One additional skill score (Briggs and Ruppert 2005) based on 2×2 contingency tables was also applied to assess model performance against climatology. The optimal yes/no predictions based naïvely on climatology would always indicate that no SEF is expected to occur. This would, for example, result in 87% correct predictions, and the model should improve on this in order to be considered skillful if the error (or loss) is considered to be symmetric. Here, symmetric loss indicates equal penalty for a false negative (miss) and false positive (false alarm). Note that this is markedly different from the Peirce skill score, which weakly penalizes false alarms and provides a measure of confidence to forecasters who must predict the occurrence of rare events. The Briggs and Ruppert skill score under the assumption of symmetric loss is given by

$$K = \frac{n_{11} - n_{01}}{n_{11} + n_{10}},$$

where n_{11} , n_{01} , and n_{10} are the number of correct positive classifications (hits), false positive classifications (false alarms), and false negative classifications (misses), respectively. This skill score can be extended to account for asymmetric loss (e.g., situations where overprediction may be more or less costly than underprediction) and, as mentioned briefly above, for misclassification error (Briggs et al. 2005).

The Brier skill score does not require a decision rule and uses the posterior probability to determine the skill of the model compared to climatology. The Brier skill score is defined as $1 - B / B_{\text{ref}}$, where

$$B = \frac{1}{k} \sum_{i=1}^k [P(C_{\text{yes}} | \mathbf{F})_i - O(i)]^2$$

$$B_{\text{ref}} = \frac{1}{k} \sum_{i=1}^k [P(C_{\text{yes}}) - O(i)]^2$$

and $O(i) = 1$ or 0 for cases of SEF or no formation, respectively. Here, k is the number of cases the algorithm is applied to, and $P(C_{\text{yes}} | \mathbf{F})_i$ is the posterior probability estimate deduced from equation (3.2) for a specific individual time.

An important point to emphasize is that we use current intensity (VMX in Table 3.1) as a feature in the Bayes probabilistic model, which represents a strong violation of the assumption of feature independence required for the “naïve approximation” of the model. For example, it is well known that current intensity is closely related to ambient vertical wind shear. As noted in chapter 3, the model has been shown to typically perform very well regardless of this violation,

but the inclusion of current intensity makes it more difficult to explicitly separate the effect of storm intensity versus storm environment on SEF. To mitigate this, we will compare model performance for three cases: 1) using current intensity as the only feature, 2) using current intensity and the SHIPS environmental features, and 3) using current intensity, SHIPS environmental features, and satellite-derived features.

Utilizing the subjoined sets of posterior probabilities formed with the cross validation method described in the previous chapter, the performance of the probabilistic model and classifier is shown in Tables 4.1 and 4.2. In this case, the classifier is based on the maximum posterior probability decision rule, that is, we choose whichever class, C_{yes} or C_{no} , is assigned a probability greater than 50%. Since the prior probabilities (i.e., the climatological expectation based on counts) are always much smaller than 50%, there would never be a prediction of imminent SEF based on climatology. This is reflected in the 2×2 contingency table at the top of Table 4.1 and in the metrics in the top row of Table 4.2. When the current intensity is used as the sole feature in the model, there is a measurable increase in the probability of detection and in the skill as measured using the Brier and Peirce skill scores. The area under the ROC curve, which provides an overall measure of the model's ability to distinguish between classes, is 0.74. This value can range from 0.5 to 1.0 where 0.5 is the expectation based on climatology. In general, 0.5–0.6 is considered a failure of the model, 0.6–0.7 is poor, 0.7–0.8 is fair, 0.8–0.9 is good, and 0.9–1.0 is excellent, so here the model does a “fair job” of distinguishing between classes when current intensity is the sole input feature.

To determine the reliability of the model output an attributes diagram was constructed (Fig. 4.1). The 45° diagonal line represents perfect reliability across the range of possible

probabilities. Points that lie within the shaded region contribute to increasing model skill and points outside the region decrease skill (see Wilks 2006 for more detail). When current intensity is the sole feature, the model does a reasonable job of correctly assigning lower probabilities, as seen by the proximity of some of the points to the perfect reliability diagonal, but the model completely fails to correctly assign higher probabilities. When the SHIPS environmental features are included, the model improves markedly. This is seen clearly in the attributes diagram, which shows improvement across most of the probabilities with particularly good improvement in correctly assigning high probabilities of SEF. The Brier and Peirce skill scores, probability of detection, and the area under the ROC curve all increase, while the false alarm rate doubles, but remains relatively small (Tables 4.1 and 4.2). When the GOES satellite-based features are added to the model, little change occurs to the attributes diagram, but the number of hits increases from 57 to 59, increasing the probability of detection from 29% to 31%, while the number of false alarms decreases, from 55 to 37. Inclusion of the three GOES features increases the Brier and Peirce skill scores from 17% to 20% and 25% to 28% respectively, and the area under the ROC curve still suggests that the model is “good” at distinguishing between classes.

Figure 4.2 shows the cumulative distributions of the probabilities of SEF assigned by the model when separated by the observed class. When current intensity (VMX) alone is used (Fig. 4.2a), roughly 50% of the observed “no-formation cases” were assigned a probability of formation of less than 10%, while around 80% of the observed formation cases were assigned a probability of more than 10%. Only about 12% of the formation cases were assigned a probability greater than 50% using VMX as the sole feature. When the SHIPS environmental features are added to the model (Fig. 4.2b), there is a large increase in the number of cases that

are assigned a near-zero probability of SEF. Almost 70% of the assigned probabilities were near zero for the cases of no observed formation, and about 30% of the observed formation cases were assigned a probability greater than 50%. When the GOES-based features are added (Fig. 4.2c), about 30% of the observed formation cases were assigned a probability greater than 50%, while about 25% were assigned a probability of formation near zero.

To provide a sense of the model characteristics when applied to individual hurricanes, Figure 4.3 shows the evolution of the model-assigned probabilities of SEF in four North Atlantic hurricanes. The SEF probability based solely on the intensity (VMX) of each hurricane is also plotted. The relationship between hurricane intensity and the probability of SEF is apparent (e.g., Hurricane Katrina (2005), Fig. 4.3a), but it is also clear that large-scale environmental conditions are significantly controlling the probabilities assigned by the model. For example, the model-assigned posterior probability remains near zero for Hurricane Ike (2008) during a period of rapid intensification that was followed by a prolonged period (0000 UTC 04 Sept. – 0000 UTC 6 Sept.) of high intensities (Fig 4.3b). Conditions may have been favorable for intensification, but they were not ideal for SEF. Instances where a large departure exists between posterior probabilities from the full model and the VMX-only model are most useful to forecasters. When high (low) probabilities are assigned for a weak (intense) storm a forecaster knows the environment is conducive (constraining) to form a secondary eyewall.

***i.* Optimal Decision Threshold**

The contingency tables and the metrics derived from those tables – the probability of detection, false alarm rate, and Peirce skill score – shown in Tables 4.1 and 4.2 are based on a decision threshold of 50% probability. As discussed in chapter 2, this may not be an “optimal” threshold, but the choice of what should define optimal is generally situation-dependent. For example, in some situations keeping the false alarm rate low may be a priority, while in others, maximizing the probability of detection may be of greater importance. The Bayes probabilistic model provides posterior probabilities, which can then be subjected to any decision rule to form a classification assignment. In an operational hurricane-forecasting environment, the model would most likely be used in the same manner that other models – empirical or numerical – are used. That is, the forecaster can assess the evolution of the probability of SEF in real time, and form an expert judgment based on a variety of available information and a working knowledge of the traits and behaviors of the models being considered. In this case, there is no need to reduce the information provided by the model by reducing it to a binary classifier. Nonetheless, it is instructive to consider the performance of the classifier based on various decision rules, if for no other reason than to scrutinize the model characteristics as deeply as possible.

Here two additional decision thresholds are considered, given by the prior (climatological) probabilities and by an analysis of the ROC curve. For the latter, we chose the threshold defined by the point on the curve closest to the point (0, 1), which represents a perfect model in the ROC diagram and maximizes the Peirce skill score. Because of the large number of probabilities that are near zero, as discussed above, this threshold value is in fact very small (~ 2%). Table 4.3 shows the 2×2 contingency tables, based on the model using all features (VMX plus ENV plus IR), for the two different thresholds, and Table 4.4 shows the performance

metrics based on the contingency tables. When the threshold is lowered, there is a marked increase in the probability of detection as well as skill, as measured by the Peirce skill score, but there is a commensurately large increase in the false alarm rate. When the optimal threshold based on the ROC curve analysis is used, the number of false alarms increases by a factor of more than 7 compared to Table 4.2, while the number of hits increases by a factor of almost 2.5. The Peirce skill score increases to 53% while the Briggs and Ruppert skill score shows considerably less skill than climatology. This reemphasizes the challenge of objectively defining an optimal classifier; maximizing a particular skill score may not provide the best tool if low false alarm rates are as important as high probabilities of detection.

***b.* Operational Model**

The diagnostic model was developed with the knowledge of the best-track intensity and an accurately analyzed ambient environment. Thus far, the skill of the model has been evaluating its ability to successfully *diagnose* SEF. In an operational setting, however, knowledge of when SEF will take place is more beneficial than simply stating the process is presently underway. By letting the feature set \mathbf{F} represent the SHIPS *forecast* values the model easily becomes a prognosticating tool, however, the skill of the operational model depends on the accuracy of the SHIPS intensity forecast and analysis of the large-scale environmental features. Any inaccuracies of the SHIPS forecast can add to the inherent error of the diagnostic model.

As part of the United States Weather Research Program Joint Hurricane Testbed (JHT) the model was transitioned to operations at the NHC for testing during the 2010 and 2011 hurricane seasons. The SHIPS intensity forecast and large-scale environmental analysis at times

$t=0$, $t=12$, $t=24$, and $t=36$ were used to determine the probability of SEF over the next 0-12 h, 12-24 h, 24-36 h, and 36-48 h. The model was run each time SHIPS guidance was executed by NHC forecasters. The probabilities were then appended to the SHIPS output text file (Fig. 4.4). A cumulative probability of these 4 forecast intervals was also made available to forecasters.

The Brier skill score (Table 4.5) was used to assess the skill of the operational model during the 2-year testing period. In addition, the operational SHIPS files were obtained for the 2008 and 2009 seasons and operational probabilities for those years were computed in-house. Although limited to only 4 years, the operational version of the SEF model was skillful for all forecast periods. As expected, the skill decreases further out in time, but the Brier skill scores remain positive, indicating that skill is added to the model compared to climatology. The model performed reasonably well for all but the 2009 season, where there was no skill in forecasting SEF. The 00-12 h and 12-24 h forecast periods during the 2010 season and the 00-12 h and 36-48 h forecast periods during the 2011 seasons matched or outperformed the skill of the diagnostic version of the model.

The reliability of the operational model for each of the 4 forecast periods is presented in an attributes diagram (Fig. 4.5). Most of the skill is obtained by correctly assigning an extremely low probability when SEF is not likely to occur. All of the forecast periods struggle to correctly assign high SEF probabilities (>0.6), except for the 00-12 h forecast period. But, even this forecast period has room for improvements given the distance of the results from the perfect reliability line.

Although a skillful model that alerts forecasters to the likelihood of SEF and a subsequent ERC is beneficial, the model does not provide guidance on how forecasters should adjust their forecasts. An essential factor and first-step in determining how to modify intensity, wind radii, and storm surge forecasts, for example, is knowledge of climatological intensity and structure changes associated with ERCs. Willoughby et al. (1982) documented the intensity evolution for a few case studies, and the present paradigm describes a weakening associated with SEF, often followed by a reintensification as the secondary eyewall contracts. These intensity deviations are generally observed to be transient and occur on intra-daily time-scales. Consequently, the archival records of hurricane intensity comprising the 6-hourly best track fixes are not particularly well suited for the task since the best track is a temporally smoothed record by design. This was corroborated with our SEF database, where it was found that the statistics of best track intensity change associated with SEF were not distinguishable from the larger sample of hurricanes. This result remained robust when we only considered best track fixes that were contemporaneous with aircraft reconnaissance measurements. To address this shortfall, the next chapter discusses the development of a large archive of raw high temporal resolution aircraft reconnaissance data that is exploited to form a more exhaustive and modern climatology of intensity evolution associated with ERCs.

Table 4.1 Four 2×2 contingency tables for classification of SEF events in the North Atlantic. The top 2×2 table is based on the climatological probability of SEF. The next table is based on the probability estimated from the new algorithm using current intensity as the sole feature. The next table shows how the inclusion of the SHIPS environmental features improves the algorithm performance. The bottom table is based on the addition of the GOES satellite-derived features. All values are based on cross validation of the model.

	Forecast	Observed	
		YES	NO
Climatology	YES	0 (hits)	0 (false alarms)
	NO	196 (misses)	1263 (correct negatives)
Current intensity only	YES	23	24
	NO	173	1239
Current intensity plus SHIPS environmental	YES	57	55
	NO	139	1191
Current intensity plus SHIPS environmental plus GOES	YES	59	37
	NO	130	1159

Table 4.2 Performance metrics of the model applied to the North Atlantic.

	Brier skill score	Peirce skill Score	Briggs & Ruppert skill score	Probability of detection	False alarm rate	Area under ROC curve
Climatology	0%	0%	0%	0%	0%	0.50
Current intensity only	9%	10%	1%	12%	2%	0.74
Current intensity & SHIPS environmental	17%	25%	1%	29%	4%	0.84
Current intensity & SHIPS environmental & GOES	20%	28%	12%	31%	3%	0.84

Table 4.3 2×2 contingency tables for two different decision rules applied to the North Atlantic.

	Forecast	Observed	
		YES	NO
Decision rule: posterior probability greater than prior probability	YES	100	122
	NO	89	1074
Decision rule: posterior probability greater than “optimal” threshold	YES	145	282
	NO	44	914

Table 4.4 Performance metrics of the model under two decision rules.

	Peirce skill score	Briggs & Ruppert skill score	Probability of detection	False alarm rate
Decision rule: posterior probability greater than prior probability	43%	-12%	53%	10%
Decision rule: posterior probability greater than “optimal” threshold	53%	-72%	77%	24%

Table 4.5 Operational brier skill scores.

Year	00-12 h	12-24 h	24-36 h	36-48 h
2008	.14	.12	-.06	.02
2009	-.06	-.02	-.01	.05
2010	.27	.23	.11	.10
2011	.21	.18	.14	.20
2008-2011	.18	.16	.06	.10

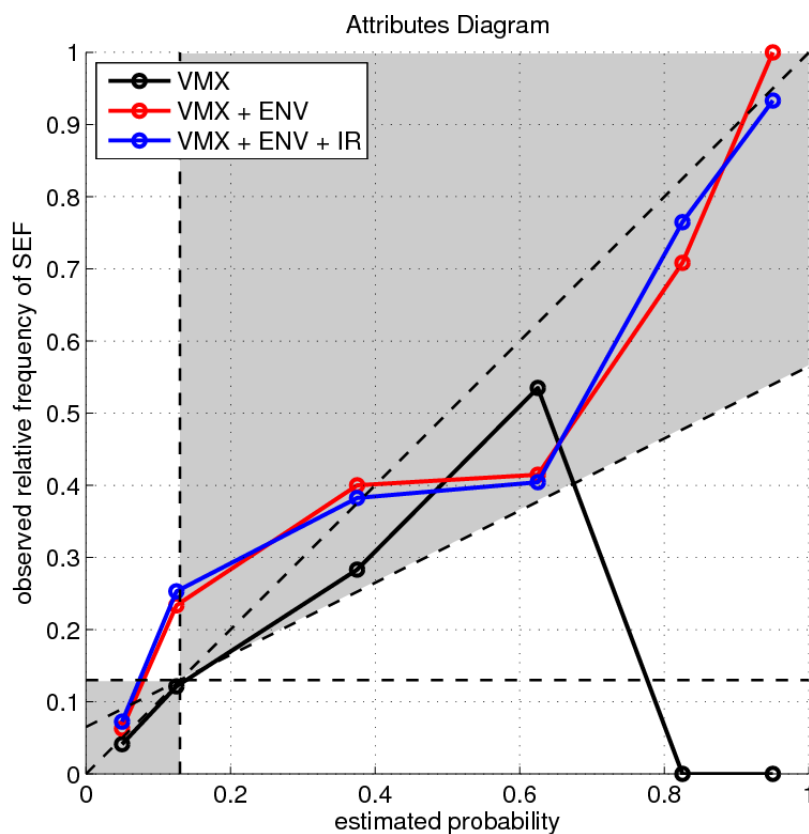


Figure 4.1 Attributes diagram for the Bayes probabilistic model for 3 different choices of features: current intensity only (VMX), current intensity plus SHIPS environmental features (VMX plus ENV), and current intensity plus SHIPS environmental features plus infrared-based features (VMX plus ENV plus IR). The posterior probabilities given by the model were placed in 6 bins of varying ranges with each point plotted at the bin center. The bin ranges were chosen *ad hoc* to reduce sampling fluctuations. The counts within each bin, from least to greatest probability, are {633, 454, 325, 43, 1, 3} for VMX only, {1089, 137, 95, 82, 24, 6} for VMX plus ENV, and {1134, 87, 68, 47, 34, 15} for VMX plus ENV plus IR.

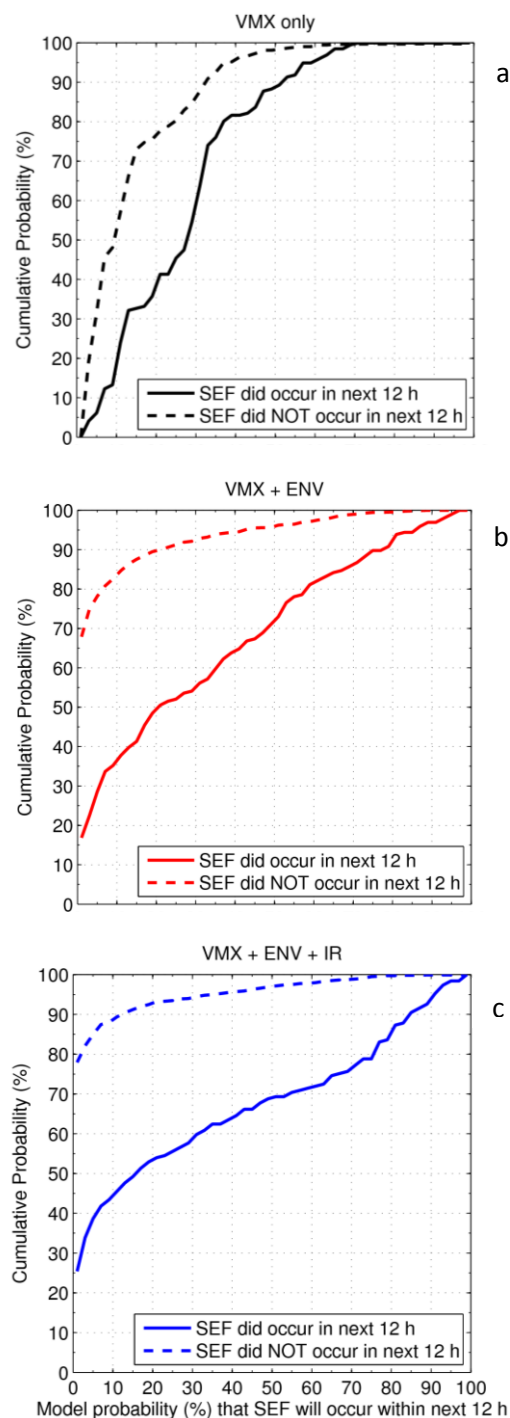


Figure 4.2 Cumulative probability of the model-estimated probability of imminent SEF using (a) VMX as the sole feature, (b) VMX plus the SHIPS environmental features, and (c) with the final addition of the infrared satellite-based features. Solid curves: probability of SEF assigned to cases that were observed to form secondary eyewalls. Dashed curves: probability of SEF assigned to storms that were *not* observed to form secondary eyewalls.

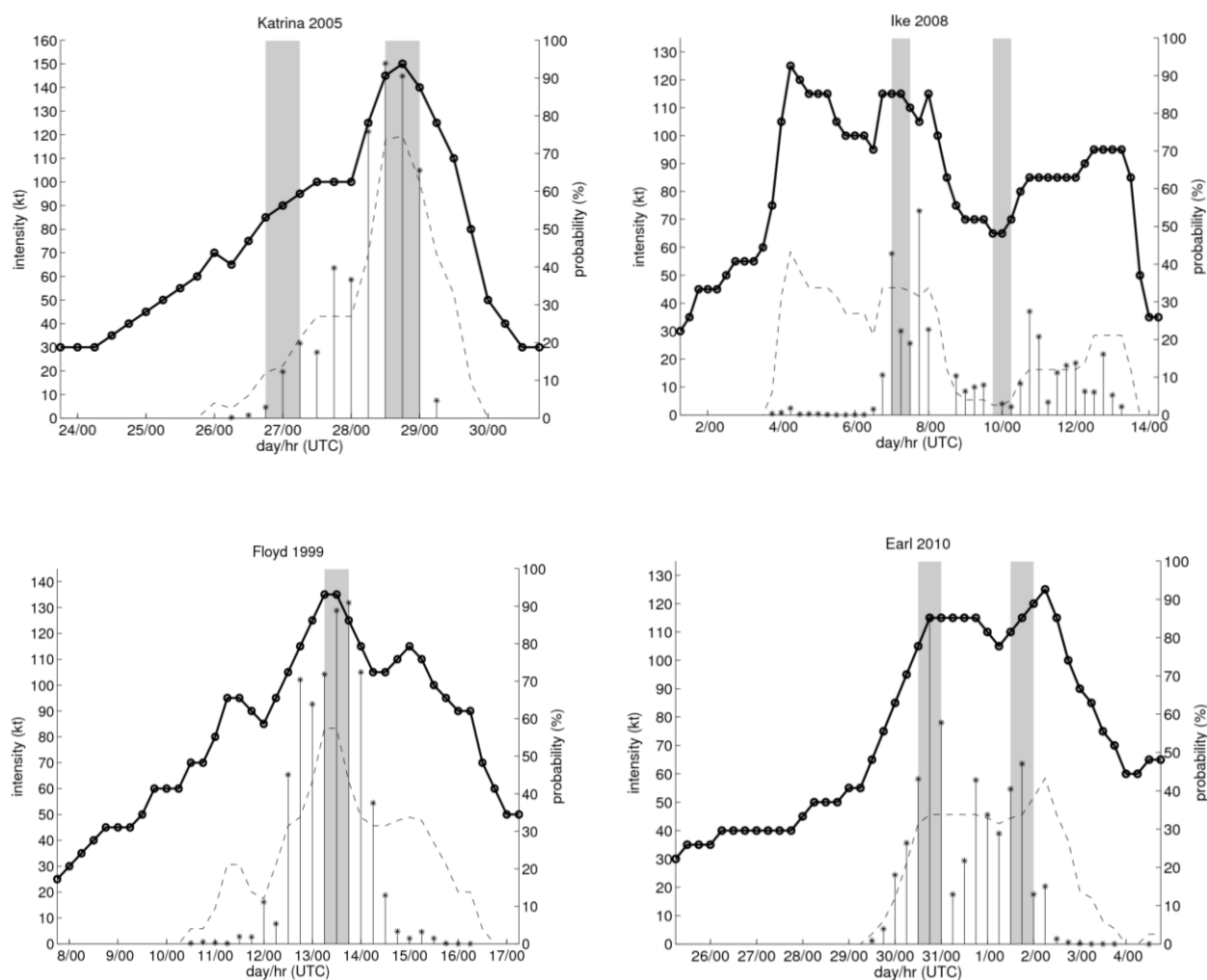


Figure 4.3 Evolution of current intensity (solid black line, left axis), VMX-model estimated probability of SEF (dashed line, right axis), and VMX plus ENV plus IR model-estimated probability of SEF (stem plot, right axis) in Hurricanes Katrina (2005), Ike (2008), Floyd (1999), and Earl (2005). Probabilities are not assigned when the intensity is less than 65 kt or when the storm center is over land. Each gray shaded region denotes a period that a SEF event was observed within.

** PROBLTY OF AT LEAST 1 SCNDRY EYEWL FORMTN EVENT AL092011					IRENE 08/24/2011 12 UTC **	
TIME (HR)	0-12	12-24 (0-24)	24-36 (0-36)	36-48 (0-48)		
CLIMO (%)	22	27 (43)	28 (59)	29 (71)	<-- PROB BASED ON INTENSITY ONLY	
PROB (%)	29	64 (74)	85 (96)	82 (99)	<-- FULL MODEL PROB (RAN NORMALLY)	

Figure 4.4 SEF model output as it appears at the end of the SHIPS output text file. SHIPS Guidance was run at 1200 UTC 24 August, when Matt Sitkowski and Chris Rozoff were aboard a NOAA-P3 aircraft in the eye of Hurricane Irene (2011). The probability for SEF over the next 12 h was 29%, which is 7% greater than the intensity-based climatology. Higher probabilities were forecast out to 48 h, with a cumulative probability of 99%. Two SEF events did verify. One was at the time guidance was run, 1200 UTC 24 August, and the other was 54 h later at 1800 UTC 26 August.

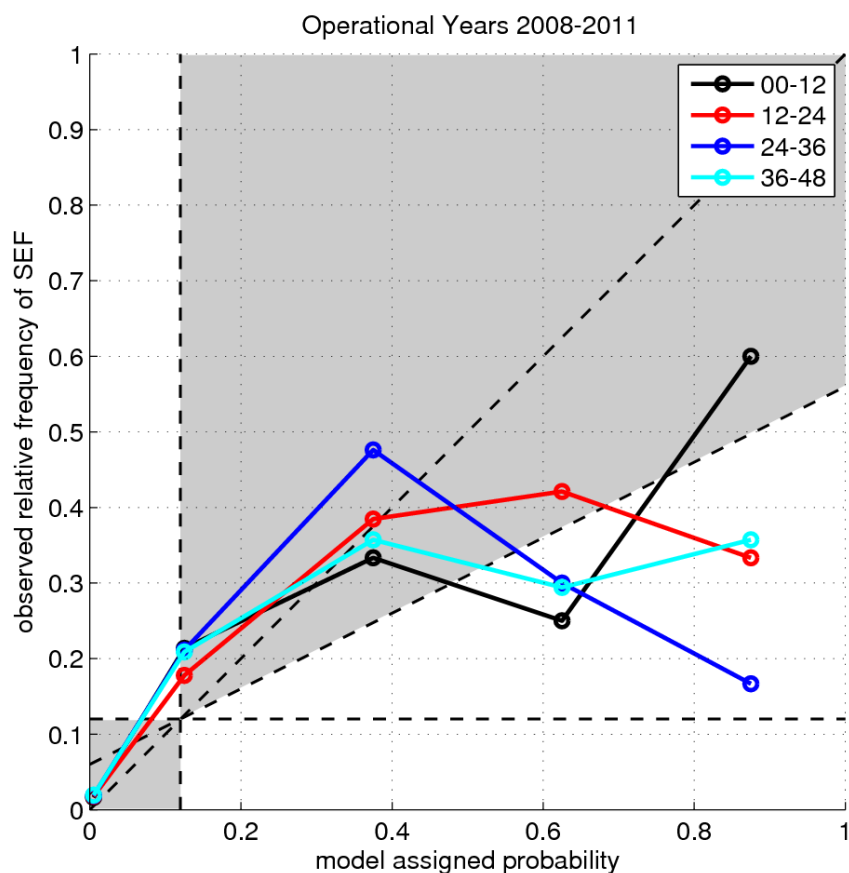


Figure 4.5 As in Fig. 4.1, but for 4 forecast periods of the 2008-2011 operational model. The counts within each bin, from least to greatest probability, are roughly {1235, 95, 20, 20, 12}.

Chapter 5 Eyewall Replacement Cycle Database

I was unable to fly close to the disturbance, visible to me for miles. It appeared to be a cone-shaped body of clouds, inverted, rising to an altitude of 12,000 feet. The waves in the sea below broke against each other like striking a sea wall.

- *Leonard Povey, an American in the Cuban army, describes his flight from Havana to investigate the Labor Day Hurricane of 1935 just before it made landfall in the Florida Keys.*

Presently, forecasters at the National Hurricane Center use intensity forecast guidance techniques that largely fail to capture intensity fluctuations associated with ERCs (Elsberry et al. 2007). Additionally, there is no obvious expectation that diagnostic satellite-based intensity estimation would recognize intensity departures due to eyewall replacement. Previous ERC studies are primarily limited to case studies for a few individual storms. As ERC research progresses, especially with successful modeling experiments, detailed documentation of in-situ measured intensity and structure changes associated with ERCs is highly desirable. This chapter discusses the methodology and data used to develop the documentation.

The best-track dataset is a smoothed, discrete (every 6 h) estimate of hurricane location and maximum intensity (resolved within 5 kt intervals) during the entire lifetime of a tropical cyclone. Often, the official intensity of a storm is a fusion of various intensity estimates. Forecasters have the option to weight these various estimates based on the reliability of the measuring platform. For this reason and the inherently smoothed nature of this dataset, intensity changes associated with ERCs are often washed out or underrepresented. To largely mitigate this issue, this study utilizes flight-level aircraft reconnaissance data to better capture inner-core

intensity and structure changes. While there are differences between best-track intensities and aircraft data, the use of a single, consistent raw data source allows for a better depiction of intensity and inner-core wind structure changes associated with ERCs.

***a.* Flight-level Dataset**

Flight-level aircraft data provide critical in-situ measurements of the inner-core intensity and wind structure over the data sparse ocean. In this study, the NOAA Hurricane Research Division (HRD) archive of Atlantic flight-level aircraft observations processed from 1977-2001 is utilized. The dataset consists of kinematic and thermodynamic measurements at various isobaric levels collected from both NOAA WP-3D and USAF WC-130 aircraft. The aircraft typically fly radial legs through the storm center out to at least 150 km and they alternate their angle of approach toward storm center to sample all four quadrants of the storm. For each radial leg, storm-centered, storm-relative data are smoothed and interpolated to a radial grid with 0.5-km grid spacing from storm center out to 150 km. Instrument wetting is a known source of error in the flight-level thermodynamic data (Eastin et al. 2002) and these errors are reduced following a correction outlined by Zipser et al. (1981). Remaining temperature and equivalent potential temperature (θ_e) errors, which are usually greatest in the updraft regions of the eyewall, are around 0.5 °C and 2.5 K respectively (Eastin et al. 2002).

The HRD database is only available from 1971-2001, so 2002-2007 flight-level data are processed in a nearly identical manner as the HRD dataset. The updated portion of the dataset utilizes the HRD “.trak” files which contain an estimated center fix every 2 minutes and is based on the center-finding methodology of Willoughby and Chelmow (1982). Additionally, linear interpolation is used to fill gaps of missing flight-level data that cover a distance of less than 10

km. Further details of the flight-level data, especially regarding thermodynamic measurements, can be found in Samsury and Zipser (1995), Mallen et al. (2005), Kossin and Eastin (2001), and Eastin et al. (2002).

Storms that never achieved hurricane intensity are excluded in this study and limitations were encountered during data-gathering that prevented the use of every storm flown by aircraft from being included in the dataset. Nonetheless, our full dataset consists of over 6000 radial legs in 79 hurricanes between 1977 to 2007. While many hurricanes were sampled by reconnaissance aircraft while undergoing an ERC, inclusion in the dataset used to develop the ERC climatology requires that hurricanes remain over water during the entire ERC and that temporal sampling must be concentrated so virtually the entire ERC is captured by reconnaissance aircraft. This resulted in 24 ERCs, consisting of nearly 1700 radial legs of aircraft data, from 14 of the 79 hurricanes. Due to the discontinuous nature of aircraft sampling, there is implicit uncertainty in measures such as start and end times of these 24 ERC events, and it is understood that this may introduce error into our analyses. Additionally, error can be introduced by data gaps during an individual ERC, but this is likely to be small as aircraft observations occurred, on average, nearly every hour and timespans between sorties averaged less than 4 hours. Some well-known hurricanes that contained ERCs (e.g. Allen 1980 and Gilbert 1988) unfortunately did not meet the rigorous temporal sampling requirements of the study. Table 5.1 lists the observed start and end times of the 24 ERCs used to develop the climatology.

Since flight-level data are taken at various pressure surfaces, all tangential winds are adjusted to a common reference level of 700 mb following Franklin et al. (2003), which documents mean vertical wind profiles of the eyewall and outer vortex region for numerous hurricanes using GPS dropwindsondes. Here, the eyewall and outer vortex vertical wind profiles

from Franklin et al. (2003) are averaged and a single pressure-dependent correction is applied to the entire length of the radial leg. Winds observed at lower (higher) pressure surfaces than 700 mb will have their winds increased (reduced) when adjusted to 700 mb. Roughly 67% of the flight-level observations from the 14 hurricanes used to develop the ERC climatology were obtained near 700 mb. The majority of the remaining observations were taken at higher pressure (lower altitude) levels. This necessary adjustment is motivated solely to add consistency to wind magnitudes for subsequent composite analyses, and should not be interpreted to imply that the radial wind structure is maintained vertically.

***b.* Rankine Fits**

Hurricane tangential wind profiles along radial flight legs are often noisy and determination of the maximum intensity, radius of maximum wind (RMW), and outer wind maximum can be difficult to ascertain. For these reasons, tangential wind profiles are often smoothed or approximated by continuous analytic functions with adjustable parameters that represent physically meaningful aspects of the profile. The Holland (1980) model, dual-exponential profiles (Willoughby et al. 2006), and the modified Rankine vortex (Mallen et al. 2005) all capture the essence of the tangential wind profile under the assumption that there is a single primary wind maximum located at the RMW. More recently, complex equations have been developed to account for tangential wind profiles with dual wind maxima (Holland et al. 2010; Wood et al. 2010).

This study utilizes a simpler and more objective method in order to capture the most relevant features of the radial profiles and facilitate analyses and comparison while keeping the number of adjustable parameters tractable. Each pressure-adjusted tangential wind profile is fit

with a modified Rankine vortex and double modified Rankine vortex (defined below). Hereafter, “modified Rankine vortex” will be referred to as “single modified Rankine vortex” to explicitly distinguish between the two fits. Examples of these fits can be seen in Fig. 5.1. The single modified Rankine vortex is described by the equation:

$$V_r = \begin{cases} v_1 \left(\frac{r}{r_1}\right), & (r \leq r_1) \\ v_1 \left(\frac{r_1}{r}\right)^{\alpha_1}, & (r_1 < r \leq 150 \text{ km}) \end{cases} \quad (5.1)$$

The function is zero at the vortex center and linearly increases to a maximum tangential wind value of v_1 at radius r_1 . The function then decreases gradually away from the storm center according to the decay parameter α_1 . When α_1 equals 0 the outer wind field is constant and equal to the maximum intensity v_1 . As α_1 increases, the outer wind field quickly decays and the maximum intensity becomes more peaked in structure. The combination of r_1 , v_1 , and α_1 that results in the smallest root mean squared error between the parameterized fit and the observations is obtained for each flight leg. Here, r_1 and α_1 are of the resolution 1 km and 0.025, respectively.

As a potentially useful aside, fitting observed wind profiles in this manner offers an effective objective method for identifying the Radius of Maximum Slope Change defined by Corbosiero et al. (2005). This radius can be argued to be more physically relevant than the RMW in cases where the tangential wind beyond the eyewall is relatively constant and the RMW becomes highly sensitive to small wind changes in that region.

The same procedure is followed for the double modified Rankine vortex, but five new parameters are introduced (Fig. 5.2a). The inclusion of r_{moat} , v_{moat} , r_2 , v_2 , and α_2 allows for the

identification of an outer wind maximum. The α_1 portion of the fit in the double modified Rankine vortex ceases at a pivot location between the two wind maxima. This position is labeled (r_{moat}, v_{moat}) , but there is no thermodynamic reasoning for the naming convention. Rather, the moat is simply referring to a position between the inner and outer wind maxima. The position (r_{moat}, v_{moat}) is analogous to the vortex center in the single modified Rankine vortex. From this position the fit is allowed to continue away from the storm center to identify an outer wind maximum. Again, the smallest root mean squared error between the parameterized fit and the observations is obtained for each flight leg. The double modified Rankine vortex is represented by the equation:

$$V_r = \begin{cases} v_1 \left(\frac{r}{r_1}\right), & (r \leq r_1) \\ v_1 \left(\frac{r_1}{r}\right)^{\alpha_1}, & (r_1 < r \leq r_{moat}) \\ v_1 \left(\frac{r_1}{r_{moat}}\right)^{\alpha_1} + \left(\frac{v_2 - v_1 \left(\frac{r_1}{r_{moat}}\right)^{\alpha_1}}{r_2 - r_{moat}}\right)(r - r_{moat}), & (r_{moat} < r \leq r_2) \\ v_2 \left(\frac{r_2}{r}\right)^{\alpha_2}, & (r_2 < r \leq 150 \text{ km}) \end{cases} \quad (5.2)$$

To offset the vastly increased computational expense of determining 8 parameters for the double Rankine fit, the parameters r_1 , r_{moat} , and r_2 are of the resolution 3 km and α_1 and α_2 are resolved in increments of 0.08. This coarser resolution still provides adequate profile fits to the data.

Once both fits are applied to each radial leg, a subjective determination is made as to which profile more accurately parameterizes the radial wind structure. Therefore, every radial leg used in the study contains an (r_1, v_1) pair. If there is only a single wind maximum, this pair is determined from the single modified Rankine vortex. If an outer wind maximum is present, then the (r_1, v_1) pair is determined from the double modified Rankine vortex, along with an (r_2, v_2) pair.

An example of both single and double modified Rankine vortex fits for a complete pass (2 radial legs) through the center of Hurricane Gilbert (1988) is presented in Fig. 5.2b. Because Gilbert contains double eyewalls, the double modified Rankine fit provides a superior fit to the data in this example. Similar good agreement is found between the single modified Rankine vortex fits and the flight-level data in storms containing only a single wind maximum.

In the event that an outer wind maximum is clearly evident in the radial wind profile, but the fitting procedure fails to correctly identify the correct wind maxima, a manual correction is applied. Corrected parameters account for roughly 15% of all the single and double modified Rankine parameters. Associated with each set of (r_1, v_1) and (r_2, v_2) pairs is a timestamp from when the aircraft is very near the storm center. This information can be used to examine the evolution of both the inner and outer (when one is observed) wind maxima during the entire time a hurricane is being investigated by reconnaissance aircraft.

Triple wind maxima (e.g., McNoldy 2004) were occasionally present in the radial wind profiles. Figure 5.2 provides an example from Hurricane Frances (2004), a hurricane with multiple ERCs. In this example, the innermost wind maximum is associated with a decaying inner eyewall and the middle wind maximum is intensifying as an ERC nears its completion. The outermost wind maxima are from spiral rainbands that eventually organize into an outer eyewall where an additional ERC ensues. Calculating a triple modified Rankine vortex, which contains 13 parameters, for every profile is computationally unfeasible, so for the few profiles that displayed three wind maxima, the Rankine parameters were subjectively determined and manually entered into the dataset.

c. Microwave Imagery Dataset

The analysis of aircraft data is supplemented by 85-GHz radiances from low earth-orbiting satellites with passive microwave sensors. These data have been obtained from the NOAA/NCDC HURSAT-MW dataset (SSM/I; Knapp 2008) and NASA (AMSR-E and TMI) (Ashcroft and Wentz 2006). An overlying cirrus canopy associated with tropical cyclone outflow typically obscures inner-core structure in infrared and visible satellite imagery, but this cloud layer is largely transparent in the 85-GHz channel. Scattering of large precipitation particles provides a snapshot of the inner-core precipitation structure in the 85-GHz channel (Hawkins and Helveston 2004). Figure 1.1 is an example of microwave imagery of an inner and outer convective eyewall. Although microwave observations of any tropical cyclone can be occasionally limited to time increments exceeding 12 h due to the finite global coverage of the satellites, these data have proven essential in identifying outer eyewalls over the open ocean. Hawkins and Helveston (2008), Kossin and Sitkowski (2009) and Kuo et al. (2009) developed criteria for SEF based on subjective determination of how complete and thick an outer convective ring appears on microwave imagery. In these studies, however, there was no discussion of whether or not a wind maximum was associated with convection, and no study to date has assembled a large enough sample of ERCs to determine the average time required to complete an ERC and its associated variance.

Table 5.1 Start and end times for all 24 ERC events as defined in flight-level aircraft data.

ERC Event	Start Time (UTC)	End Time (UTC)	ERC Event	Start Time (UTC)	End Time (UTC)
1984 Diana	09/11/13:23	09/12/19:16	2004 Frances	09/01/05:40	09/03/17:29
1995 Luis	09/04/22:16	09/05/20:54	2004 Frances	09/03/16:36	09/04/19:01
1995 Luis	09/06/14:00	09/08/11:26	2004 Ivan	09/08/17:48	09/09/23:29
1997 Erika	09/08/20:14	09/09/19:16	2004 Ivan	09/09/16:42	09/11/09:17
1998 Georges	09/19/18:48	09/21/09:09	2004 Ivan	09/10/19:13	09/12/20:39
1999 Floyd	09/11/08:49	09/12/05:37	2004 Ivan	09/12/11:30	09/14/17:21
1999 Floyd	09/12/17:31	09/14/20:28	2005 Katrina	08/26/15:58	08/28/00:10
2002 Isidore	09/19/17:54	09/20/23:10	2005 Katrina	08/28/11:03	08/29/12:09
2003 Fabian	09/03/17:28	09/05/11:22	2005 Rita	09/21/17:53	09/23/05:07
2003 Isabel	09/15/19:36	09/18/16:54	2005 Wilma	10/18/19:53	10/20/10:20
2004 Frances	08/30/05:47	08/30/21:16	2007 Dean	08/18/05:00	08/19/05:11
2004 Frances	08/30/18:12	09/01/11:05	2007 Dean	08/19/01:05	08/20/05:16

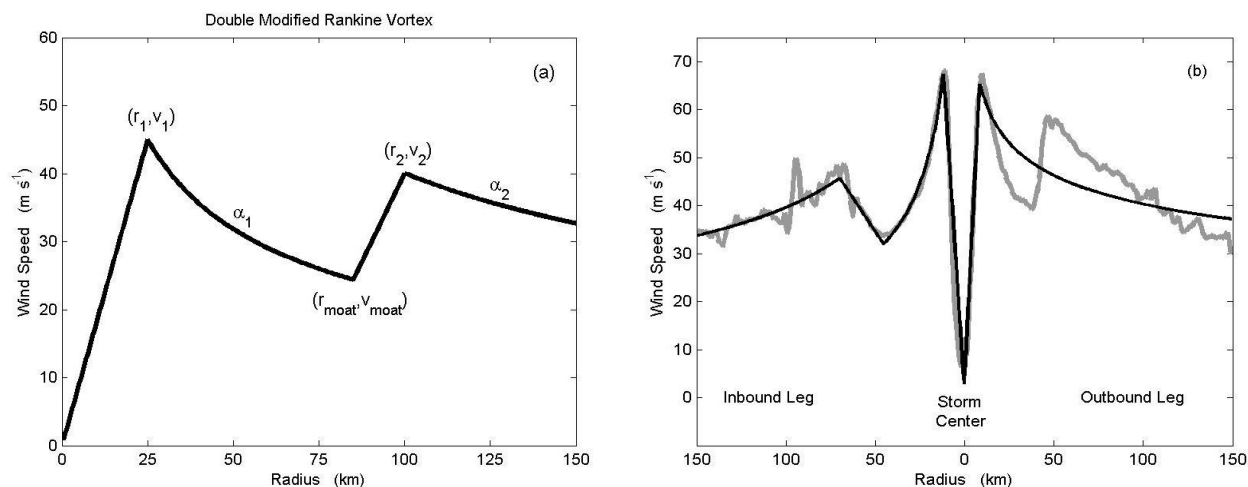


Figure 5.1 a) A double modified Rankine vortex with all eight parameters labeled. The radius is from storm center. b) A complete profile (inbound and outbound radial legs) of tangential wind (gray line) for Hurricane Gilbert (1988). The inbound pass is fit with a double modified Rankine vortex, capturing both wind maxima. The outbound pass is fit with a single modified Rankine vortex which only allows for the detection of a single wind maximum.

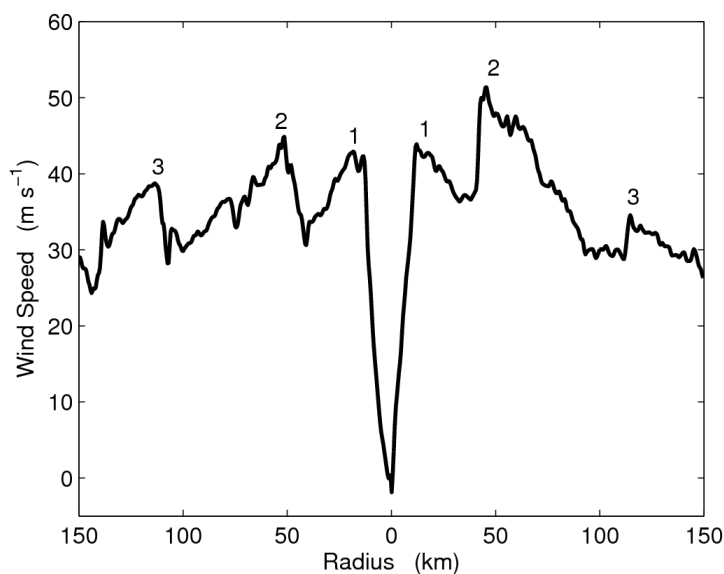


Figure 5.2 A complete profile (inbound and outbound radial legs) of tangential wind for Hurricane Frances (2004). Three wind maxima, identified by number, are observed for each leg. The aircraft was near the storm center at 1815 UTC 30 August. The radius is from storm center.

Chapter 6 Kinematic Climatology

Science isn't just cold, hard facts. The crux is fitting unfitted things together and making them hang together. It's similar to composing music or art or poetry.

– *Dr. Joanne Simpson, first woman to earn a Ph.D. in Meteorology (1923-2010)*

The development of a large newly-constructed flight-level in-situ aircraft dataset and the fortune to have adequate reconnaissance coverage for 24 ERCs, permits the documentation of typical intensity and structures changes, and their variance, associated with North Atlantic basin ERCs. This chapter describes these changes and discusses how the convective appearance in microwave imagery, the most frequent method of observing ERCs, evolves in conjunction with flight-level observations. The role of ERCs in broadening the inner-core wind field is also examined.

a. Hurricane Diana 1984

Hurricane Diana (1984) is presented first to introduce the reader to the process involved in developing the climatology. The evolution of the inner (r_1, v_1) and outer (r_2, v_2) wind maxima are displayed for Hurricane Diana (1984) in Fig. 6.1. The first aircraft sorties into the hurricane on 9 and 10 September sampled a weak tropical cyclone with flight-level winds of 20 - 25 m s⁻¹. The initial estimates of the inner radius contain considerable spread. This may be due to the short-lived, stochastic nature of convection during the developmental stages of a tropical storm, which can cause the primary wind maximum to be transient resulting in variability in r_1 (Simpson et al. 1997). When the aircraft began sampling on 11 September, the tropical cyclone

was stronger and intensifying. A more robust inner-core with sustained convection (see Willoughby 1990 Fig. 18) was established and the r_1 variance is reduced; however, some spread remains. Some small variance is expected due to the accuracy of the least squares Rankine fits correctly identifying the location of the primary wind maximum. More importantly, variance exists because hurricanes are not perfectly axisymmetric. For example, an elliptical eyewall will result in a larger r_1 parameter if the aircraft flies along the major axis instead of the minor axis. Piech and Hart (2008) found that aircraft observations routinely report elliptical eye structures prior to the formation of concentric eyewalls.

As seen in Fig. 6.1, the aircraft encountered an outer wind maximum in Diana (1984) shortly before 1200 UTC 9 September. Outer wind maxima are not always collocated with a developing convective outer eyewall feature (Samsury and Zipser 1995) and the lack of additional outer wind maximum observations suggests this local maximum was likely from isolated cellular convection or a rainband. Near 1200 UTC 11 September, the aircraft again encountered outer wind maxima at roughly the same distance (75 km) from storm center. Unlike the outer wind maximum from two days prior, this outer wind maximum was the first of many measurements that formed a coherent evolution of a contracting outer wind maximum.

Just before Diana's landfall on 13 September (Fig. 6.1), an outer wind maximum roughly 140 km from storm center was observed. Although only a single data point, it is possible that it signals the initiation of another ERC. The timing and location of the observation are in agreement with many ERCs examined in the study that underwent multiple ERCs, which are discussed later in this chapter. Some storms even formed an outer wind maximum while a previous ERC was concluding; these storms exhibited triple wind maxima.

Criteria for determining when an ERC initiates and concludes have never been formally established. This decision is subjective and is heavily influenced by the medium being used to investigate the inner-core of a hurricane. An added level of complexity is that regardless of which observing platform is being operated, the formation of an outer eyewall and decay of inner eyewall are not instantaneous events, rather they can occur over several hours. This study defines the length of an ERC based solely on flight-level aircraft data. The start of ERC begins when the first of a coherent cluster of outer wind maximum, in space and time, is detected. The cycle concludes when the outer wind maximum transitions to the primary eyewall and the remnant inner wind maximum can no longer be detected.

Based on this criterion, the complete ERC of Diana (1984) is shown in Fig. 6.2. The r_1 , v_1 , r_2 , v_2 parameters are fit with a third-order polynomial best fit line to make use of all the data and capture the essence of the structure and intensity evolutions. The initial r_2 measurements contain considerable spread since outer wind maxima are prone to be associated with rainbands that are located at various distances from storm center. At the start of the ERC the best fit suggests the outer wind maximum is near 70 km with an intensity around 25 m s^{-1} . The inner wind intensity is roughly 48 m s^{-1} and is located about 18 km from storm center. The inner wind maximum is intensifying at the start of the ERC during an *intensification phase*, but eventually reaches a maximum intensity near 1800 UTC 11 September before beginning to weaken for the remainder of the ERC. As the primary intensity weakens during the *weakening phase*, the outer wind maximum contracts and intensifies, eventually surpassing the intensity of the inner wind maximum around 1500 UTC 12 September. After 0600 UTC 12 September, the r_2 estimates are tightly clustered and a well-defined outer eyewall and moat between eyewalls is visible from

aircraft radar (see Willoughby 1990 Fig. 18c). The outer wind maximum continues to intensify during the *reintensification phase* until the aircraft departs the hurricane. When an aircraft returns, less than 6 hours later, the first pass detects a single wind maximum with an r_1 value of 28 km. The hurricane returns to a single wind maximum structure.

Even in the case of Diana (1984), where confidence is very high that virtually the entire ERC is captured by aircraft, it is not known exactly when concentric eyewalls, rather than organizing spiral rainbands, first appear by simply analyzing the Rankine parameters. The first few r_2 observations are more scattered than those towards the end of the ERC. This behavior is found in several of the ERCs investigated in the study. At what point are the outer wind maxima being encountered by aircraft associated with concentric rings, rather than spiral rainbands? Due to the extensive usage of microwave imagery in diagnosing ERCs and its familiarity among forecasters, the intensity and structure changes for many of the ERCs are compared with the evolution of microwave imagery.

b. Microwave Imagery

Extensive examination and comparison of microwave imagery and flight-level data for 20 out of the 24 ERCs is carried out to clarify the inner-core precipitation structure during the evolution of an outer wind maximum. The hurricanes not included in this portion of the study occurred before the advent of microwave imagery or lack sufficient imagery. Diagnosing when a double eyewall structure first appears in microwave imagery is challenging given the irregularity of the temporal sampling, and there is inherent uncertainty in our estimates of these times.

The analysis reveals that for all 20 ERCs, aircraft detect outer wind maxima several hours before a pronounced double eyewall configuration appears in microwave imagery. Microwave imagery usually shows rainbands spiraling from the eyewall when an outer wind maximum is first detected by aircraft. These data reveal that the outer wind maximum associated with the spiral rainbands contracts and intensifies during the transition to an outer eyewall. It appears the outer wind maximum associated with concentric eyewalls has been contracting before the concentric eyewall first appeared in microwave imagery. The physical relevance of this observed behavior is an interesting and open question.

On average, the concentric eyewall configuration is estimated to appear in microwave imagery nearly 18 hours after the first detection of an outer wind maximum as defined in the aircraft flight-level data. In addition, 17 out of the 20, or 85% of ERCs with adequate microwave imagery contained a more intense inner eyewall than outer wind maximum when concentric eyewalls first appear in microwave imagery, but the inner eyewall is typically half way through its weakening phase at this time. The inner eyewall typically weakens for almost 8 hours prior to the double eyewall structure first appearing in microwave imagery and continues weakening for several more hours before it is overtaken by the contracting outer wind maximum.

Figure 6.3 illustrates an example from Hurricane Floyd (1999) of spiral rainbands containing local wind maxima transitioning to a concentric eyewall structure. The spiral rainbands in Floyd are visible in the microwave imagery and contain local wind maxima that range over various radii, depending on the approach of the aircraft. The rainbands do not completely wrap around the center initially (Fig. 6.3 bottom-left), but eventually develop and organize into a concentric ring with a well-defined moat between the inner and outer eyewalls

(Fig. 6.3 bottom-middle). In this example, the primary eyewall intensifies prior to the development of the concentric eyewalls in microwave imagery. At some critical point, shortly before the time concentric eyewalls appear in microwave imagery, the storm's intensity begins to decrease. These results suggest the developing outer eyewall begins its detrimental effects on the inner eyewall before a complete outer ring structure is established. The weakening is consistent with previous work that indicates rainbands alone can introduce low-entropy air into the low-level inner eyewall inflow, as well as act as a barrier to the eyewall (e.g., Barnes et al. 1983; Barnes and Powell 1995; Powell 1990a,b; Hausman 2001). As the inner eyewall's latent heating begins to weaken, the ability of the storm to maintain an intense, localized warm core decreases (Rozoff et al. 2008).

Aircraft leave Floyd just as the decaying inner eyewall diminishes and microwave imagery depicts a single, larger eye and eyewall than what was observed at the start of the ERC. This newly established primary eyewall continues to contract and the storm intensifies. The entire ERC takes just over 2 days.

c. Intensity and Structure Changes

The ERC intensity evolutions of Hurricanes Diana (1984) and Floyd (1999) are fairly representative of the 24 ERCs examined in this study. Both ERCs contain an intensification, weakening, and reintensification phase. To quantify the intensity changes during an ERC and the amount of time required for those changes, a third-order polynomial best fit of the Rankine parameters r_1 , r_2 , v_1 , and v_2 is applied to all 24 ERCs. This results in a smooth, continuous evolution of radii, intensity, and time and allows for determination of several key properties of

ERCs. Each ERC is then divided into the previously mentioned phases (e.g., Fig 6.2). The documentation of the 3 phases expands upon the known paradigm first established by Willoughby et al. (1982).

The composite analysis of the polynomial fit data along with the distribution of that data for all the 3 phases of the ERC is displayed in Fig. 6.4. Associated with each ERC phase are vertical boxplots that display the range of intensity changes (m s^{-1}) of v_1 and v_2 and horizontal boxplots that display the range of time (h) required to complete that particular portion of the ERC (Fig. 6.4a). Figure 6.4b follows the same arrangement, but displays the radii changes. Details of each phase are as follows:

- 1) *Intensification* – This phase begins at the start of an ERC and concludes when the inner wind maximum reaches peak intensity. In general, this portion of the ERC is characterized by both inner and outer wind maxima undergoing contraction and intensification even though the outer wind maximum is unlikely to be associated with a well-developed convective ring during this phase. Often, the inner wind maximum is concluding a period of rapid intensification. Ten storms contained an inner wind maximum intensification rate that exceeded $0.5 \text{ m s}^{-1} \text{ h}^{-1}$ during this phase, which is comparable to the 90th percentile of 24-h over water intensification rates for tropical cyclones examined by Kaplan et al. (2010). Seven of the twenty-four ERCs did not contain an intensification phase because the inner eyewall was at peak intensity at the start of the ERC.

- 2) *Weakening* – This phase is bounded by the peak intensity of the inner wind maximum to when the outer wind maximum intensity surpasses the intensity of the inner wind maximum. During this phase, the inner wind maximum steadily weakens as the outer wind maximum continues to contract and intensify. All but 2 ERCs contained an intersection of intensities. Georges (1998) had an outer wind maximum that was weakening in tandem with the inner wind maximum and aircraft departed Isidore (2002) just before the intensities were preparing to intersect. As was the case with the inner wind maxima in the intensification phase, many of the secondary wind maxima in the weakening phase are rapidly intensifying. At this point in the ERC the outer wind maximum, if it has not already, is organizing into a circular ring. Although determination of the exact SEF time is unrealistic, the average estimated time when a double eyewall configuration first appears on microwave imagery occurs during this phase, or almost 18 hours after the start of the ERC. While the secondary wind maximum becomes better defined and arranges into a convective ring it is also contracting. During the weakening phase the average contraction rate of r_2 is 1.75 km h^{-1} .
- 3) *Reintensification* - The reintensification portion of the ERC refers to the period when the outer wind maximum intensity surpasses the inner wind maximum intensity and continues to intensify. As this occurs, the inner wind maximum decays and eventually dwindles away in the eye. Once the inner wind maximum can no longer be detected, the ERC is considered complete and the storm returns back to a single eyewall structure. Although the ERC has concluded and the intensity is no longer tracked once the inner eyewall has decayed, the hurricane often will continue to intensify. In some cases this

occurs rapidly, resulting in the hurricanes maximum lifetime intensity (e.g. Hurricane Katrina 2005).

A schematic diagram summarizing the evolution of an ERC appears in Fig. 6.5. The average values of the Rankine parameters (Fig. 6.4) also appear in Fig 6.5. The intensification phase, weakening phase, and reintensification phase last approximately 9, 16, and 11 hours respectively. At the start of an ERC the location of r_2 is 3 times the distance of r_1 . This distance is reduced to twice the distance of r_1 at the end of the ERC. The value of v_2 is $2/3$ that of v_1 at both the start of an ERC and at the transition time from the intensification phase to the weakening phase. Interestingly, the maximum intensity at the start of an ERC, when an outer wind maximum is first observed, is nearly the same when the last inner wind maximum is detected at the end of an ERC.

While the average values of the Rankine parameters in Figs. 6.4 and 6.5 agrees well with previously documented inner-core changes associated with ERCs, the box plots (Fig. 6.4) highlight the high variance with these events. Table 6.1 lists the mean and standard deviation for the intensity changes, radii changes, and time requirements for each phase of the ERC. The mean and standard deviation for the time required for the entire ERC as well as the amount of time for concentric eyewalls to appear on microwave imagery after the first detection of an outer wind maximum are also listed. In many cases the variance is high and the standard deviation is greater than the mean. While the climatology allows for the appreciation of inner-core changes during an ERC, it cannot be understated that an individual event can have large departures from the climatology.

Figure 6.6 compares the climatological ERC intensity, radii, and time changes with those observed from an Ivan (2004) ERC. The most anomalous phase for this ERC is the intensification phase, where the intensity increase, contraction of the inner wind maximum, and length of time to complete this phase are more than double the climatological values. The weakening phase is more in line with climatology, but the outer wind maximum has an extraordinary intensification rate resulting in a much greater increase in intensity after the inner and outer intensities intersect. Although the final values of r_1 and r_2 were similar to the climatological ERC values, the final flight-level v_2 intensity at the end of the ERC is almost 70 m s^{-1} , or just over 25 m s^{-1} greater than at the start of the ERC. Further analysis has begun to exploit this newly developed dataset and explore methods to detect systematic conditions that can help better quantify inner-core structure and intensity changes to assist forecasters (Kossin and Sitkowski 2012).

The composite analysis for the ERC phases only examines key times of the ERC, so a phase diagram of the ratio of wind maxima v_1/v_2 versus the ratio of their respective locations r_1/r_2 was developed to make use of the entire polynomial fits for each of the 24 ERC events (Fig. 6.7). It is important to note that time and intensity are not captured in Fig. 6.7. Some lines in the phase diagram can occur over a period of 18 h, while others exceed 48 h and hurricanes from all categories are included.

The slight arc shape of the phase diagram in Fig. 6.7 begins with many of the ERCs containing an average inner wind maximum around 1.5 times the intensity of the outer wind maximum located 3 times the distance of the inner eyewall. This is one region in the phase space where data are more tightly clustered. Roughly 25% of all the ERCs passed very near this region.

As the secondary wind maximum contracts inward, the r_1/r_2 ratio increases as r_1 changes little and r_2 is reduced. The v_1/v_2 ratio usually decreases as a result of v_2 increasing, v_1 decreasing, or some combination of the two. When v_1/v_2 equals 1 the intensities of the inner and outer eyewalls are equal. This usually occurs when r_1/r_2 is near .5, or when r_2 has reached twice the distance of r_1 . Roughly 1 in 4 ERCs pass near this region at some point during the ERC. The final v_1/v_2 ratio is less than 1, indicating the outer eyewall has transitioned into a primary eyewall.

Where the lines are not located is also of interest. It is rare to have an outer wind maximum be less than half the intensity of the inner wind maximum at the start of an ERC. Also, it is rare for the outer wind maximum to be first detected at a radius more than 6 times the radius of the inner wind maximum. The concave shape of the diagram suggests that there is not a linear relationship between the behaviors of the two wind maxima.

***i.* Multiple Eyewall Replacement Cycles**

Occasionally, conditions are favorable for hurricanes to undergo multiple ERCs (Hawkins and Helveston 2008). These hurricanes are a great resource to examine the intensity and structure variations associated with ERCs. Figure 6.8 displays all of the radii parameters observed during Hurricane Ivan (2004). There are 7 separate events of an intensifying and contracting outer wind maximum during Ivan's lifetime! Towards the end of each of these events are jumps in eye sizes indicative of the replacement of the inner eyewall by an outer wind maximum. Ivan also exhibits 3 cases where triple wind maxima were observed in the storm. The triple wind maxima eventually transition to secondary wind maxima once the innermost wind maximum decays. Microwave imagery for Ivan and other storms with triple wind maxima

supports the notion of rainbands and co-located wind maxima organizing around a double eyewall structure rather than a well-developed triple ring structure depicted in microwave imagery. However, convective triple ring configurations were observed in Hurricane Juliette (2001) (McNoldy 2004).

Figure 6.9 displays the evolution of wind maxima during the ERCs in Ivan between 1200 UTC 10 September 2004 and 0000 UTC 13 September 2004. A previous ERC is concluding when the outermost wind maxima are first detected near 1800 UTC 10 September (Fig. 6.9). A microwave image taken shortly before aircraft arrive near 1900 UTC 10 September shows a double eyewall configuration with the outer eyewall located between 50 and 100 km from storm center (Fig 6.9 bottom-left). Banded convection elements also appear at and beyond 100 km, but these spiral bands do not contain the same cold brightness temperatures found in the outer eyewall. However, aircraft do encounter local wind maxima associated with the bands (Fig 6.9 blue dots), resulting in triple wind profiles. The green dots show the innermost wind maximum from the previous eyewall decaying in the soon to be larger, developing eye.

There is a clear intensification of the storm in the 18 h between 1800 UTC 10 September and 1200 UTC 11 September. This is a result of the previous ERC concluding as the once secondary wind maximum continues to contract and takeover as the primary eyewall. Ivan reaches 910 mb, its lowest lifetime minimum sea-level pressure, near 0000 UTC 12 September (Franklin et al. 2006). Microwave imagery taken just after the remnant eyewall can no longer be detected show a well-defined single eye with warm brightness temperatures, indicative of warm, subsiding air (Fig 6.9 bottom-center). At this time, the secondary wind maxima near 100 km are associated with more cellular convection that have become more circular, but still lack cold

brightness temperatures, usually indicative of strong convection (Fig 6.9 bottom-center). More intense cellular convection, located beyond 100 km, could contain local wind maxima, but were not yet detected by aircraft. Roughly 18 h after the microwave image Aircraft do encounter local wind maxima beyond 100 km, observing yet another start to an ERC. To avoid congestion, these triple wind maxima are intentionally left off of Fig. 6.9, but they do appear in Fig. 6.8.

Ivan reached peak intensity in flight-level winds around 1800 UTC 11 September, 6 h before a minimum in sea level pressure was attained and weakens until the outer wind maximum surpasses the inner wind maximum. Just after the wind maxima intersect, a microwave image reveals that the rainband features have quickly organized in a circular fashion and have become more convective (Fig 6.9 bottom-right). There was a rapid intensification rate of the secondary wind maximum that was nonlinear and increased as the ERC progressed. The development of the convective structure of the inner-core in less than 24 h between 1348 UTC 11 September and 1252 UTC 12 September is stunning, and the intensity changes are drastic. As a result of this ERC, Ivan again reached its lowest lifetime minimum sea-level pressure of 910 mb near 2100 UTC 13 September (Franklin et al. 2006). The outer wind maximum intensified 25 m s^{-1} from 1800 UTC 11 September to 1800 UTC 12 September. This rapid intensification occurred in association with rapid strengthening since the outer wind field beyond the outer wind maximum remained elevated (Fig. 6.10).

***ii.* Wind Field Expansion**

The Hovmöller diagram (Fig. 6.10) of pressure adjusted flight-level winds for Hurricane Ivan (2004) depicts several ERCs. All of the tangential wind profiles over a period of several

days were utilized to create the diagram and interpolation was used for periods when reconnaissance was absent from the storm. There are several interesting features captured by the Hovmöller diagram. A repetitive process occurs with each ERC. At some distance beyond the RMW a local maximum of wind is observed, usually near a time where wind speeds at the RMW are very intense. Over time, the outer wind maximum contracts inward toward the vortex center and intensifies. In doing so, the outer wind field expands and remains elevated. Eventually, the inner eyewall is replaced by this outer wind maximum. Typically, the outer wind maximum fails to contract beyond the original primary eyewall radius. Instead, shortly after the secondary eyewall has transitioned into the primary eyewall, contraction halts and the storm is left with a larger eye.

Aircraft data and Hovmöller diagrams from other hurricanes depict similar behavior indicating that ERCs are a mechanism for storm growth. Our dataset contains 10 ERCs that occur after an ERC has occurred previously for the same hurricane. The initial r_l parameter at the start of the repeat ERCs was larger than the initial r_l at the start of the previous ERC for 90% of these events. In addition, 80% of the repeat events took longer to complete than the previous ERC. A larger eyewall and more expansive wind field can result in larger rainfall amounts and an increase in storm strength. Additionally, a broader post-ERC wind profile can certainly result in greater storm surges as the results of Irish et al. (2008) suggest.

A composite analysis of tangential wind profiles for each of the 3 ERC phases from all 24 ERC events is shown in Fig. 6.11. Similar to Maclay et al. (2008), integrated kinetic energy (IKE) for each composite leg was computed using the following equation:

$$IKE = \frac{\rho_o \Delta z}{2} \int_0^{2\pi} \int_0^R v^2 r dr d\theta, \quad (6.1)$$

where v is the tangential wind, ρ_o is the density (0.9 kg m^{-3}), and Δz is a 1 km depth of the atmosphere. The IKE for the intensification, weakening, and reintensification phases were $3.6 \times 10^{16} \text{ J}$, $4.2 \times 10^{16} \text{ J}$, and $4.6 \times 10^{16} \text{ J}$ respectively. The combination of a larger RMW and an increase in storm strength produces a 28% increase of IKE during the ERC, even though there is a small decrease of maximum intensity. This behavior has been previously documented by Maclay et al. (2008). In addition to the RMW increasing, the hurricane wind field expands from 94 km during the intensification phase to just beyond 150 km towards the end of the ERC. This is nearly a 70% increase in the hurricane wind field.

Hurricanes naturally expand their wind field with age and increasing latitude (Weatherford and Gray 1988a; Kimball and Mulekar 2004; Kossin et al. 2007). ERCs can take on order of a day or two to complete, so it is necessary to compare the increase of the outer wind field specifically associated with ERCs to a larger sample of outer wind field changes over a specific time interval. The SEF database, detailed in chapter 2, is utilized to increase the sample size of SEF events. If a mean of all available radial legs 12 h before SEF (pre-SEF) are compared with a mean profile of all available radial legs 12 h after SEF (post-SEF), then the entire ERC is not required to be observed by aircraft. The mean of the pre-SEF radial legs was subtracted from the mean post-SEF profile to determine the average outer wind field increase as a result of the hurricane undergoing an ERC. The same procedure, using a Monte Carlo approach, was then carried out for 5000 random “SEF times” from the remaining pool of hurricanes in the full flight-level dataset of ~6000 radial legs. For each random time the storm was required to be at

hurricane intensity. The difference profiles were binned into 15 10 km regions and the distribution is compared with the mean SEF difference profile (Fig. 6.12).

The increased outer wind field, that is a product of an ERC, far exceeds those changes from the Monte Carlo distribution, which exhibit a near equal chance for wind speed increases and decreases for the entire radial leg. From 70 km to beyond 150 km the wind field expansion related to an ERC far exceeds the 75th percentile of climatological changes for the same 12 h interval. Since hurricanes generally increase to maximum lifetime intensity (LMI) and then begin to weaken, a repeat analysis that divided the SEF events into respective pre-LMI and post-LMI classes was performed to further securitize the above result. The same LMI ratio of the SEF events was maintained during the Monte Carlo sampling and revealed very similar results. These large increases associated with SEF are robust and can occur over a short time period requiring the storm to obtain energy resources effectively and to use the energy efficiently.

Hurricane Wilma (2005) has an extraordinary rate of intensification from 1200 UTC 18 October to 1200 UTC 19 October. No other Atlantic storm has matched the 95-kt increase in a 24 h period (Beven et al. 2008). Additionally, Wilma also holds the record for the lowest estimated minimum pressure ever in the Atlantic, 882 mb, which occurred at the end of the rapid intensification (Beven et al. 2008). When this record low pressure was observed there was already a well-developed secondary wind maximum. As this maximum contracted and intensified, Hurricane Wilma had a dramatic increase in IKE (Fig. 6.13).

In general, the IKE mimics and lags the evolution of the maximum intensity, but the outer wind field is responsible for the large increase of IKE. Between 1800 UTC 19 October and

0600 UTC 20 October, Wilma was an intense tropical cyclone with an extremely small 2 nm eye, but maximum flight-level winds weakened within the inner eyewall (Fig. 6.13b). During this 12 h period, the Hovmöller diagram shows a large region of increasing winds in the outer wind field (Fig. 6.13a). Despite the storm weakening, the IKE increased roughly 35% during this period and eventually the storm re-intensifies as the outer eyewall becomes the dominant eyewall. Weatherford and Gray (1988a,b) identified this inverse relationship between intensity and the outer wind field for Western Pacific typhoons and more recent studies observed this relationship during ERCs (Croxford and Barnes 2002; Maclay et al. 2008). To add some perspective for this specific case, the 24 h increase of IKE in Wilma from 0000 UTC 19 October to 0000 UTC 20 October is similar to the IKE of Hurricane Dennis (2005) when it made landfall on the Florida panhandle as a category 3 hurricane.

Part of Wilma's explosive intensification and concurrent IKE increases may be explained through efficiency arguments (Schubert and Hack 1982; Shapiro and Willoughby 1982; Nolan et al. 2007; Rozoff et al. 2011). Efficiency may have been high not only right near the vortex center, but also well beyond 50 km from storm center. The collocation of localized heating and vorticity allows for the storm to reduce the Rossby radius of deformation to focus energy, while the secondary wind maximum increases the inertial stability in a localized region. The remainder of this work uses the Rankine parameters, along with thermodynamic flight-level data, to examine more closely the dynamics that occur within the inner-core during an ERC.

Table 6.1 Mean and standard deviations for r_1 , r_2 , v_1 , and v_2 changes during each ERC phase. The mean and standard deviation is also given for the time required to complete each phase, the time to complete an entire ERC, and the amount of time until concentric eyewalls first appear on microwave imagery.

	Intensification		Weakening		Reintensification	
	Mean	Std.	Mean	Std.	Mean	Std.
r_1 (km)	-7.0	11.5	-1.4	6.9	-2.2	8.0
r_2 (km)	-14.8	18.8	-28.8	15.9	-12.7	12.1
v_1 (m s ⁻¹)	7.0	9.3	-10.2	5.6	-7.5	7.0
v_2 (m s ⁻¹)	4.7	5.6	9.2	7.2	3.9	4.1
Time (h)	9.4	9.1	16.6	8.6	10.7	12.6
	Length of ERC		Microwave Appearance			
	Mean	Std.	Mean	Std.		
Time (h)	36.3	13.4	17.5	10.7		

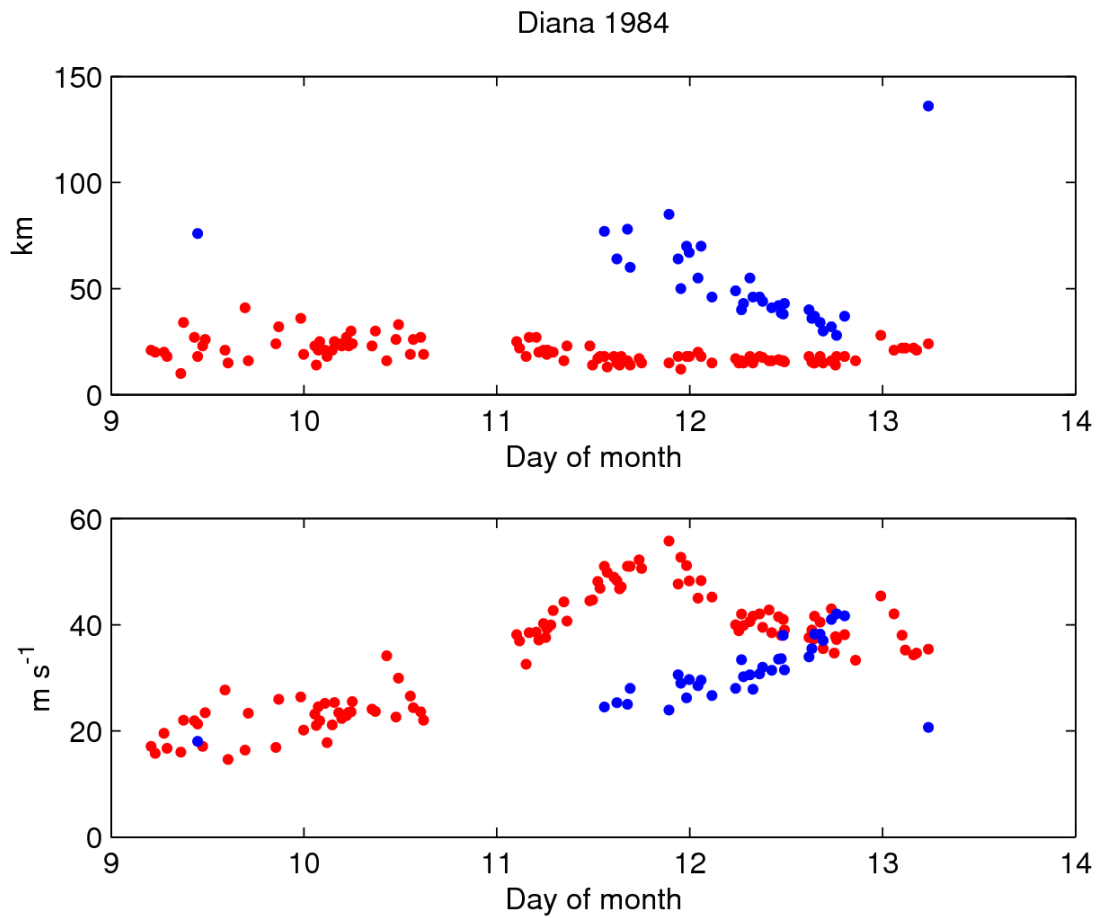


Figure 6.1 *Top panel:* The evolution of radii parameters r_1 (red) and r_2 (blue). *Bottom panel:* The evolution of intensity parameters v_1 (red) and v_2 (blue) for Hurricane Diana (1984).

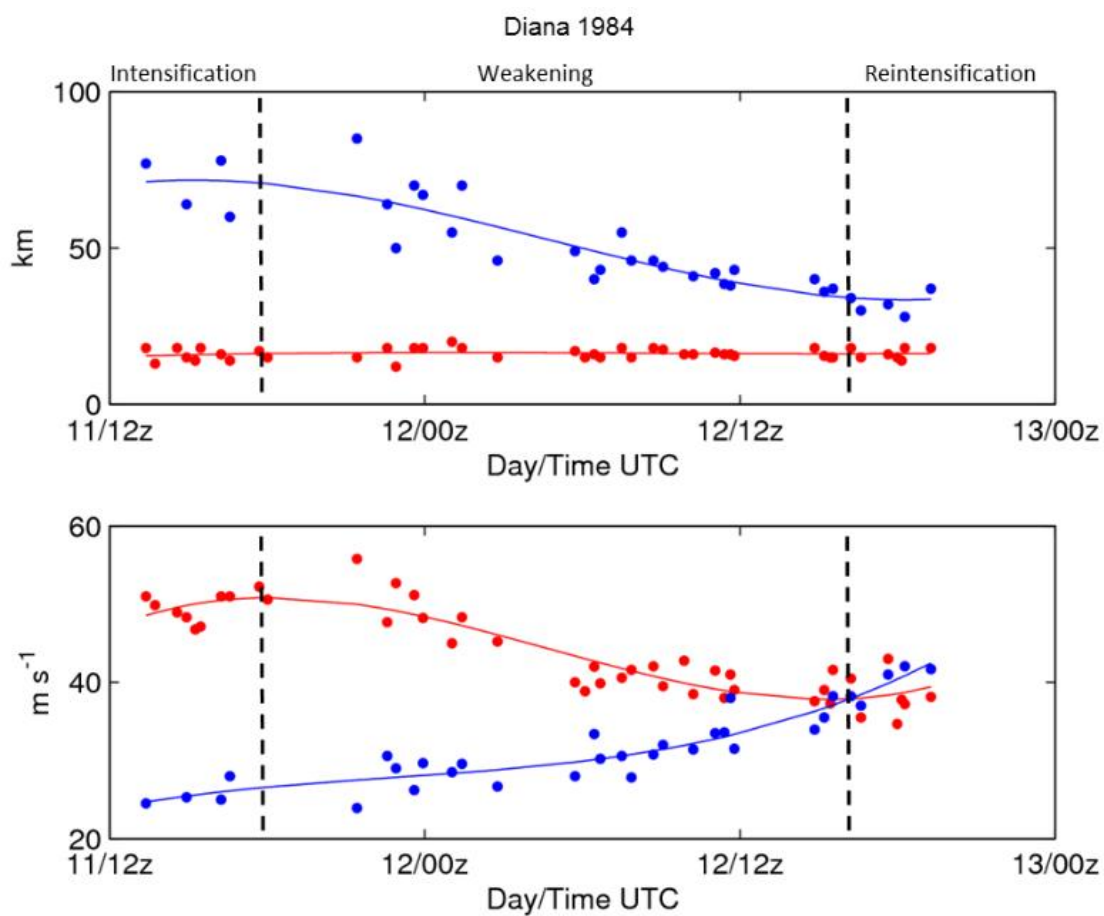


Figure 6.2 As in Fig. 6.1, but only during the ERC. Each time series of wind profile parameters is fit with a polynomial best fit (solid lines). Vertical dashed lines separate phases of the ERC, determined from the evolution of the maximum intensity.

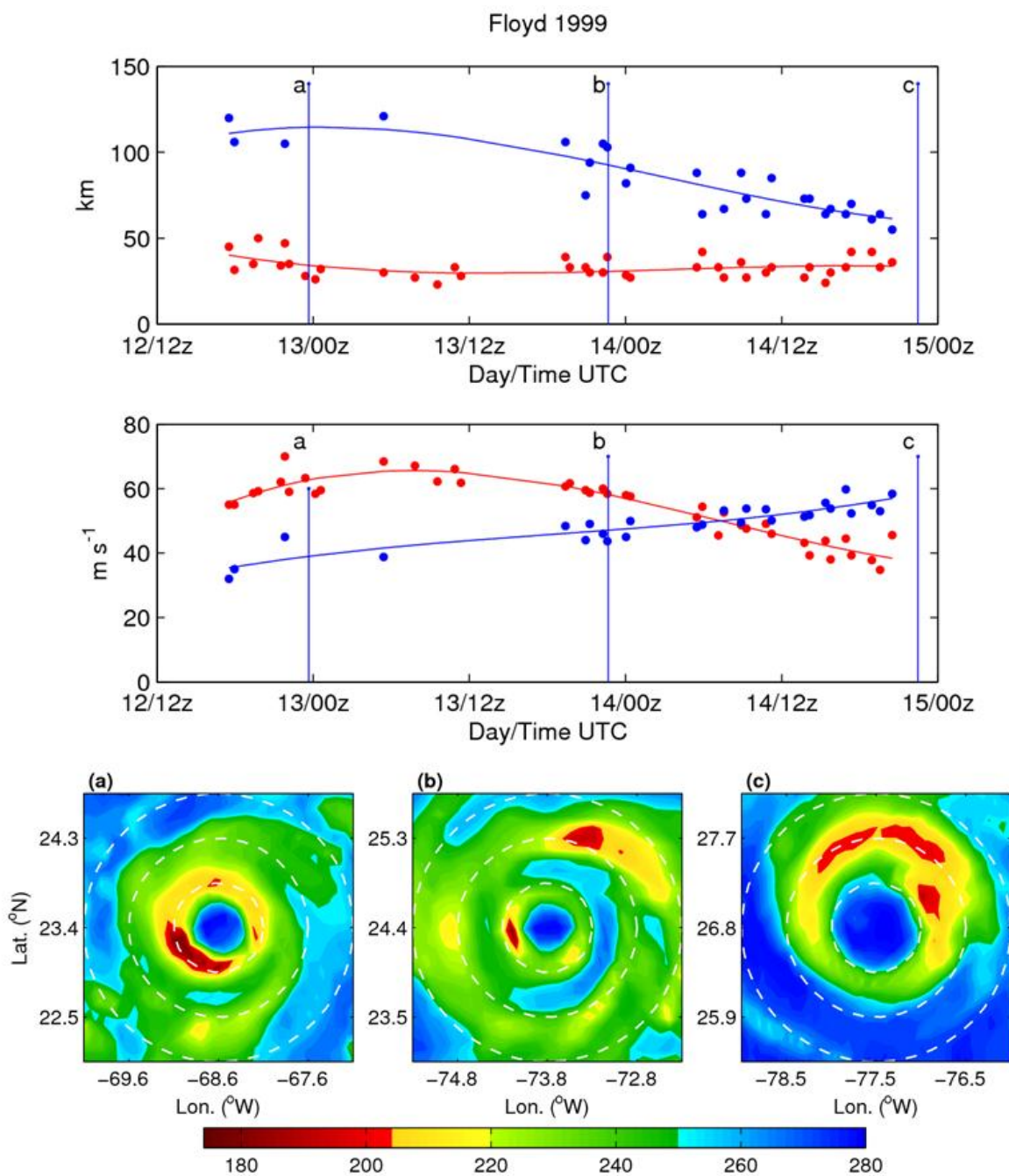


Figure 6.3 *Top*, as in Fig. 6.2, but for a Hurricane Floyd (1999) ERC. The lettered vertical lines correspond to the times when the inner-core was observed by microwave instrumentation. *Bottom panel*, 300 x 300 km storm-centered 85 GHz SSM/I imagery of brightness temperatures (K) taken at *a*) 2340 UTC 12 September, *b*) 2240 UTC 13 September, and *c*) 2228 UTC 14 September for Hurricane Floyd (1999). White range rings denote radial distances from storm center of 50, 100, and 150 km.

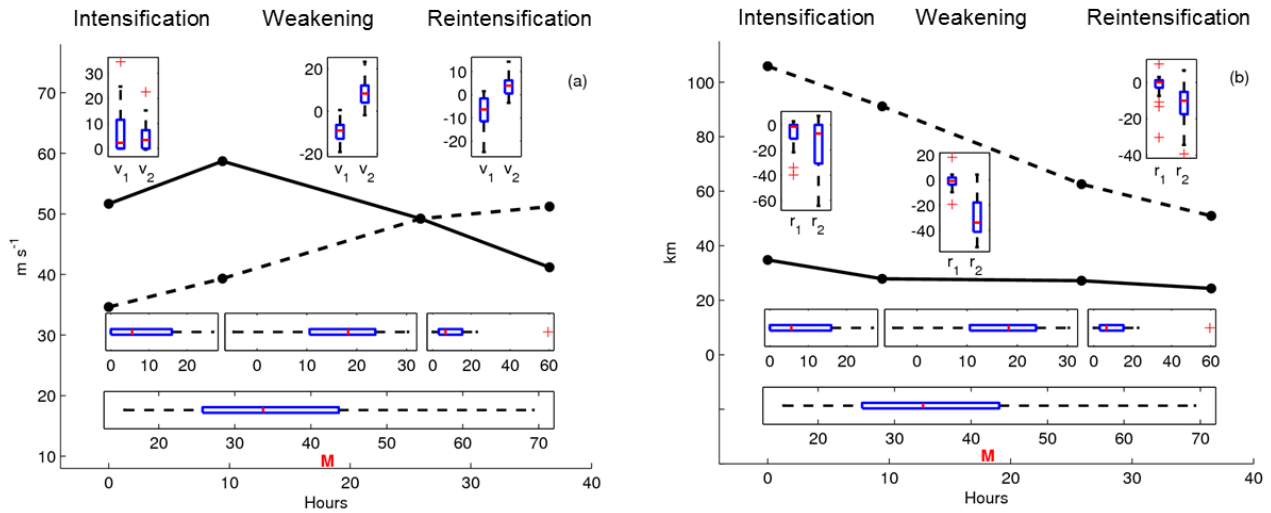


Figure 6.4 a) Composite analysis of intensity changes associated with the inner wind maximum (v_1 , solid black line) and outer wind maximum (v_2 , dashed black line) for 24 ERC events. The ERC is broken into 3 phases: intensification, weakening, and reintensification. Associated with each ERC phase are vertical boxplots depicting the spread of the intensity changes, in m s^{-1} , for each phase. Horizontal boxplots depict the range of time (h) associated with each phase⁶. The bottom horizontal boxplot represents the range of time required to complete an entire ERC. The red M is the average of the best estimated time when double eyewalls with a well-defined moat first appear on microwave imagery after an outer wind maximum has been detected. b) As in (a), but for radii changes of r_1 and r_2 measured in km.

⁶ The inner wind maximum was able to intensify in tandem with the outer eyewall even after the intensities intersected during Hurricane Dean (2007). Since the inner wind maximum reached peak intensity after the intersection of intensities a negative time appears for the weakening phase of the composite analysis.

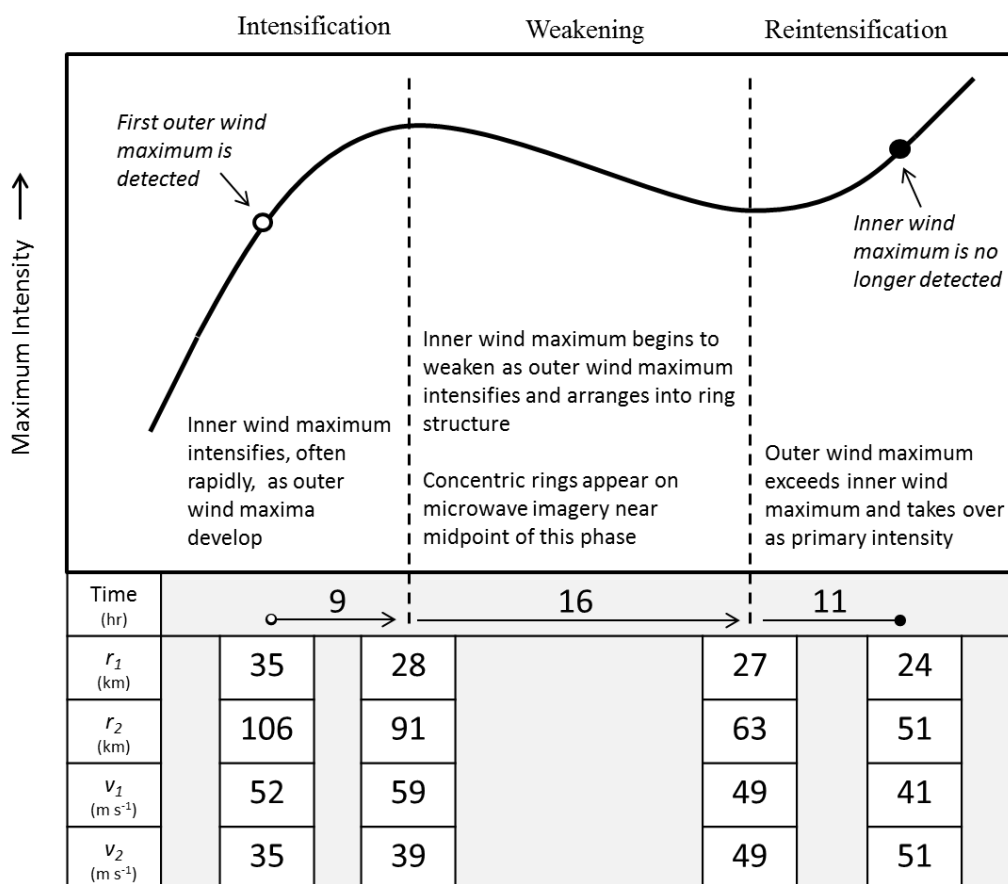


Figure 6.5 Schematic of the maximum intensity evolution during 3 phases of an ERC. The average amount of time to complete each phase, along with the average values of the Rankine parameters, as determined from the third-order polynomial fits, are listed for the start and end of the ERC, as well as the transition of phases.

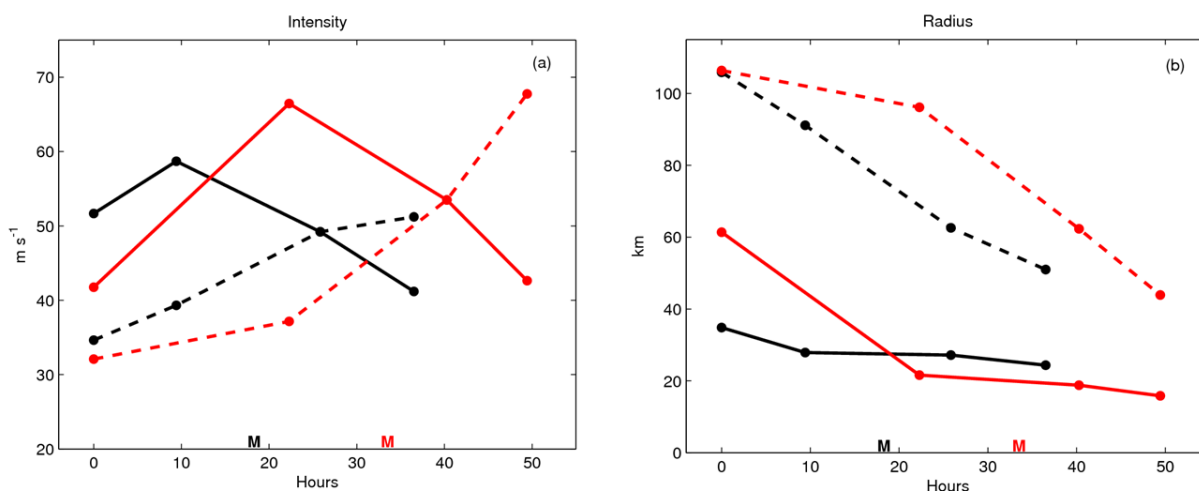


Figure 6.6 a) Composite analysis of the intensity changes associated with the inner wind maximum (solid black line) and outer wind maximum (dashed black line) for 24 ERC events for all three ERC phases. The black lines are identical to those that appear in Fig. 6.4. The solid red line and dashed red line mark the intensity changes for inner and outer wind maximum changes respectively for a single ERC during Ivan (2004) that occurred on 11 and 12 September. The black M is the average of the best estimated time when double eyewalls with a well-defined moat first appear on microwave imagery after an outer wind maximum has been detected. The red M represents when double eyewalls are estimated to have first appeared on microwave imagery for this particular Ivan ERC. b) As in a, but for radii.

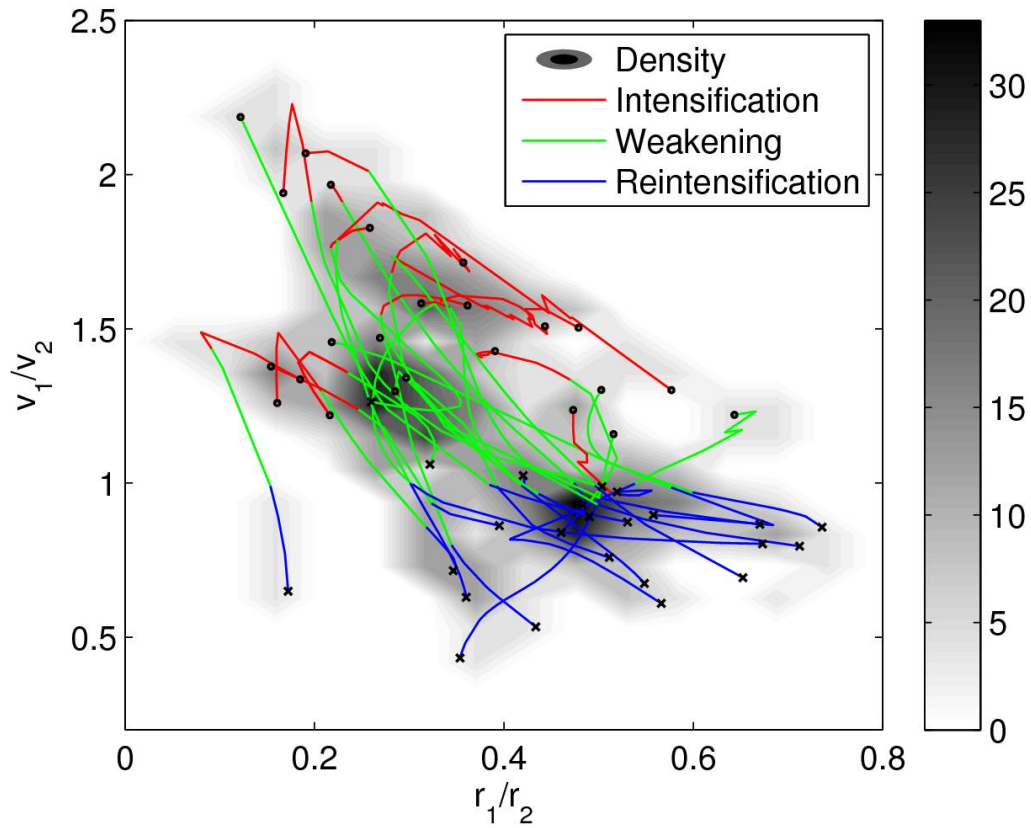


Figure 6.7 A phase diagram of r_1/r_2 versus v_1/v_2 for 24 ERC cases. The entire polynomial fits of the Rankine parameters are used. Shading represents the density (%) of an ERC event passing through an existing radius ratio and intensity ratio pair. The red, green, and blue portion of each line represents the intensification, weakening, and reintensification phases respectively. Black dots and X's indicate the start and end time an ERC.

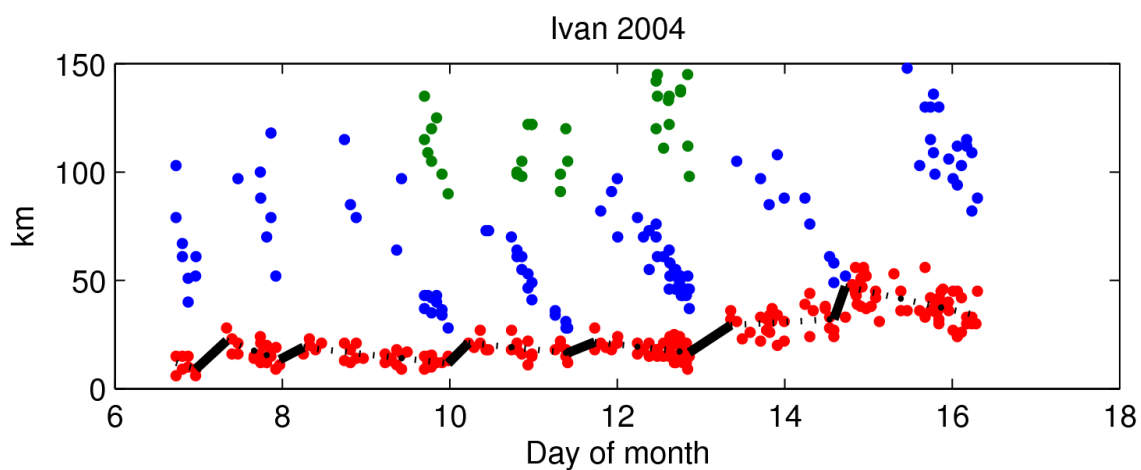


Figure 6.8 Evolution of Rankine parameters r_1 (red dots) and r_2 (blue dots) for Hurricane Ivan (2004). Green dots indicate the location of triple wind maxima. Black lines are linear interpolations of the inner radius, r_1 . The dotted line captures the contraction of r_1 and the solid black line highlights the jump in eye size associated with the transitioning of the outer wind maximum to the primary wind maximum.

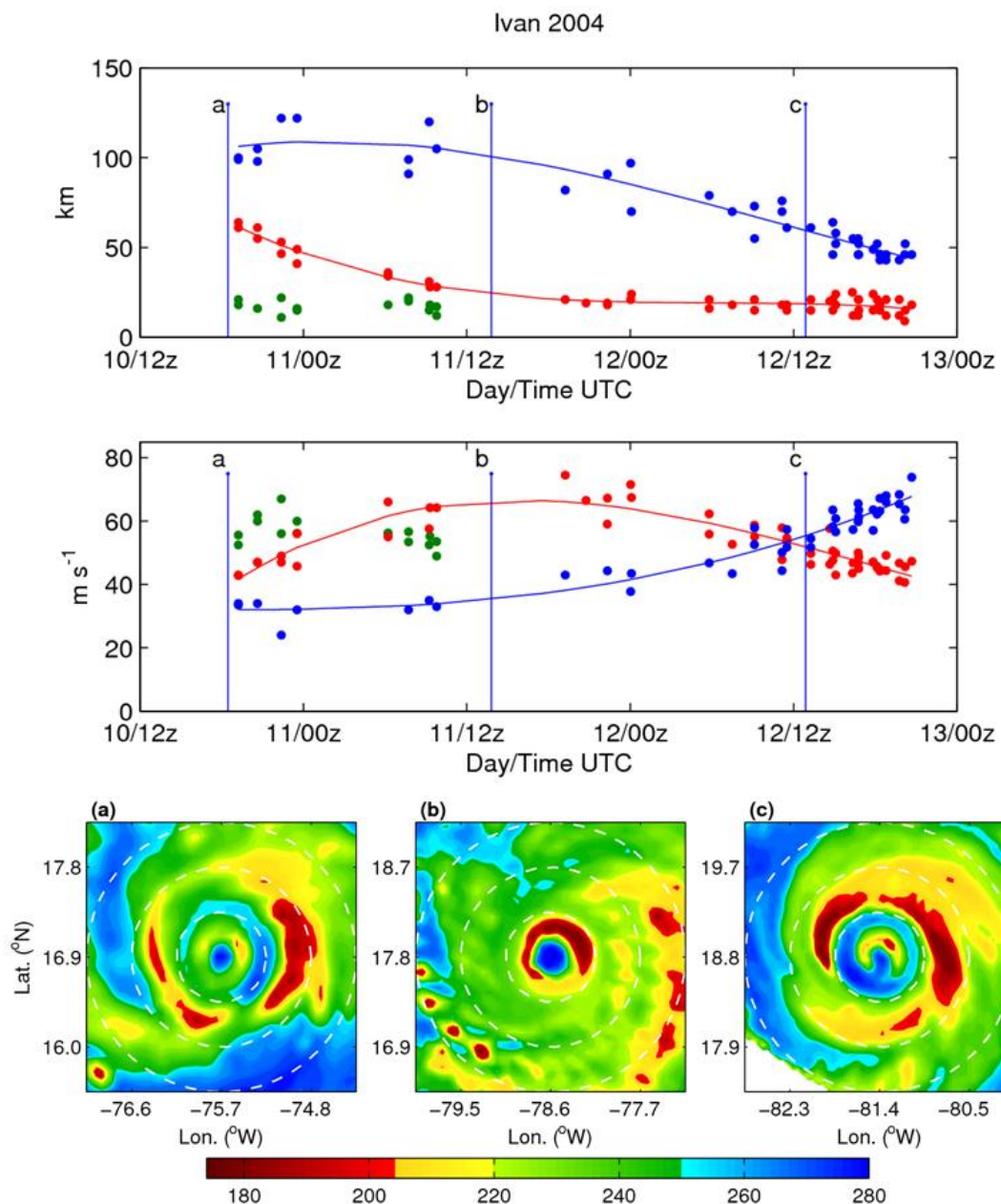


Figure 6.9 As in Fig. 6.3, but for an ERC in Hurricane Ivan (2004). *Top*, the green dots represent the radius (top panel) and intensity (bottom panel) of the decaying innermost eyewall. *Bottom*, Microwave images are from 1828 UTC 10 September (AMSRE), 1348 UTC 11 September (TMI), and 1252 UTC 12 September (TMI).

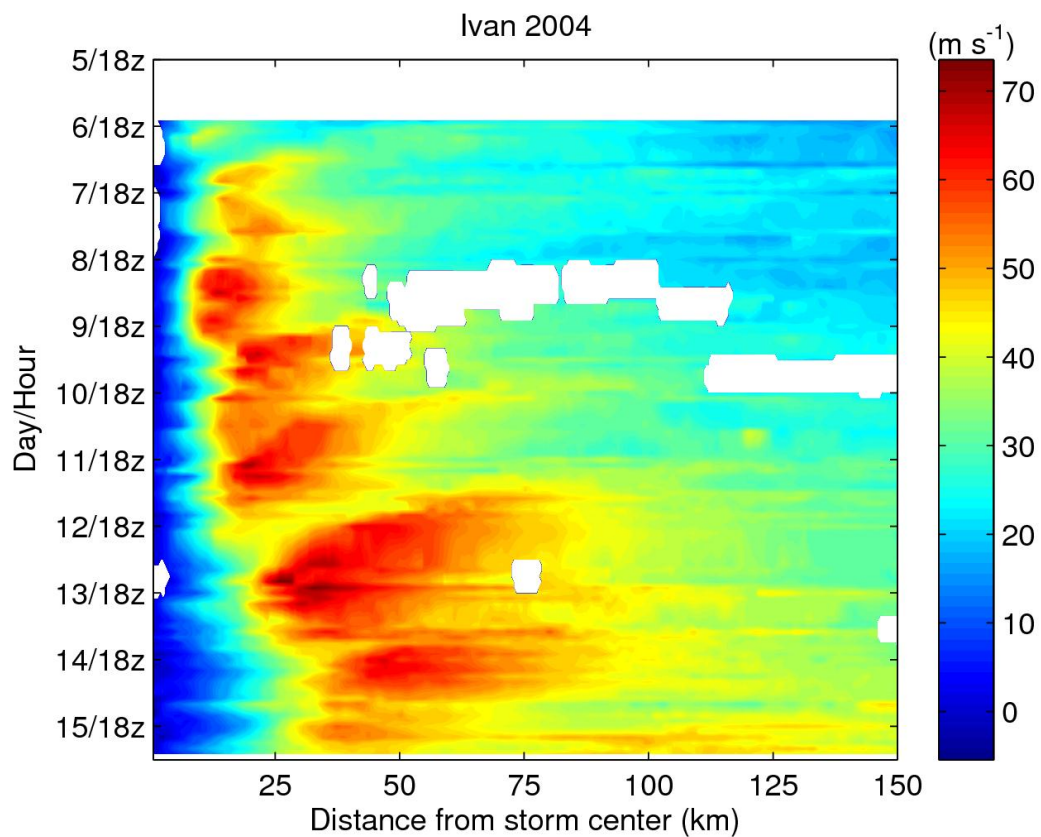


Figure 6.10 Hovmöller diagram of flight-level radial profiles of tangential wind for Hurricane Ivan (2004) during the month of September. Radial leg profiles extend from storm center (0 km) out to 150 km. Time increases toward the origin on the y-axis.

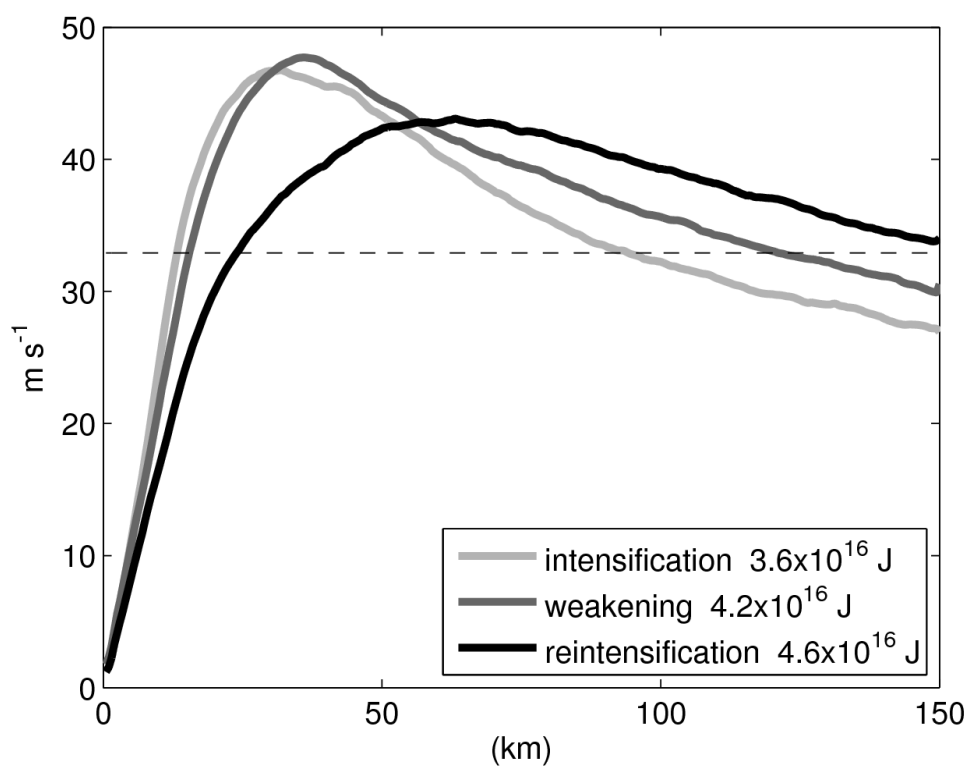


Figure 6.11 Composite analysis of flight-level radial legs and for each of the 3 phases of an ERC and their corresponding IKE values. The dashed line represents hurricane intensity, 33 m s^{-1} .

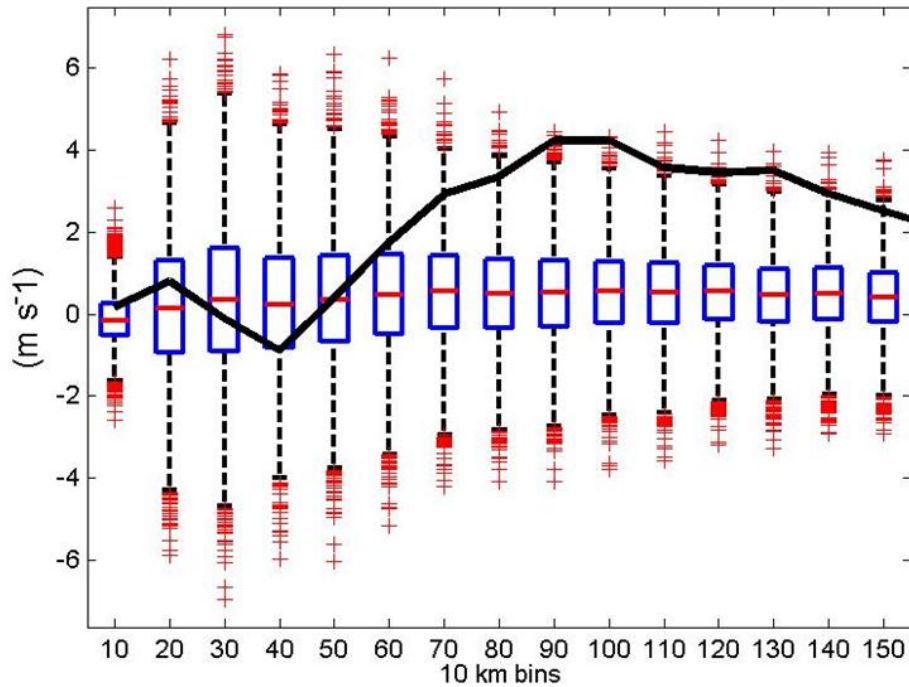


Figure 6.12 Comparison of intensity changes associated with ERCs and a climatology of hurricane intensity changes. The black line represents the difference between the mean pre-SEF profile, all available radial legs 12 h before SEF, compared with the mean post-SEF profile, all available radial legs 12 h after SEF for 15 10 km bins. The 15 boxplots display the distribution of 5000 random hurricane intensity changes that followed the same procedure, i.e. 5000 random times were selected and all available radial legs 12 h before and after this time were used in the analysis.

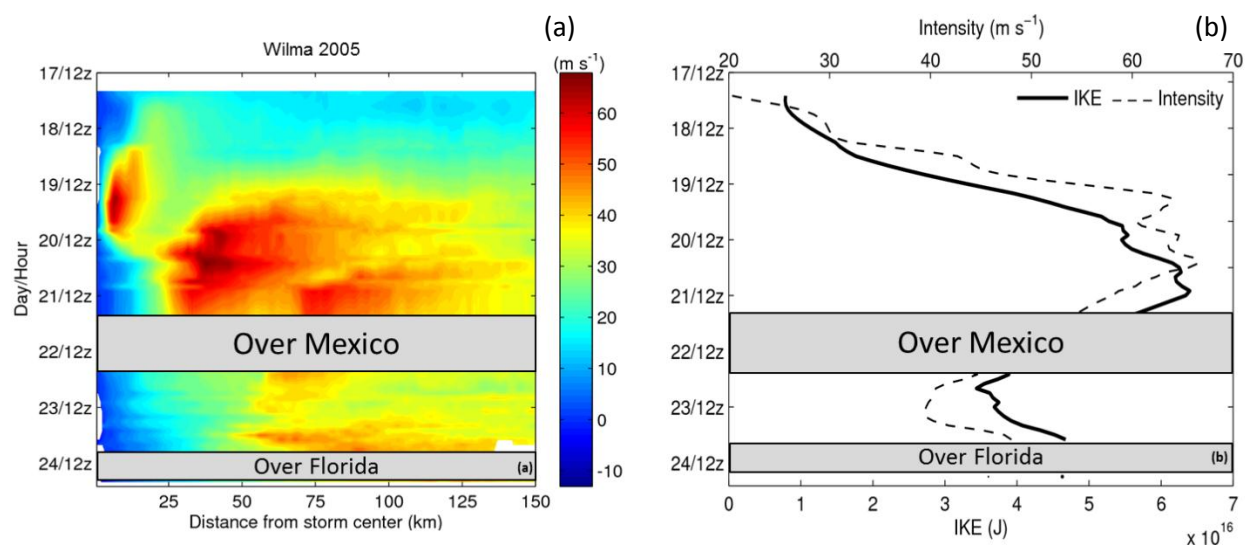


Figure 6.13 a) As in Fig. 6.10 but for Hurricane Wilma (2005) during the month of October. b) Evolution of Wilma (2005) flight-level intensity (dashed line) and IKE (solid line). Time increases toward the origin on the y-axis. 95% of data from each radial leg was required to calculate IKE. Gray boxes indicate when Wilma was over land.

Chapter 7 Thermodynamic Analysis

Wind changes weather
and we can see why.
It blows clouds along
and clears rain from the sky.

- *Dr. Seuss, “Oh Say Can You Say What’s the Weather Today”, discussing the transverse circulation of a hurricane...of course.*

During an ERC, the complex interaction of the secondary circulations of both eyewalls plays a major role in the evolution of the thermodynamic structure of the inner-core, which can be dramatic and highly variable. This chapter sets out to document the variability of these changes by comparing flight-level temperature, dewpoint, relative humidity, and θ_e at the start and end of the 24 ERCs used to develop the kinematic climatology in the previous chapter.

All of the radial legs that were flown within the first and last 3 hours of each ERC are divided into three regions based on flight-level measurements of tangential wind and the double modified Rankine vortex: the region from storm center to r_1 (eye), the region between r_1 and r_2 (moat), and the region from r_2 to the end of the radial leg (far field). Fig. 7.1 illustrates typical changes in the convective presentation during an ERC and its relationship to these three regions. Toward the end of an ERC, the eye and moat regions together make up the new developing post-ERC eye.

The changes in the distributions of flight-level thermodynamic variables between the start and end of an ERC are shown in Fig. 7.2. Flight-level thermodynamic variables are highly

dependent on the altitude of the aircraft, so only measurements collected at 700 mb, the most common isobaric flight-level, are used in this analysis. When radial legs from all pressure levels are normalized through the use of a fixed tropical atmosphere sounding (e.g., Dunion and Marron 2008) and combined, the thermodynamic variables exhibit essentially the same behavior as shown in Fig. 7.2.

All three regions warm between the start and end of an ERC (Fig. 7.2a). The largest temperature increase occurs in the moat, where warming increases the mean temperature by more than 2°C (Fig. 7.2a). Persistent subsiding air from both eyewalls (Dodge et al. 1999; Houze et al. 2007; Rozoff et al. 2008) is likely responsible for the warming in the moat. While the eye does show warming between the start and end of an ERC the eye is typically cooling during the weakening and reintensification phases of an ERC, which account for the majority of time. The reason why temperatures are shown to be warmer at the end of an ERC is because, similar to the intensity, temperatures in the eye are increasing during and peak at the end of the intensification phase. An alternate way to view these changes near the primary eyewall region that aren't limited to sampling only the first and last 3 h of an ERC, include more radial legs, and maintain more structure is shown in Fig 7.3.

The dramatic cooling and moistening in the eye is highlighted when all the radial legs are normalized by r_1 and are divided into two classifications: when v_1 or v_2 is the maximum intensity of the radial leg. Using this criterion allows the inclusion of portions of ERCs that were not fully sampled by aircraft. These classes, however, can generally be thought of as the combination of the intensification and weakening phases compared to the reintensification phase. Just inward of r_1 , when v_1 is the maximum intensity, there is a dramatic warming and drying (Fig. 7.3).

Dewpoint depressions in the eye that exceed 5°C are reduced by more than half once the outer wind maximum becomes the primary intensity. An increase in temperature and dewpoint beyond r_1 is also observed.

Returning to the analysis of the complete 24 ERCs dataset, dewpoint also increases significantly in all three regions between the start and end of an ERC (Fig. 7.2b). Dewpoint temperatures in the eye typically increase during the weakening phase of an ERC, which may be a result of a rising inversion level (Jordan 1961; Franklin et al. 1988), the ascension of a hub cloud to flight-level (e.g., Schubert et al. 2007), mixing of eyewall air into the eye (Kossin and Eastin 2001), or a combination of these processes. The increase of dewpoint in the moat may be due to changes in subsidence and associated changes in inversion level, or may be due to precipitation or advective processes. Previous studies have shown that radar bright bands can exist in the moat and precipitation can be very asymmetric and intense. A radar image of Hurricane Rita (2005), for example, shows a band of high reflectivity (>30 dBZ) spiraling into a well-developed moat from the eyewall, while an echo-free region exists in a nearby portion of the moat (Didlake and Houze 2011; their Fig. 3a).

As dewpoint temperatures increase, relative humidity in the eye and far field regions increase significantly between the start and end of an ERC (Fig 7.2c). However, mean relative humidity in the moat decreases because the temperature increase exceeds the increase of dewpoint temperatures in this region (Fig. 7.2c). At the end of an ERC, the relative humidity distribution of the moat is very similar to the distribution of the eye region (Fig. 7.2c; also cf. Houze et al. 2007). Flight-level relative humidity values in both of these regions, which together account for the total area of the developing post-ERC eye, are substantially higher than those found in the eye at the

start of the ERC. It should be noted, however, that some hurricanes (e.g., Gilbert 1988, Wilma 2005) exhibit especially pronounced warming and drying in the moat and contain much lower relative humidity values than in the eye region. These hurricanes usually have prominent outer wind maxima forming a wall of high inertial stability early on during an ERC while inner eyewall convection is still active. This may allow for upper-level exhaust from two convectively active eyewalls to subside in the moat, generating substantial warming and drying at flight-level (Rozoff et al. 2008).

Despite the similar flight-level relative humidity distributions at the end of an ERC, the eye and moat regions contain distinctly different air masses, as evident in their distributions of flight-level θ_e (Fig 7.2d). The difference of their means is roughly 10 K. This difference is large enough to overcome any remaining instrumentation wetting errors and shows that two separate air masses exist in the developing post-ERC eye. This signal was observed for all 24 ERCs, including Hurricane Rita (2005), a case used here to illustrate a “typical” thermodynamic evolution of the inner-core during the three ERC phases, save for the extremely dry and warm eye at the onset of the ERC (Fig. 7.4).

During Rita’s intensification phase, the eye is warmer and drier than the rest of the inner-core and two distinct θ_e maxima are located along flight-level in the eyewall (Fig. 7.4a). A decrease of inner eyewall convection and wind speed signal the beginning of the weakening phase. In the eye, the temperature decreases and the dewpoint increases to form a θ_e maximum that is contained within the regions of high inertial stability near a radius of 20 km (Fig. 7.4b). An example of this warming and moistening throughout the lower troposphere, instead of one isobaric level, is shown by Houze et al. (2007; their Fig.3).

Temperature and dewpoint increase in the moat region as the ERC progresses (Fig. 7.4b,c). Toward the end of the ERC, warming and drying are focused along an annulus of the developing eye just inward of the outer wind maximum near 30 km (Fig. 7.4c). Dewpoint depressions eventually become more pronounced and expand to cover a large region of the post-ERC eye (Fig. 7.4d). The relevance of this selective warming and drying is discussed further in the next chapter.

At the end of the ERC, the air mass defining the new larger developing eye is not a homogenous air mass, and θ_e is substantially greater within the relict inner eyewall circulation than the surrounding moat (Fig. 7.4c,d). Since convection in the region of the inner wind maximum is largely absent during the end of the reintensification phase, θ_e is approximately conserved and serves as a useful marker for distinguishing air masses of differing origins. The θ_e increase is not gradual, but rather a sharp radial gradient exists at the inner edge of the relict inner eyewall circulation and its associated high inertial stability (Fig. 7.4c). In the case of Hurricane Rita, θ_e increases more than 10 K over a distance of less than 10 km inward of the relict inner eyewall circulation. This gradient defines the separation of the two air masses (i.e., the original moat and inner eye) and can persist after the completion of an ERC (Fig. 7.4d). Microwave brightness temperatures can appear nearly uniform across the post-ERC eye (e.g., Fig. 7.1b) and the relict inner eyewall circulation can be difficult to identify in a flight-level tangential wind profile (Fig. 7.4d).

The relict inner eyewall circulation may appear to be a desultory, insignificant feature, as it accounts for only 15% of the area in Rita's post-ERC eye (Fig. 3d), but it can have substantial ramifications on the subsequent evolution of the storm, which is the focus of the next chapter.

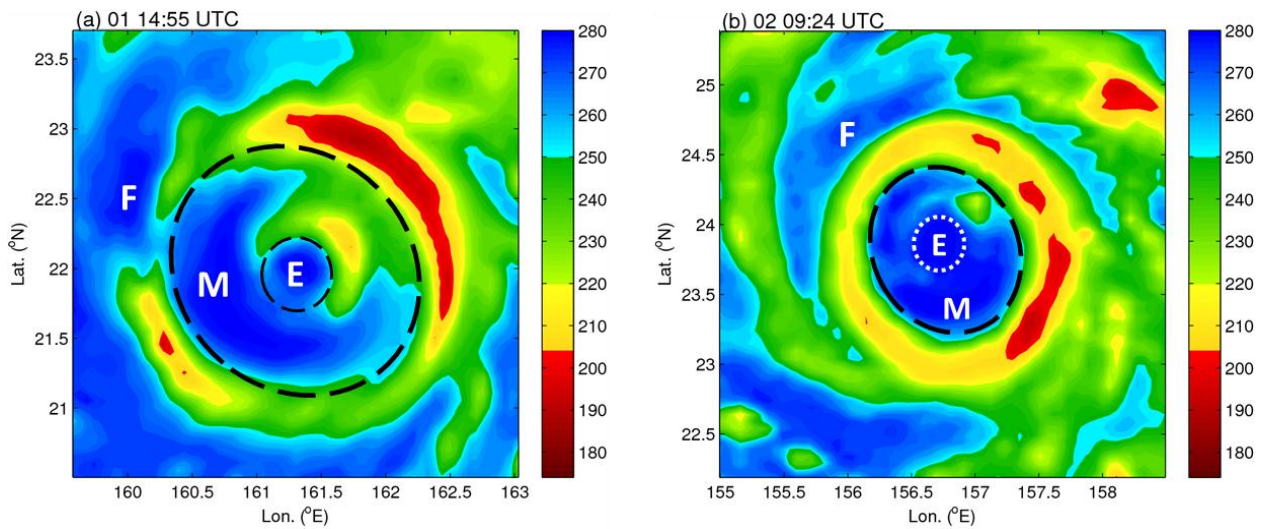


Figure 7.1 Storm-centered 85 GHz imagery of brightness temperatures (K) of Hurricane Ioke (2006) taken at (a) 1455 UTC 01 Sep. (AMSR-E) and (b) 0924 UTC 02 Sep. (TRMM-TMI). The typical changes in the convective presentation of the inner-core during an ERC and its relationship to the three regions are shown. The letters E, M, and F represent the eye, moat, and far-field regions respectively. The relict inner eyewall circulation (contained within the white dashed ring) and moat region together make up the developing post-ERC eye.

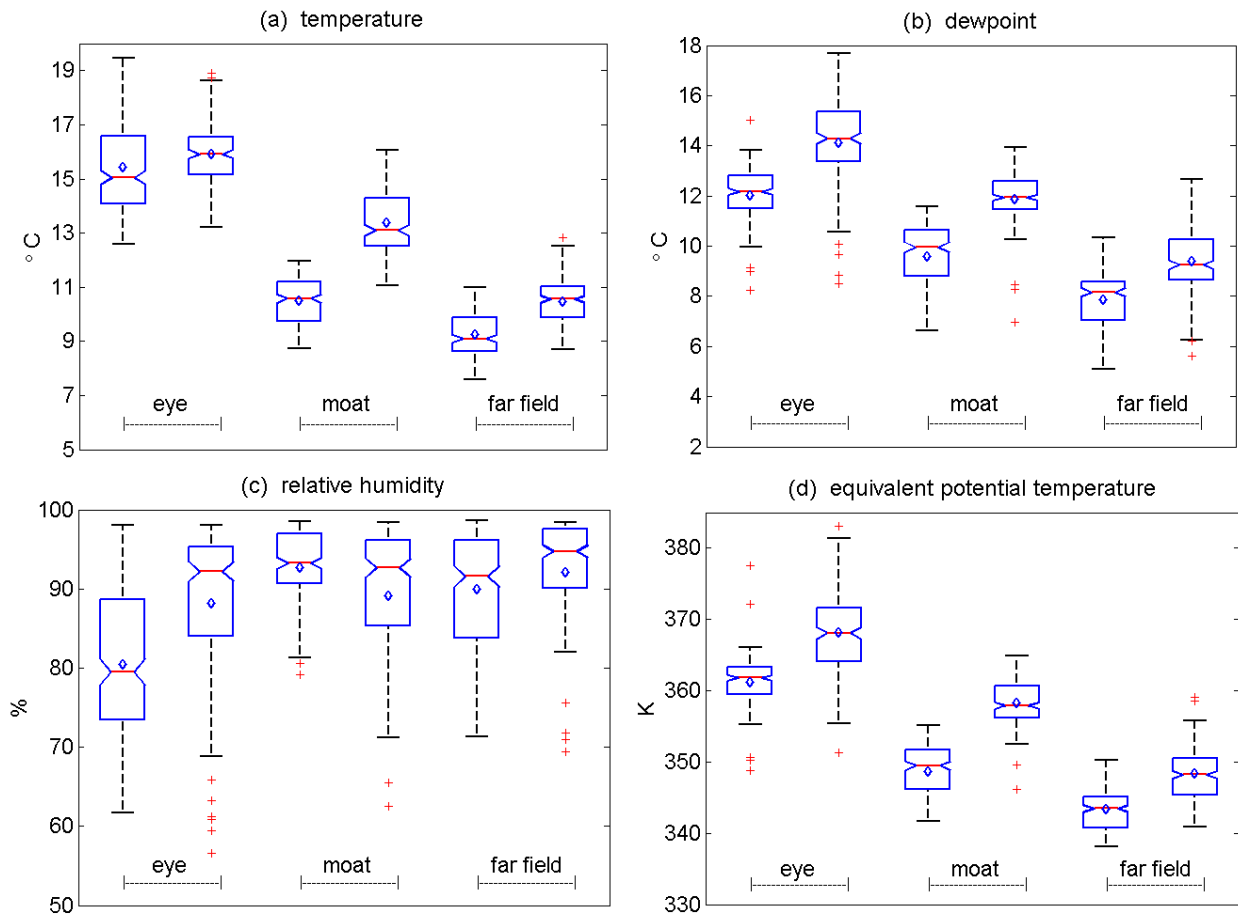


Figure 7.2 Comparisons of flight-level thermodynamic data at the start and end of the 24 SKR11 ERCs. All plots are based on the mean flight-level measurements along the 700 mb level within each region. For each region, the boxplot on the left (right) is based on the first (last) 3 h of the ERC. The medians at the start and end of an ERC in each region are significantly different at the 5% significance level if the widths of the notches centered on the medians do not overlap. The blue diamond represents the mean of the data. The four panels show changes in flight-level (a) temperature, (b) dewpoint, (c) relative humidity, and (d) θ_e .

Temperature and Dewpoint when a Secondary Wind Maximum is Present

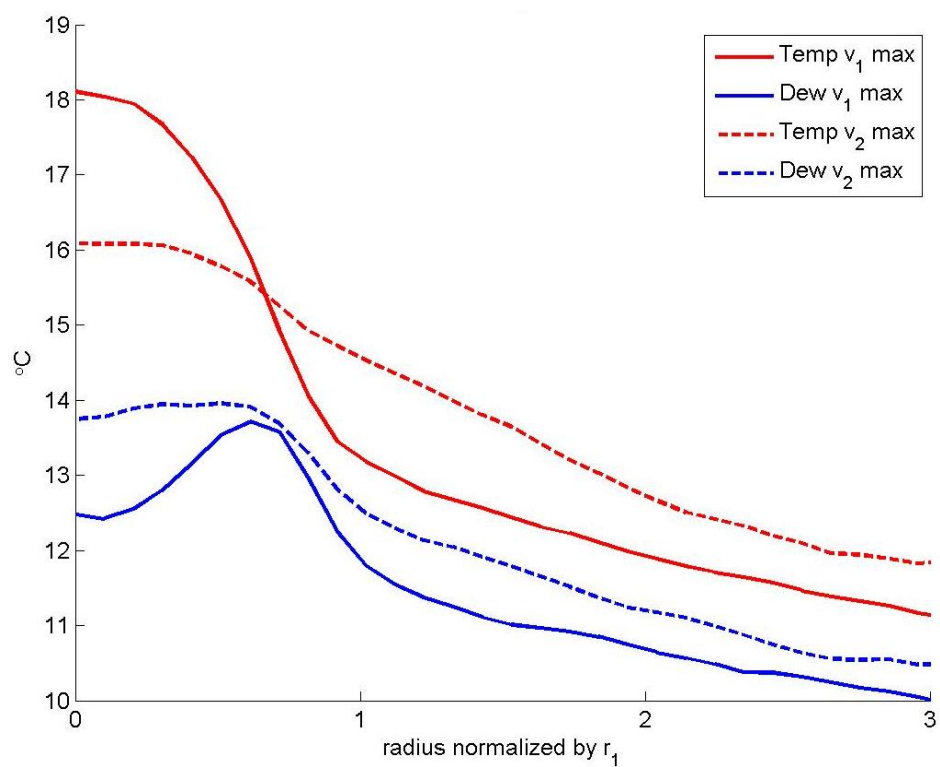


Figure 7.3 Comparisons of flight-level (700 mb) composite temperature (red) and dewpoint (blue) profiles. The solid (dashed) line indicated that v_1 (v_2) was the maximum intensity of the radial leg. The profiles are normalized by r_1 .

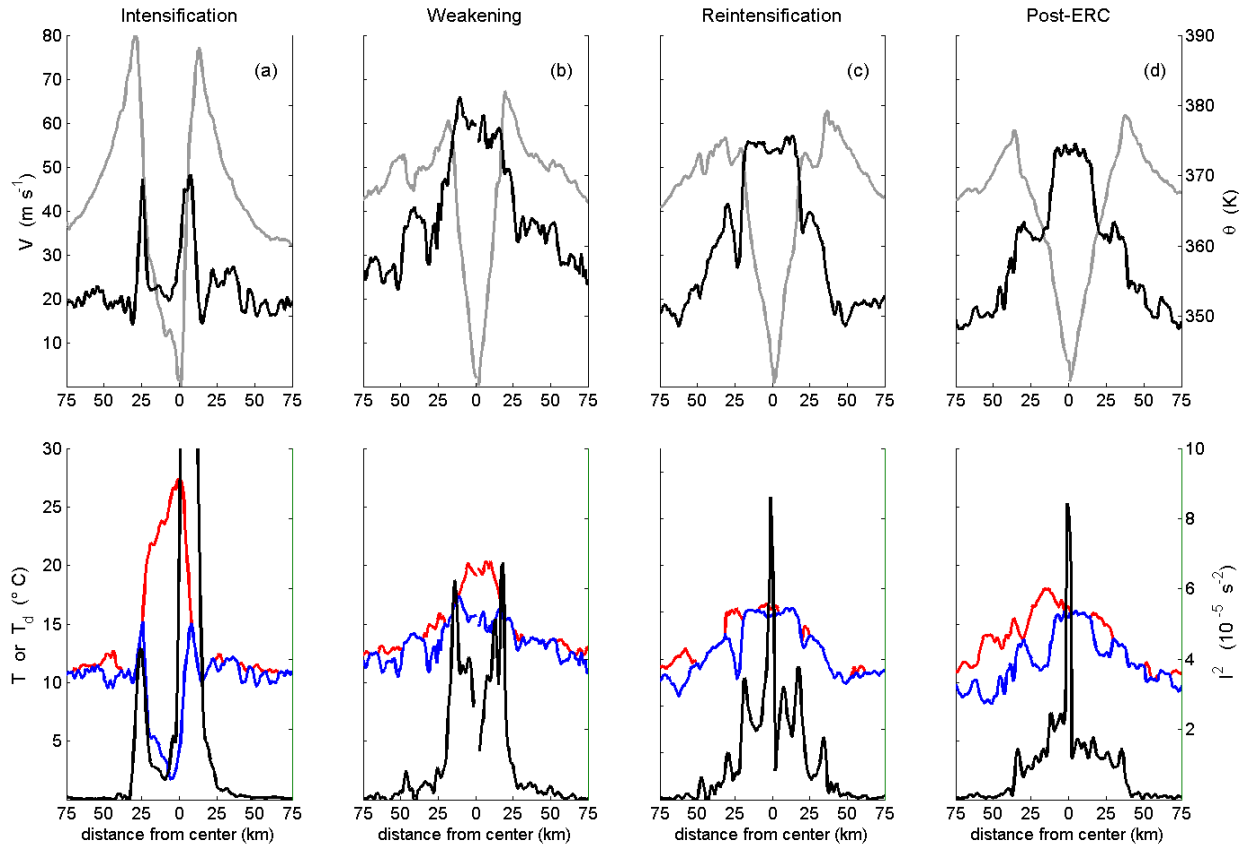


Figure 7.4 Hurricane Rita (2005) flight-level measurements along the 700 mb level from storm center out to 75 km. The top panels display tangential wind (gray) and θ_e (black). The bottom panels display temperature (red), dewpoint (blue) and inertial stability (black). Measurements were taken during the (a) intensification phase at 1937 UTC 21 Sep. (the inertial stability near storm center exceeds the maximum value of the y-axis), (b) weakening phase at 1619 UTC 22 Sep., (c) reintensification phase at 0145 UTC 23 Sep., and (d) post-ERC period at 0600 UTC 23 Sep.

Chapter 8 Relict Inner Eyewall Circulation

Big whorls have little whorls
 That feed on their velocity,
 And little whorls have lesser whorls
 And so on to viscosity.

– *Lewis F. Richardson*

The inner-core during an ERC consists of calm winds near storm center that rapidly increase to a maximum at the primary eyewall. The outer eyewall, located at a more distant radius, usually contains a secondary wind maximum with relatively enhanced vorticity, and the region between the eyewalls consists of a largely convection-free, low-vorticity moat. The region near and just inward of the primary eyewall generally contains high vorticity and is a region of enhanced inertial stability. Inertial stability is defined by $I^2 = (f + (\partial rv/r\partial r))(f + (2v/r))$, where v is the tangential wind, r is radius from storm center, f is the Coriolis parameter, and $(\partial rv/r\partial r)$ is the axisymmetric vertical component of the vorticity vector. An inertially stable region provides resistance to radial motions and is an important factor in the evolution of a hurricane inner-core (Schubert and Hack 1982; Hack and Schubert 1986; Kossin et al. 2000; Schubert et al. 2007; Rozoff et al. 2008; Vigh and Schubert 2009).

Rozoff et al. (2008) hypothesized that the inertial stability of the developing outer eyewall impedes the outflow from the inner eyewall and would reduce inner eyewall convection. Following the demise of the inner eyewall convection, the relict inner eyewall circulation often persists as a well-defined region of high inertial stability that is resistant to horizontal mixing (Zhu et al. 2004; Chen et al. 2011), thereby impacting the local transverse circulation and

potentially limiting subsidence inside the region (Schubert et al. 2007). This impacts the thermodynamic and kinematic characteristics of the eye, as well as the relationship between minimum pressure and maximum wind near the conclusion of an ERC and the hours that follow. Here, flight-level data are used to examine these impacts in detail.

***a.* Hurricane Wilma**

During an ERC in Hurricane Wilma (2005), the flight-level θ_e profile exhibited a pronounced maximum near storm center on the morning of 20 Oct. (Fig. 8.1). The maximum was bounded by high values of inertial stability associated with the relict inner eyewall circulation (Fig. 8.1). We suspect the region of high inertial stability within the relict inner eyewall circulation forms a “containment vessel” that restricts horizontal motions and limits subsidence as it orbits within the larger, developing eye. The moat was warm and dry, with large dewpoint depressions exceeding 7°C at this time while a large portion of the air in the relict inner eyewall circulation was saturated (Fig. 8.1). This provides evidence that subsidence was strong and persistent everywhere except within the relict inner eyewall circulation where inertial stability was greatest. This aspect of the relict inner eyewall circulation has direct implications on both storm structure and intensity.

Figure 8.2 displays the evolution of the surface pressure and flight-level tangential wind profiles during the same ERC in Hurricane Wilma (2005). Surface pressure profiles are calculated from flight-level data in the usual manner, i.e., vertical integration of the hypsometric equation (e.g., Wallace and Hobbs 2006, pages 68-70). For simplicity, we assume that the mean column temperature beneath the aircraft equals the flight-level temperature (isothermal assumption). This assumption introduces a bias since the mean column temperature below the aircraft is typically

warmer than the flight-level temperature, but this bias is mostly irrelevant to the main results of this study.

At 2140 UTC 19 Oct. the tangential wind profile of the inner eyewall was very peaked and the surface pressure was very low (Fig. 8.2a). Nine hours later, at 0650 UTC 20 Oct. the minimum surface pressure had risen and the inner eyewall wind speed had weakened considerably (Fig. 8.2b). The combination of waning convection within the inner eyewall, as evident in microwave imagery (Fig 8.3), and cessation of subsidence over the inner eye likely led to reduced warming in this region and caused the minimum surface pressure to rise (Fig. 8.2).

Microwave imagery also indicates that the relict inner eyewall circulation was located near the outer eyewall at 1845 20 Oct. (Fig 8.3b). Visible satellite imagery (not shown) reveals that the relict inner eyewall circulation had orbited around the larger, developing eye and produced trochoidal motions of the storm center. Trochoidal motions often accompany concentric eyewall structures (Jordan 1966; Oda et al. 2006; Muramatsu 1986), as well as when only a single eyewall is present (Liu et al. 1999; Nolan et al. 2001; Marks et al. 2008; Hendricks et al. 2009). The air mass within the relict inner eyewall circulation maintained its identity and characteristics as it orbited through the much drier environment of the developing eye. This highlights the ability of the inertial stability to restrict radial motions and limit mixing between the two distinct air masses. The trochoidal orbit and longevity of the relict inner eyewall circulation exhibit similar behavior to the idealized model simulations of small offset eyes by Prieto et al. (2001).

The inertial stability within the relict inner eyewall circulation limits the transverse circulation, preventing subsidence within the relict inner eyewall circulation (Schubert et al. 2007),

where the minimum pressure is located (see e.g., Kossin and Schubert 2001, Figs. 8.1 and 8.3). Subsidence-induced warming is focused outside of the relict inner eyewall circulation, typically in an annulus along the inner periphery of the active outer eyewall convection. This warming selectively lowers surface pressure in the annulus and increases the pressure gradient just inward of the outer eyewall (Fig. 8.2b,c), which allows the outer eyewall to more easily contract and intensify (Willoughby et al. 1982; Shapiro and Willoughby 1982; Willoughby 1990; Vigh and Schubert 2009). The localized subsidence-induced warming also transforms the tangential wind into an increasingly “U-shaped” profile (Fig. 8.2), which produces a local vorticity maximum in the eyewall and destabilizes the local flow (Schubert et al. 1999). This can lead to dramatic rearrangements of inner-core thermodynamic and kinematic structure and subsequent changes in storm intensity (Schubert et al. 1999; Kossin and Schubert 2001, 2004; Rozoff et al. 2009; Hendricks and Schubert 2010).

As mentioned previously, vertical integration of the hypsometric equation leads to a biased estimate of surface pressure under an isothermal approximation. The warmer the mean column temperature is compared to flight-level, the greater the high bias. Of particular relevance here, however, is that lapse rates in the outer eyewall and moat are closer to moist and dry adiabatic, respectively, and thus the mean column temperature below flight-level in the convectively active outer eyewall will be cooler than in the moat. This would have the effect of steepening the pressure gradient near the moat/outer eyewall interface even further.

The intensification of Wilma’s outer eyewall winds, likely due in part to the process described above, occurred simultaneously with a steady rise of minimum pressure resulting in an anomalous pressure-wind relationship. The best track data shows that the intensity of the storm

remained at 67 m s^{-1} for 24 h (0600 UTC 20 Oct. to 0600 UTC 21 Oct.) while the minimum pressure increased 29 mb. The result was a highly anomalous pressure-wind relationship – 20 to 30 mb lower than typically expected at the times of Fig. 8.2a,b (Knaff and Zehr 2007, 2008). It should be noted that the ramifications of Wilma's relict inner eyewall circulation are believed to be consistent with other storms (e.g. Fig 7.4d, the region of strongly enhanced θ_e in Rita's post-ERC eye), but the magnitude of Wilma's anomalous pressure-wind is thought to be a rather exceptional example. A detailed examination of the pressure-wind relationship specifically for Wilma was conducted by Kieu et al. (2010).

The relict inner eyewall circulation in Wilma was estimated to have dissipated around 2140 UTC 20 Oct. (Chen et al. 2011). Shortly before this time at 2017 UTC 20 Oct. dewpoint depressions exceeded 5°C in much of the post-ERC eye, but dewpoint values were still highest in a region of high inertial stability that was slightly offset to the right of the storm center (Fig. 8.4a). The radial legs shown in Fig. 8.4a occurred less than two hours after a microwave image showed the relict inner eyewall circulation to be near the inner edge of the northeast eyewall (Fig. 8.3b). When aircraft sampled the inner-core 14 h later, the inertial stability was greatly reduced near storm center and the air masses in the eye had homogenized (Fig. 8.4b). The θ_e range across the eye was less than 5 K and the temperature and dewpoint range across the eye was less than 4°C (Fig. 8.4b). In addition, the best track minimum pressure decreased 4 mb from 0600 to 1800 UTC 21 Oct., even though the intensity decreased 5 m s^{-1} . The pressure decrease may be an indication that subsidence had resumed over storm center.

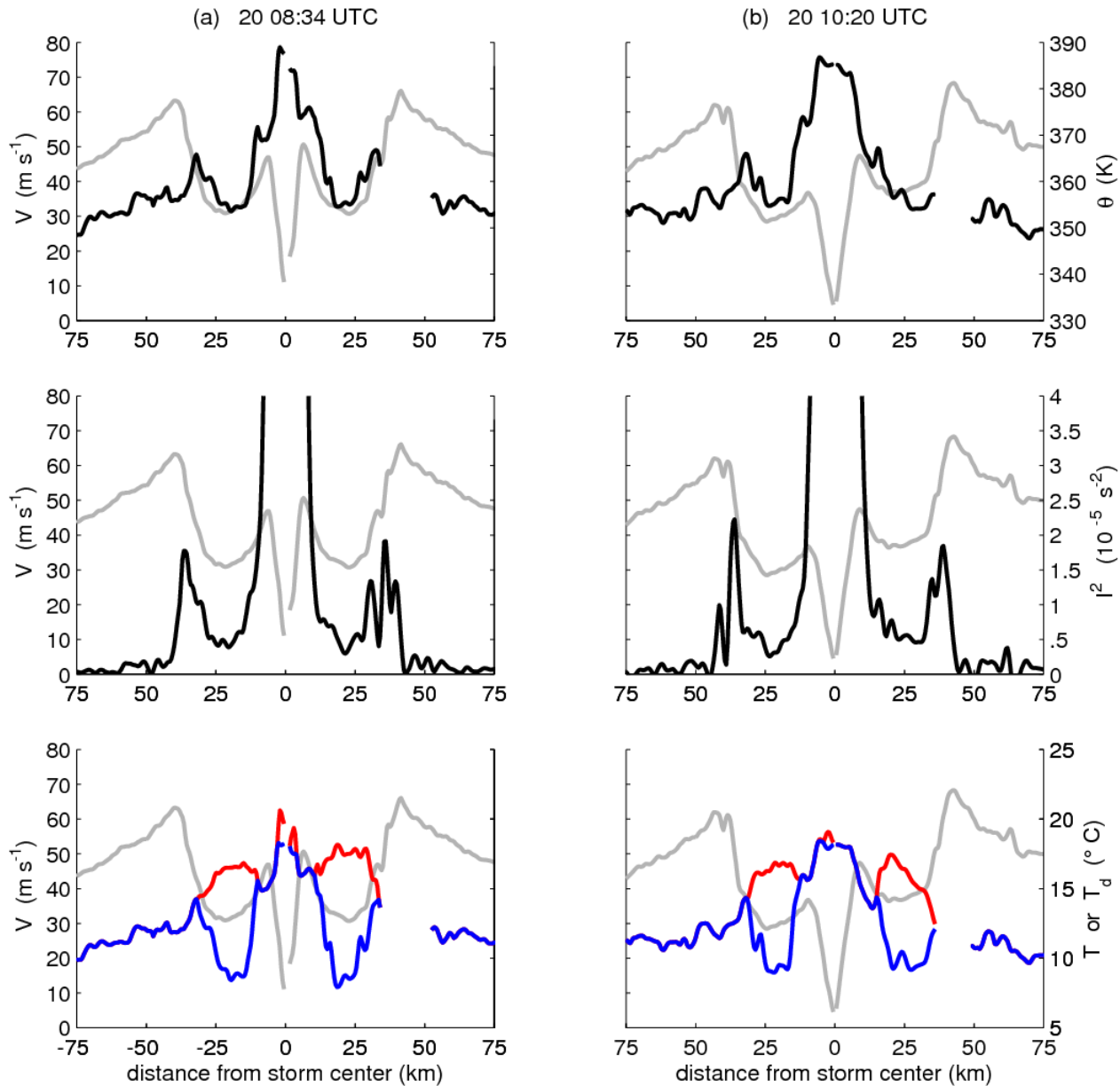


Figure 8.1 (a) Hurricane Wilma (2005) flight-level measurements along the 700 mb level taken near 0834 UTC 20 Oct. *Top*, tangential wind (gray) and θ_e (black). *Middle*, tangential wind (gray) and inertial stability (black). Inertial stability near storm center exceeds the maximum value of the y-axis. *Bottom*, temperature, dewpoint, and tangential wind appear as red, blue and gray lines respectively. A small portion of thermodynamic data from 30-50 km contained large wetting errors and were removed. (b) As in (a), but for 1020 UTC 20 Oct.

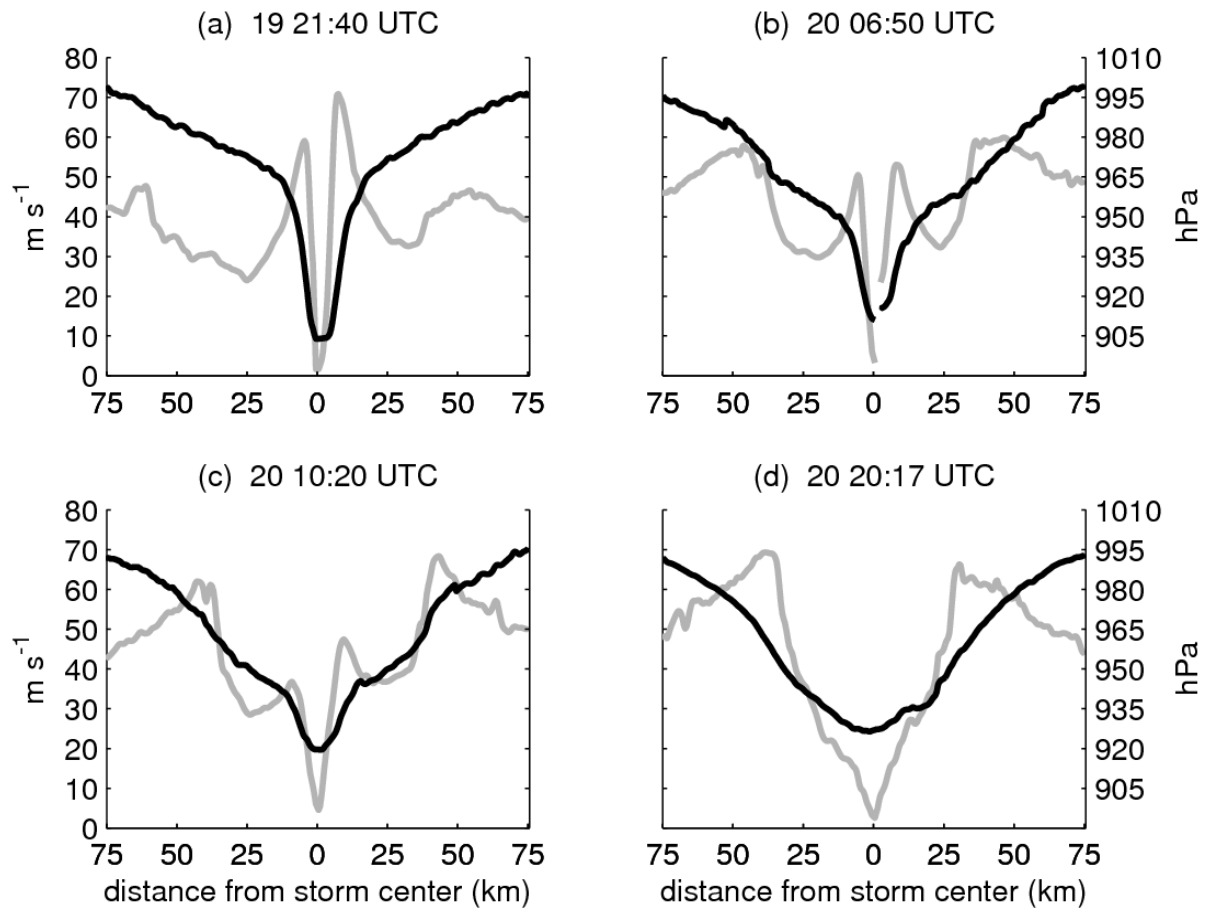


Figure 8.2 Hurricane Wilma (2005) flight-level (700 mb) tangential wind (gray line) and surface pressure (black line). The aircraft was near storm center at (a) 2140 UTC 19 Oct., (b) 0650 UTC 20 Oct., (c) 1020 UTC 20 Oct., and (d) 2017 UTC 20 Oct. As noted in the text, the actual surface pressure is likely lower than shown here.

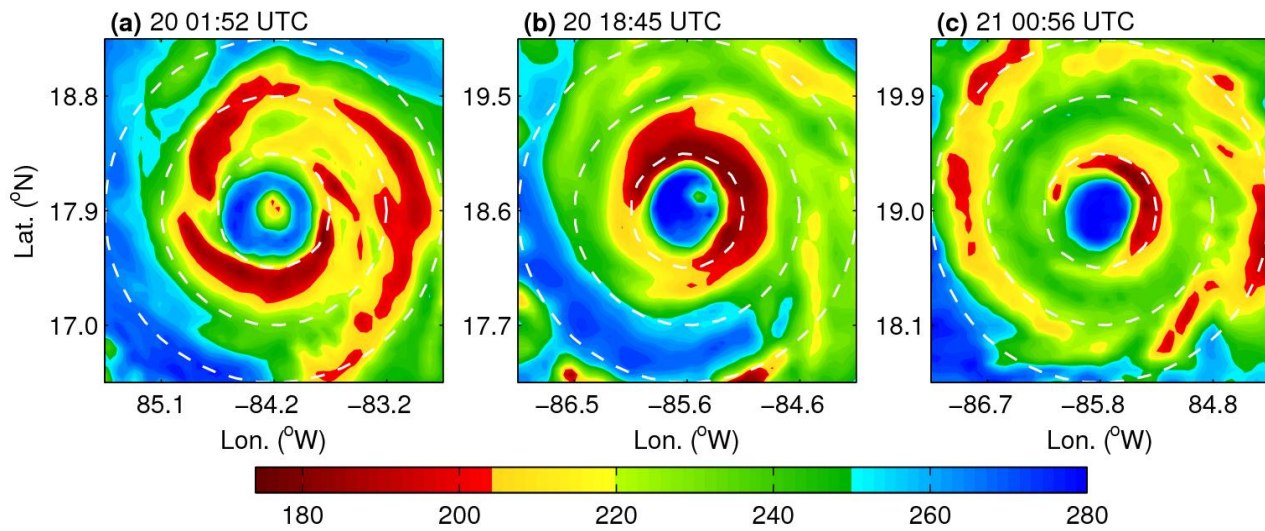


Figure 8.3 300 x 300 km storm-centered 85 GHz imagery of brightness temperatures (K) of Wilma (2005) taken at (a) 0152 UTC 20 Oct. (TRMM-TMI), (b) 1845 UTC 20 Oct. (AMSR-E), and (c) 0056 UTC 21 Oct. (TRMM-TMI). White range rings denote radial distances from storm center of 50, 100, and 150 km.

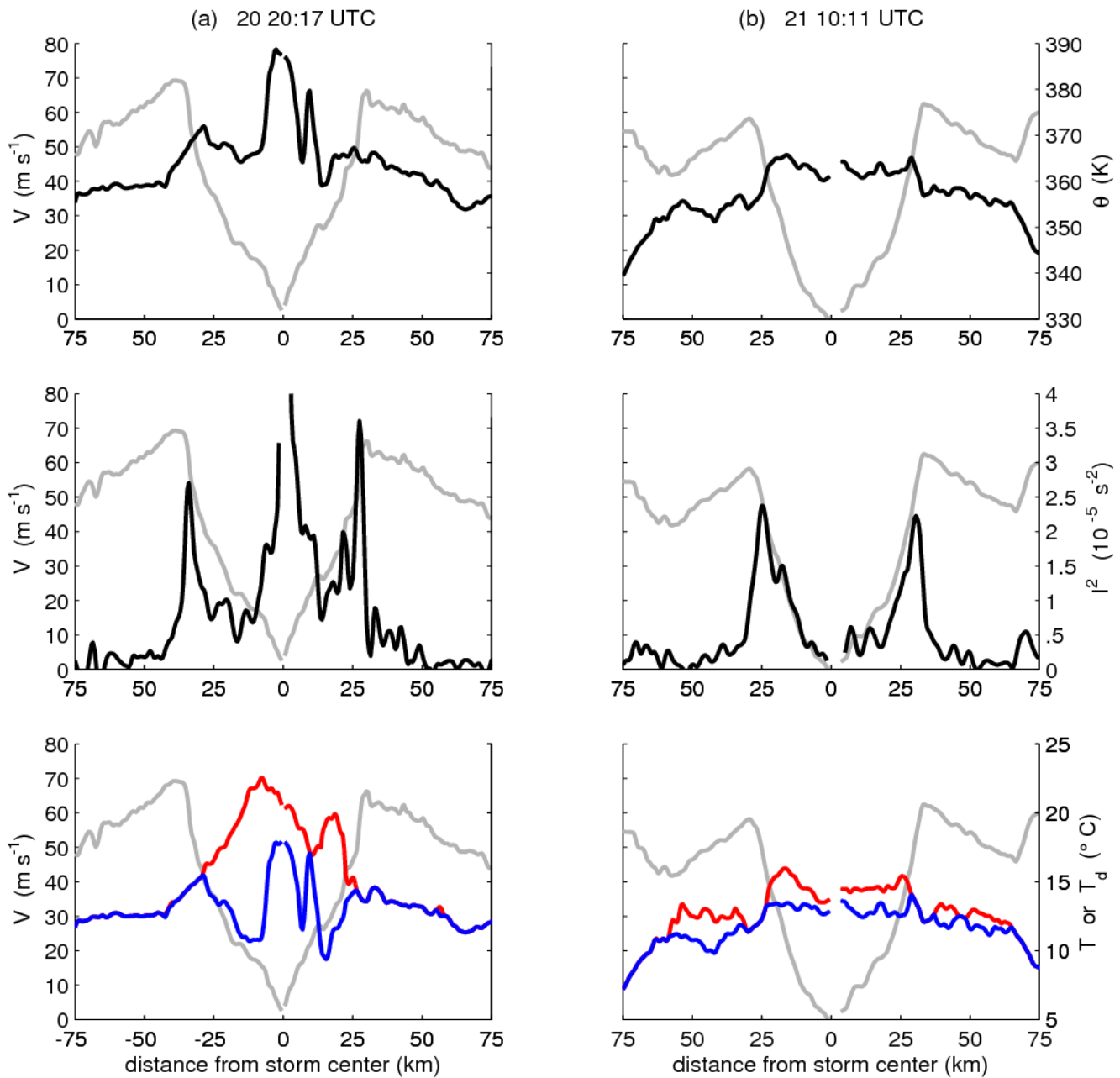


Figure 8.4 (a) As in Fig. 8.1, but for 2017 UTC 20 Oct. (b), As in Fig. 8.1, but for 1011 UTC 21 Oct.

Chapter 9 Summary and Outlook

While we have made significant progress in hurricane forecasting and warnings, we believe we have more work to do. From a scientific standpoint, the gaps in our capabilities fall into two broad categories: first, our ability to assess the current state of a hurricane and its environment (analysis), and second, our ability to predict a hurricane's future state (the forecast).

- *Max Mayfield, National Hurricane Center Director, before the Committee on Commerce, Science, and Transportation, Subcommittee on Disaster Prevention and Prediction, United States Senate, Sept 30, 2005.*

The number of published hurricane research articles has increased markedly over the last 20 years (Fig. 9.1). The research findings cover great breadth of temporal and spatial scales that include the investigation of decadal hurricane activity and the smallest of details related to a single thunderstorm in the eyewall. There have been many discoveries and successes along the way, but many processes that govern a hurricane's behavior are not well understood, especially with respect to intensity. Much of the research presented in this body of work has been steered by the operational needs of the NHC. Prior to this work, NHC forecasters had no objective guidance for predicting ERCs and they did little to their intensity and structure forecasts to account for the inner-core changes associated with ERCs. Today, as a direct result of this work, NHC forecasters now have a tool to help them forecast SEF and subsequent ERCs. A climatology of ERC intensity and structure changes serves as a baseline forecast and a discussion on the relict inner eyewall circulation helps to explain the intensity evolution and pressure-wind relations of a hurricane following an ERC.

Kossin and Sitkowski (2009) developed the first-ever objective model in diagnosing and forecasting hurricane SEF. Their model proved to be skillful and was successfully installed at the NHC for the 2010 and 2011 hurricanes seasons. Several updates have improved the model since its inception. Current work under the JHT includes optimal feature selection, invoking logistic regression methods, and examining ensemble forecasting. As the dataset increases and changes driven by improving skill scores make the model more reliable and accurate, forecasters will rely on model output more routinely.

The considerable task of developing a flight-level kinematic and thermodynamic dataset was required to investigate inner-core structure and intensity changes associated with ERCs. This dataset can also be utilized in future investigations that test a multitude of theories and concepts. The final climatology improved and expanded upon the seminal work of Willoughby (1982), which provided a description of the intensity oscillation associated with ERCs. Now, three phases have been identified that describe the intensity of the hurricane during an ERC. Reference values of intensity, wind radii, and time have been calculated and can be compared with model simulations and theoretical concepts. They also serve as a starting point for modifying hurricane forecasts when an ERC is expected. Furthermore, the inner-core microwave signature was examined during several ERCs to gain an appreciation for the presentation of the convective structure during the ERC phases. When aircraft are not present, forecasters can use microwave imagery as a proxy to the intensity behavior of the hurricane during the ERC.

The newly constructed ERC climatology presented in Chapter 6 provides the basis for the development of statistical/empirical intensity forecast tools when an ERC is imminent. Simple

statistical models have recently been constructed that input SHIPS environmental and satellite-based features and predict the amplitude and timing of ERC intensity and wind structure fluctuations, providing real-time operational objective guidance to forecasters (Kossin and Sitkowski 2012). Further improvements to this new model are likely, especially when the ERC climatology is expanded.

The documentation of the thermodynamic changes during an ERC and the exploration of the decaying inner eyewall following an ERC were also conducted as part of this research. Flight-level temperature, dewpoint, relative humidity, and θ_e were all found to increase within the inner-core over the course of an ERC, except for a decrease of mean relative humidity in the moat region. This warming in the moat is driven by subsidence from both eyewalls and, in part, because the high inertial stability of the relict inner eyewall circulation limiting subsidence near the storm center. Despite its rather insignificant appearance and size, the ramifications of the relict inner eyewall circulation were found to impact the intensification and the pressure-wind relationship of the storm. In line with the motivation of this entire work, a better understanding of this feature may lead to improved intensity forecasts.

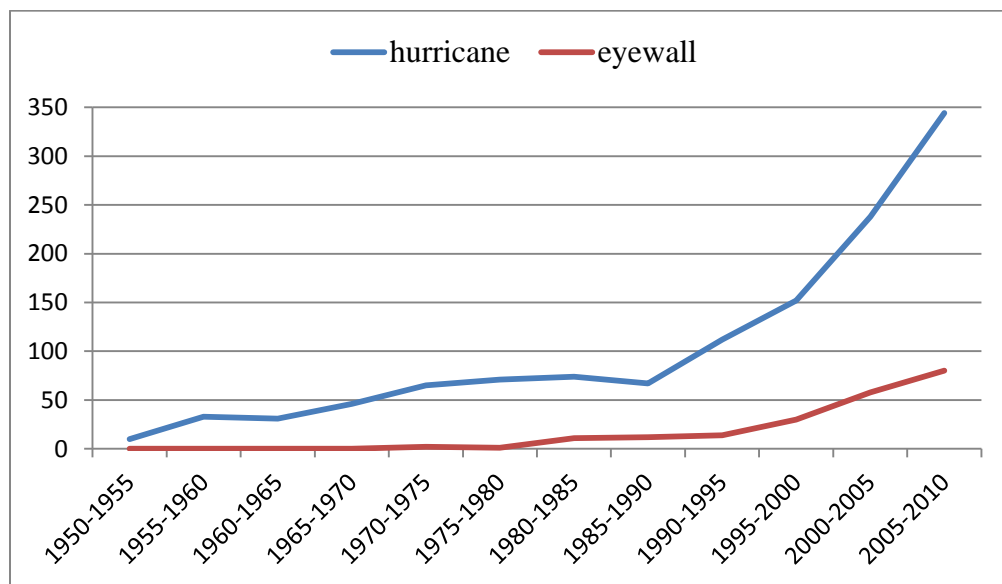


Figure 9.1 Number of times the word ‘hurricane’ and ‘eyewall’ have appeared in the abstract of American Meteorological Society journals. The counts cover 12 pentads.

Appendix

The following list of features from the 2011 SHIPS predictor file was provided by Dr. Mark DeMaria.

HEAD: header line (1st 4 letters of storm name, 2-digit year, month, day, and UTC time, maximum winds, minimum sea level pressure, and ATCF ID number (e.g., AL011982) at t=0 of current case.

TIME: Time relative to current case (hr)

VMAX: Maximum surface wind (kt)

MSLP: Minimum sea level pressure (mb)

TYPE: Storm type (0=wave, remnant low, dissipating low, 1=tropical, 2=subtropical, 3=extra-tropical). Note that the SHIPS variables are set to missing for all cases except type=1 or 2, since these are not included in the SHIPS developmental sample for estimating the model coefficients.

HIST: Storm history variable. The no. of 6 hr periods the storm max wind has been above 20, 25, ..., 120 kt.

DELV: Intensity change (kt) -12 to 0, -6 to 0, 0 to 0, 0 to 6, ... 0 to 120 hr. If the storm crosses a major land mass during the time interval, value set to 9999

INCV: Intensity change (kt) -18 to -12, -12 to -6, ... 114 to 120 hr. Set to 9999 similar to DELV for land cases.

LAT: Storm latitude (deg N)

LON: Storm longitude (deg W)

CSST: Climatological SST (deg C)

DTL: Distance to nearest major land mass (km)

RSST: Reynolds SST (deg C). Number after SST label is the age in days of the SST analysis used to estimate RSST

PHCN: Estimated ocean heat content (kJ/cm²) from climo OHC and current SST anomaly. Designed to fill in for RHCN when that is missing.

U200: 200 mb zonal wind (kt) (r=200-800 km)

U20C: Same as U200 but for r=0-500 km)

V20C: Save as U20C, but for the v component of the wind

E000: 1000 mb theta_e (r=200-800 km) (deg K)

EPOS: The average theta_e difference between a parcel lifted from the surface and its environment (200-800 km average) versus time (deg C). Only positive differences are included in the average.

ENEG: Same as EPOS, but only negative differences are included. The minus sign is not included.

EPSS: Same as EPOS, but the parcel theta_e is compared with the saturated theta_e of the environment

ENSS: Same as ENEG, but the parcel theta_e is compared with the saturated theta_e of the environment

RHLO: 850-700 mb relative humidity (%) (200-800 km)

RHMD: Same as RHLO for 700-500 mb

RHHI: Same as RHLO for 500-300 mb

PSLV: Pressure of the center of mass (mb) of the layer where storm motion best matches environmental flow (t=0 only)

Z850: 850 mb vorticity ($\text{sec}^{-1} * 10^{**7}$) (r=0-1000 km)

D200: Same as above for 200 mb divergence

REFC: Relative eddy momentum flux convergence (m/sec/day, 100-600 km avg)

PEFC: Planetary eddy momentum flux convergence (m/sec/day, 100-600 km avg)

T000: 1000 mb temperature (deg C* 10) (200-800 km average)

R000: 1000 mb relative humidity (200-800 km average)

Z000: 1000 mb height deviation (m) from the U.S. standard atmosphere

TLAT: Latitude of 850 mb vortex center in NCEP analysis (deg N)

TLON: Longitude of 850 mb vortex center in NCEP analysis (deg W)

TWAC: 0-600 km average symmetric tangential wind at 850 mb from NCEP analysis (m/sec)

TWXC: Maximum 850 mb symmetric tangential wind at 850 mb from NCEP analysis (m/sec)

V000: The tangential wind (m/sec) azimuthally averaged at r=500 km from (TLAT,TLON) If TLAT,TLON are not available, (LAT,LON) are used.

V850: Same as V000 at 850 mb

V500: Same as V000 at 500 mb

V300: Same as V000 at 300 mb

TGRD: The magnitude of the temperature gradient between 850 and 700 mb averaged from 0 to 500 km estimated from the geostrophic thermal wind ($\text{deg C per m} \cdot 10^7$)

TADV: The temperature advection between 850 and 700 mb averaged from 0 to 500 km from the geostrophic thermal wind ($\text{deg per sec} \cdot 10^6$)

PENC: Azimuthally averaged surface pressure at outer edge of vortex (mb-1000)

SHDC: Same as SHRD but with vortex removed and averaged from 0-500 km relative to 850 mb vortex center

SDDC: Heading (deg) of above shear vector

SHGC: Same as SHRG but with vortex removed and averaged from 0-500 km relative to 850 mb vortex center

DIVC: Same as D200, but centered at 850 mb vortex location

T150: 200 to 800 km area average 150 mb temperature (deg C)

T200: Same as above for 200 mb temperature (deg C)

T250: Same as above for 250 mb temperature (deg C)

SHRD: 850-200 mb shear magnitude (kt) (200-800 km)

SHTD: Heading (deg) of above shear vector

SHRS: 850-500 mb shear magnitude (kt)

SHTS: Heading of above shear vector

SHRG: Generalized 850-200 mb shear magnitude (kt) (takes into account all levels)

PENV: 200 to 800 km average surface pressure $((\text{mb}-1000) \cdot 10)$

VMPI: Maximum potential intensity from Kerry Emanuel equation (kt)

VVAV: Average (0 to 15 km) vertical velocity ($\text{m/s} \cdot 100$) of a parcel lifted from the surface where entrainment, the ice phase and the condensate weight are accounted for. Note: Moisture and temperature biases between the operational and reanalysis files make this variable inconsistent in the 2001-2007 sample, compared 2000 and before.

VMFX: Same as VVAV, but a density weighted vertical average.

VVAC: Same as VVAV but with soundings from 0-500 km with GFS vortex removed

IRXX: Same as IR00 below, but generated from other predictors (not satellite data). These should only be used to fill in for IR00 as needed.

IR00: Predictors from GOES data (not time dependent). The 17 values in this record are as follows:

- 1) Time (hr) of the GOES image, relative to this case
- 2) Average GOES ch 4 brightness temp (deg C), r=0-200 km
- 3) Stan. Dev. of GOES BT (deg C*10), r=0-200 km
- 4) Same as 2) for r=100-300 km
- 5) Same as 3) for r=100-300 km
- 6) Percent area r=50-200 km of GOES ch 4 BT < -10 C
- 7) Same as 6 for BT < -20 C
- 8) Same as 6 for BT < -30 C
- 9) Same as 6 for BT < -40 C
- 10) Same as 6 for BT < -50 C
- 11) Same as 6 for BT < -60 C
- 12) max BT from 0 to 30 km radius (deg C)
- 13) avg BT from 0 to 30 km radius (deg C)
- 14) radius of max BT (km)
- 15) min BT from 20 to 120 km radius (deg C)
- 16) avg BT from 20 to 120 km radius (deg C)
- 17) radius of min BT (km)

IRM3: Same as IR00 but at three hours before initial time

RD20: Ocean depth of the 20 deg C isotherm (m), from satellite altimetry data

RD26: Ocean depth of the 26 deg C isotherm (m) from satellite altimetry data

RHCN: Ocean heat content (KJ/cm²) from satellite altimetry data. The number after the label is the age in days of the OHC analysis used to estimate RD20, RD26 and RHCN.

LAST: The last line for this case

References

- Abarca, S. F., and K. L. Corbosiero, 2011: Secondary eyewall formation in WRF simulations of hurricanes Rita and Katrina (2005). *Geophys. Res. Lett.*, **38**, L07802, doi:10.1029/2011GL047015.
- Ashcroft, P. and F. Wentz. 2006, updated daily. *AMSR-E/Aqua L2A Global Swath Spatially-Resampled Brightness Temperatures V002*, 2002-2007. Boulder, Colorado USA: National Snow and Ice Data Center. Digital media.
- Barnes, G. M., D. P. Jorgensen, and F. D. Marks Jr., 1983: Mesoscale and convective structure of a hurricane rainband. *J. Atmos. Sci.*, **40**, 2125-2137.
- Barnes, G. M. and M. D. Powell, 1995: Evolution of the inflow boundary layer of Hurricane Gilbert (1988). *Mon. Wea. Rev.*, **123**, 2348-2368.
- Bellman, R.E. 1957. *Dynamic Programming*. Princeton University Press, Princeton, NJ.
- Beven, J. L., II, and Coauthors, 2008: Atlantic Hurricane Season of 2005. *Mon. Wea. Rev.*, **136**, 1109-1173.
- Bishop, C. M., 1995: *Neural networks for pattern recognition*. Oxford University Press, New York, NY.
- Bister, M., and K.A. Emanuel, 1998: Dissipative heating and hurricane intensity. *Meteor. Atm. Phys.*, **52**, 233-240.
- Black, M. L., and H. E. Willoughby, 1992: The concentric eyewall cycle of Hurricane Gilbert. *Mon. Wea. Rev.*, **120**, 947-957.
- Briggs, W., and D. Ruppert, 2005: Assessing the skill of yes/no predictions. *Biometrics*, **61**, 799-807.
- Briggs, W., M. Pocerlich, and D. Ruppert, 2005: Incorporating misclassification error in skill assessment. *Mon. Wea. Rev.*, **133**, 3382-3392.
- Chen, H., D.-L. Zhang, J. Carton and R. Atlas, 2011: On the Rapid Intensification of Hurricane Wilma (2005). Part I: Model Prediction and Structural Changes. *Wea. Forecasting*, **26**, 885-901. doi: 10.1175/WAF-D-11-00001.1
- Camp, J. P., and M. T. Montgomery, 2001: Hurricane maximum intensity: Past and present. *Mon. Wea. Rev.*, **129**, 1704-1717.

- Corbosiero, K. L., J. Molinari, and M. L. Black, 2005: The structure and evolution of Hurricane Elena (1985). Part I: Symmetric intensification. *Mon. Wea. Rev.*, **133**, 2905-2921.
- Croxford, M. and G. Barnes, 2002: Inner-core strength of Atlantic tropical cyclones. *Mon. Wea. Rev.*, **130**:127–139.
- DeMaria, M., and J. Kaplan, 1994: A Statistical Hurricane Intensity Prediction Scheme (SHIPS) for the Atlantic Basin. *Wea. Forecasting*, **9**, 209–220.
- DeMaria, M., and J. Kaplan, 1999: An Updated Statistical Hurricane Intensity Prediction Scheme (SHIPS) for the Atlantic and Eastern North Pacific Basins. *Wea. Forecasting*, **14**, 326–337.
- DeMaria, M., M. Mainelli, L.K. Shay, J.A. Knaff, and J. Kaplan, 2005: Further Improvements to the Statistical Hurricane Intensity Prediction Scheme (SHIPS). *Wea. Forecasting*, **20**, 531–543.
- Didlake, A. C., and R. A. Houze, 2011: Kinematics of the secondary eyewall observed in Hurricane Rita (2005). *J. Atmos. Sci.*, **68**, 1620–1636.
- Dodge, P. R. W. Burpee, and F. D. Marks Jr., 1999: The kinematic structure of a hurricane with sea level pressure less than 900 mb. *Mon. Wea. Rev.*, **127**, 987-1004.
- Domingos, P., and Pazzani, M., 1997: Beyond independence: Conditions for the optimality of the simple Bayesian classifier. *Machine Learning*, **29**, 103–130.
- Dunion, J. P., and C. S. Marron, 2008: A reexamination of the Jordan mean tropical sounding based on awareness of the Saharan Air Layer: Results from 2002. *J. Climate*, **21**, 5242–5243.
- Eastin, M. D., P. G. Black, and W. M. Gray, 2002: Flight-level thermodynamic instrument wetting errors in hurricanes. Part I: Observations. *Mon. Wea. Rev.*, **130**, 825–841.
- Elsberry, R. L., T. D. B. Lambert, and M. A. Boothe, 2007: Accuracy of Atlantic and eastern North Pacific tropical cyclone intensity forecast guidance. *Wea. Forecasting*, **22**:747–762.
- Elsner, J., and C. Schmertmann, 1994: Assessing Forecast Skill through Cross Validation. *Wea. Forecasting*, **9**, 619–624.
- Fang, J., and F. Zhang, 2011: Beta effect on the development of tropical cyclones. *Mon. Wea. Rev.*, in press.
- Fortner, L.E., 1958: Typhoon Sarah, 1956. *Bull. Amer. Meteor. Soc.*, **39**, 633–639.

- Franklin, J. L., S. J. Lord, and F. D. Marks Jr., 1988: Dropwindsonde and radar observations of the eye of Hurricane Gloria (1985). *Mon. Wea. Rev.*, **116**, 1237–1244.
- Franklin, J. L., M. L. Black, and K. Valde, 2003: GPS dropwindsonde wind profiles in hurricanes and their operational implications. *Wea. Forecasting*, **18**, 32–44.
- Franklin, J. L., R. J. Pasch, L. A. Avila, J. L. Beven II, M. B. Lawrence, S. R. Stewart, and E. S. Blake, 2006: Atlantic hurricane season of 2004. *Mon. Wea. Rev.*, **134**, 981–1025.
- Hack, J. J., and W. H. Schubert, 1986: Nonlinear response of atmospheric vortices to heating by organized cumulus convection. *J. Atmos. Sci.*, **43**, 1559–1573.
- Hand, D. J., and K. Yu, 2001: Idiot's Bayes: Not so stupid after all? *International Statistical Review*, **69**, 385–398, doi:10.2307/1403452.
- Hausman, S. A., 2001: Formulation and sensitivity analysis of a nonhydrostatic, axisymmetric tropical cyclone model. Department of Atmospheric Science Paper No. 701, Colorado State University.
- Hawkins, J. D., and M. Helveston, 2004: Tropical cyclone multi-eyewall characteristics. *Preprints 26th Conference on Hurricanes and Tropical Meteorology, Miami, FL*.
- Hawkins, J., M. Helveston, T. F. Lee, F. J. Turk, K. Richardson, C. Sampson, J. Kent, and R. Wade, 2006: Tropical cyclone multiple eyewall configurations. *Preprints, 27th Conference on Hurricanes and Tropical Meteorology, Monterey, CA*.
- Hawkins, J. D., and M. Helveston, 2008: Tropical cyclone multiple eyewall characteristics. *28th Conference on Hurricanes and Tropical Meteorology, Orlando, FL*.
- Hendricks, E. A., W. H. Schubert, R. K. Taft, H. Wang, J. P. Kossin, 2009: Life Cycles of Hurricane-Like Vorticity Rings. *J. Atmos. Sci.*, **66**, 705–722, doi:10.1175/2008JAS2820.1.
- Hendricks, E. A., and W. H. Schubert, 2010: Adiabatic rearrangement of hollow PV towers. *J. Adv. Model. Earth Syst.*, **2**, Art. #8, 19pp., doi:10.3894/JAMES.2010.2.8.
- Hill, K. A., and G. M. Lackmann, 2009: Influence of environmental humidity on tropical cyclone size. *Mon. Wea. Rev.*, **137**, 3294–3315.
- Hogsett, W., and D.-L. Zhang, 2009: Numerical simulation of Hurricane Bonnie (1998). Part III: Energetics. *J. Atmos. Sci.*, **66**, 2678–2696.
- Holland, G. J., 1980: An analytic model of the wind and pressure profiles in hurricanes. *Mon. Wea. Rev.*, **108**, 1212–1218.
- Holland, G. J., J. I. Belanger, and A. Fritz, 2010: A revised model for radial profiles of hurricane winds. *Mon. Wea. Rev.*, in press.

- Houze, R. A., Coauthors 2006: The Hurricane Rainband and Intensity Change Experiment (RAINEX): Observations and modeling of Hurricanes Katrina, Ophelia, and Rita (2005). *Bull. Amer. Meteor. Soc.*, **87**:1503–1521, doi: 10.1175/BAMS-87-11-1503.
- Houze, R. A., S. S. Chen, B. F. Smull, W.-C. Lee, and M. M. Bell, 2007: Hurricane intensity and eyewall replacement. *Science*, **315**, 1235-1239, doi:10.1126/science.1135650.
- Irish, J. L., R. T. Resio, and J. J. Ratcliff, 2008: The influence of storm size on hurricane surge. *J. Phys. Oceanogr.*, **38**, 2003-2013.
- Jarvinen, B. R., C. J. Neumann, and M. A. S. Davis, 1984: A tropical cyclone data tape for the North Atlantic basin, 1886-1983: Contents, limitations, and uses. NOAA Tech. Memo. NWS NHC 22, Miami, FL, 21 pp. [Available from National Technical Information Service, 5285 Port Royal Rd., Springfield, VA 22151].
- Jordan, C. L., 1961: Marked changes in the characteristics of the eye of intense typhoons between the deepening and filling stages. *J. Meteor.*, **18**, 779–789.
- Jordan, C. L., 1966: Surface pressure variations at coastal stations during the period of irregular motion of Hurricane Carla of 1961. *Mon. Wea. Rev.*, **94**, 454–458.
- Judt, F., and S. S. Chen, 2010: Convectively generated potential vorticity in rainbands and formation of the secondary eyewall in Hurricane Rita of 2005. *J. Atmos. Sci.*, **67**, 3581—3599.
- Kaplan, J., M. DeMaria, and J. A. Knaff, 2010: A revised tropical cyclone rapid intensification index for the Atlantic and Eastern North Pacific basins. *Wea. Forecasting*, **25**, 220-241.
- Kieu, C. Q., H. Chen, D.-L. Zhang, 2010: An examination of the pressure–wind relationship for intense tropical cyclones. *Wea. Forecasting*, **25**, 895–907, doi:10.1175/2010WAF2222344.1.
- Kimball, S. K. and M. S. Mulekar, 2004: A 15-year climatology of North Atlantic tropical cyclones. Part I: Size parameters. *J. Climate*, **17**:3555–3575.
- Knaff, J. A., J. P. Kossin, and M. DeMaria, 2003: Annular Hurricanes. *Wea. Forecasting*, **18**, 204-223.
- Knaff, J.A., and R.M. Zehr, 2007: Reexamination of tropical cyclone wind-pressure relationships. *Wea Forecasting*, **22**:1, 71–88.
- Knaff, J.A., and R.M. Zehr, 2008: Reply. *Wea. Forecasting*, **23**, 762-770, doi:10.1175/2008WAF2007086.1.

- Knapp, K. R., and J. P. Kossin, 2007: A new global tropical cyclone data set from ISCCP B1 geostationary satellite observations. *J. of App. Remote Sensing*, **1**, 013505.
- Knapp, K. R., 2008: Hurricane satellite (HURSAT) data sets: Low Earth orbit infrared and microwave data. *28th Conference on Hurricanes and Tropical Meteorology, Orlando, FL*.
- Kossin, J. P., W. H. Schubert, and M. T. Montgomery, 2000: Unstable interactions between a hurricane's primary eyewall and a secondary ring of enhanced vorticity. *J. Atmos. Sci.*, **57**, 3893–3917.
- Kossin, J. P., and M. D. Eastin, 2001: Two distinct regimes in the kinematic and thermodynamic structure of the hurricane eye and eyewall. *J. Atmos. Sci.*, **58**, 1079-1090.
- Kossin, J. P., and W. H. Schubert, 2001: Mesovortices, polygonal flow patterns, and rapid pressure falls in hurricane-like vortices. *J. Atmos. Sci.*, **58**, 2196–2209.
- Kossin, J. P., and W. H. Schubert, 2004: Mesovortices in Hurricane Isabel. *Bull. Amer. Meteor. Soc.*, **85**, 151–153, doi:10.1175/BAMS-85-2-151.
- Kossin, J. P., Coauthors 2007: Estimating hurricane wind structure in the absence of aircraft reconnaissance. *Wea. Forecasting*, **22**:89–101.
- Kossin, J. P., J. A. Knaff, H. I. Berger, D. C. Herndon, T. A. Cram, C. S. Velden, R. J. Murnane, and J. D. Hawkins, 2007b: Estimating hurricane wind structure in the absence of aircraft reconnaissance. *Wea. Forecasting*, **22**, 89–101.
- Kossin, J. P., K. R. Knapp, D. J. Vimont, R. J. Murnane, and B. A. Harper, 2007a: A globally consistent reanalysis of hurricane variability and trends. *Geophys. Res. Lett.*, **34**, L04815, doi:10.1029/2006GL028836.
- Kossin, J. P., and M. Sitkowski, 2009: An objective model for identifying secondary eyewall formation in hurricanes. *Mon. Wea. Rev.*, **137**, 876-892.
- Kossin, J. P., and M. Sitkowski, 2012: Predicting hurricane intensity and structure changes associated with eyewall replacement cycles. *Wea. Forecasting*, in press.
- Kuo, H-C., L-Y. Lin, C-P. Chang, and R. T. Williams. 2004: The formation of concentric vorticity structures in typhoons. *J. Atmos. Sci.*, **61**, 2722-2734.
- Kuo, H.-C., C.-P. Chang, Y.-T. Yang, and H.-J. Jiang, 2009: Western North Pacific typhoons with concentric eyewalls. *Mon. Wea. Rev.*, **137**, 3758-3770, doi:10.1175/2009MWR2850.1.

- Kwon, Y. C., and W. M. Frank, 2008: Dynamic instabilities of simulated hurricane-like vortices and their impacts on the core structure of hurricanes. Part II: Moist experiments. *J. Atmos. Sci.*, **65**, 106–122.
- Landsea, C. W., J. L. Franklin, C. J. McAdie, J. L. Beven, J. M. Gross, B. R. Jarvinen, R. J. Pasch, E. N. Rappaport, J. P. Dunion, and P. P. Dodge, 2004: A reanalysis of Hurricane Andrew's intensity. *Bull. Amer. Meteor. Soc.*, **85**, 1699–1712.
- Liu, Y., D-L. Zhang, and M. K. Yau, 1999: A multiscale numerical study of Hurricane Andrew (1992). Part II: Kinematics and inner-core structures. *Mon. Wea. Rev.*, **127**, 2597–2616.
- Maclay, K.S., M. DeMaria and T.H. Vonder Haar, 2008: Tropical cyclone inner core kinetic energy evolution. *Mon. Wea. Rev.*, **136**, 4882-4898, doi:10.1175/2008MWR2268.1.
- Mallen, K. J., M. T. Montgomery, and B. Wang, 2005: Reexamining the near-core radial structure of the tropical cyclone primary circulation: Implications for vortex resiliency. *J. Atmos. Sci.*, **62**, 408-425.
- Marks, F. D., Jr., P. G. Black, M. T. Montgomery, and R. W. Burpee, 2008: Structure of the eye and eyewall of Hurricane Hugo (1989). *Mon. Wea. Rev.*, **136**, 1237–1259, doi:10.1175/2007 MWR2073.1.
- Martinez, Y. H., G. Brunet, and M. K. Yau, 2010: On the dynamics of two-dimensional hurricane-like concentric rings vortex formation. *J. Atmos. Sci.*, **67**, 3253–3268.
- Martinez, Y., G. Brunet, M. K. Yau, and X. Wang, 2011: On the dynamics of concentric eyewall genesis: Space-time empirical normal mode diagnosis. *J. Atmos. Sci.*, in press.
- McNoldy, B. D., 2004: Triple eyewall in Hurricane Juliette. *Bull Amer. Meteor. Soc.*, **85**, 1663-1666.
- Molinari, J., and D. Vollaro, 1989: External influences on hurricane intensity. Part I: Outflow layer eddy angular momentum fluxes. *J. Atmos. Sci.*, **46**, 1093–1105.
- Montgomery, M. T., and R. J. Kallenbach, 1997: A theory for vortex Rossby-waves and its application to spiral bands and intensity changes in hurricane. *Quart. J. Roy. Meteor. Soc.*, **123**, 435–465.
- Muramatsu, T., 1986: Trochoidal motion of the eye of Typhoon 8019. *J. Meteor. Soc. Japan*, **64**, 259–272.
- Nolan, D. S., M. T. Montgomery, and L. D. Grasso, 2001: The wavenumber-one instability and trochoidal motion of hurricane-like vortices. *J. Atmos. Sci.*, **58**, 3243–3270.

- Nolan, D. S., Y. Moon, and D. P. Stern, 2007: Tropical cyclone intensification from asymmetric convection: Energetics and efficiency. *J. Atmos. Sci.*, **64**, 3377-3405.
- Nong, S., and K. A. Emanuel, 2003: A numerical study of the genesis of concentric eyewalls in hurricane. *Quart. J. Roy. Meteor. Soc.*, **129**, 3323–3338.
- Oda, M., M. Nakanishi, and G. Naito, 2006: Interaction of an asymmetric double vortex and trochoidal motion of a tropical cyclone with the concentric eyewall structure. *J. Atmos. Sci.*, **63**, 1069–1081, doi:10.1175/JAS3670.1.
- Ooyama, K., 1969: Numerical simulation of the life cycle of tropical cyclones. *J. Atmos. Sci.*, **26**, 3–40.
- Piech, D., and R. Hart, 2008: Atlantic reconnaissance vortex message climatology and composites and their use in characterizing eyewall cycles. *28th Conference on Hurricanes and Tropical Meteorology, Orlando, FL*.
- Powell, M. D., 1990a: Boundary layer structure and dynamics in outer hurricane rainbands. Part I: Mesoscale rainfall and kinematic structure. *Mon. Wea. Rev.*, **118**, 891-917.
- Powell, M. D., 1990b: Boundary layer structure and dynamics in outer hurricane rainbands. Part II: Downdraft modification and mixed layer recovery. *Mon. Wea. Rev.*, **118**, 918-938.
- Prieto, R., J. P. Kossin, and W. H. Schubert, 2001: Symmetrization of lopsided vorticity monopoles and offset hurricane eyes. *Q. J. R. Meteorol. Soc.*, **127**, 2307-2328.
- Qiu, X., Z.-M. Tan, and Q. Xiao, 2010: The roles of vortex Rossby waves in hurricane secondary eyewall formation. *Mon. Wea. Rev.*, **138**, 2092—2109.
- Rappin, E., M. C. Morgan, and G. Tripoli, 2011: The impact of outflow environment on tropical cyclone intensification and structure. *J. Atmos. Sci.*, **68**, 177-194, doi:10.1175/2009 JAS2970.1.
- Rozoff, C. M., W. H. Schubert, B. D. McNoldy, and J. P. Kossin, 2006: Rapid filamentation zones in intense tropical cyclones. *J. Atmos. Sci.*, **63**, 325-340.
- Rozoff, C. M., W. H. Schubert, and J. P. Kossin, 2008: Some dynamical aspects of tropical cyclone concentric eyewalls. *Q. J. R. Meteorol. Soc.*, **134**, 583-593, doi: 10.1002/qj.237.
- Rozoff, C. M., J. P. Kossin, W. H. Schubert, and P. J. Mulero, 2009: Internal control of hurricane intensity variability: The dual nature of potential vorticity mixing. *J. Atmos. Sci.*, **66**, 133–147, doi: 10.1175/2008JAS2717.1.
- Rozoff, C. M., J. P. Kossin, D. S. Nolan, F. Zhang, and J. Fang, 2011: On the efficiency of secondary eyewall formation in tropical cyclones. *Mon. Wea. Rev.*, to be submitted.

- Samsury, C. E., and E. J. Zipser, 1995: Secondary wind maxima in hurricanes: Airflow and relationship to rainbands. *Mon. Wea. Rev.*, **123**, 3502–3517.
- Schubert, W. H. and J. J. Hack, 1982: Inertial stability and tropical cyclone development. *J. Atmos. Sci.*, **39**, 1687-1697.
- Schubert, W. H., M. T. Montgomery, R. K. Taft, T. A. Guinn, S. R. Fulton, J. P. Kossin, and J. P. Edwards, 1999: Polygonal eyewalls, asymmetric eye contraction, and potential vorticity mixing in hurricanes. *J. Atmos. Sci.*, **56**, 1197–1223.
- Schubert, W. H., C. M. Rozoff, J. L. Vigh, B. D. McNoldy, and J. P. Kossin, 2007: On the distribution of subsidence in the hurricane eye. *Quart. J. Roy. Meteor. Soc.*, **133**, 595-605, doi:10.1002/qj.49.
- Shapiro, L. J., and H. E. Willoughby, 1982: The response of balanced hurricanes to local sources of heat and momentum. *J. Atmos. Sci.*, **39**, 378–394.
- Simpson, J., E. Ritchie, G. J. Holland, J. Halverson, and S. Stewart, 1997: Mesoscale interactions in tropical cyclone genesis. *Mon. Wea. Rev.*, **125**:2643–2661.
- Sitkowski, M, J. P. Kossin, C.M. Rozoff, 2011: Intensity and structure changes during eyewall replacement cycles. *Mon. Wea. Rev.*, in press, doi:10.1175/MWR-D-11-00034.1.
- Terwey, W. D., and M. T. Montgomery, 2006: Modeled secondary eyewall and spiral band dynamics. 27th Conference on Hurricanes and Tropical Meteorology, Monterey, CA.
- Terwey, W. D., and M. T. Montgomery, 2008: Secondary eyewall formation in two idealized, full-physics modeled hurricanes. *J. Geophys. Res.*, **113**, D12112, doi:10.1029/2007JD008897.
- Vigh, J. L., and W. H. Schubert, 2009: Rapid development of the tropical cyclone warm core. *J. Atmos. Sci.*, **66**, 3335-3350, doi:10.1175/2009JAS3092.1.
- Wallace, J. M. and P. V. Hobbs 2006: Atmospheric Science: an Introductory Survey, Second Edition, Academic Press, 483 pages.
- Wang, Y., 2008a: Rapid filamentation zone in a numerically simulated tropical cyclone. *J. Atmos. Sci.*, **65**, 1158—1181.
- Wang, Y., 2008b: Structure and formation of an annular hurricane simulated in a fully compressible, nonhydrostatic model-TCM4. *J. Atmos. Sci.*, **65**, 1505—1527.
- Wang, Y., 2009: How do outer spiral rainbands affect tropical cyclone structure and intensity? *J. Atmos. Sci.*, **66**, 1250—1273.

- Weatherford, C. L., and W. M. Gray, 1988a: Typhoon structure as revealed by aircraft reconnaissance. Part I: Data analysis and climatology. *Mon. Wea. Rev.*, **116**, 1032–1043.
- Weatherford, C. L., and W. M. Gray, 1988b: Typhoon structure as revealed by aircraft reconnaissance. Part II: Structural variability. *Mon. Wea. Rev.*, **116**, 1044–1056.
- Wilks, D. S., 2006: Statistical methods in the atmospheric sciences, 2nd Ed., International Geophysics Series, Vol. 91, Academic Press, 627 pp.
- Willoughby, H. E., J. A. Clos, and M. G. Shoreibah, 1982: Concentric eyewalls, secondary wind maxima, and the evolution of the hurricane vortex. *J. Atmos. Sci.*, **39**, 395–411.
- Willoughby, H. E., and M. B. Chelmon, 1982: Objective determination of hurricane tracks from aircraft observations. *Mon. Wea. Rev.*, **110**, 1298–1305.
- Willoughby, H. E., D. P. Jorgensen, R. A. Black, S. L. Rosenthal, 1985: Project STORMFURY: A Scientific Chronicle 1962–1983. *Bull. Amer. Meteor. Soc.*, **66**, 505–514.
- Willoughby, H. E., 1988: The dynamics of the tropical cyclone core. *Aust. Met. Mag.*, **36**, 183–191.
- Willoughby, H. E., 1990: Temporal changes of the primary circulation in tropical cyclones. *J. Atmos. Sci.*, **47**, 242–264.
- Willoughby, H. E., and P. G. Black, 1996: Hurricane Andrew in Florida: Dynamics of a disaster. *Bull. Amer. Meteor. Soc.*, **77**, 543–549.
- Willoughby, H. E., R. W. R. Darling, and M. E. Rahn, 2006: Parametric representation of the primary hurricane vortex. Part II: A new family of sectionally continuous profiles. *Mon. Wea. Rev.*, **134**, 1102–1120.
- Wood, V. T., L. W. White, and H. E. Willoughby, 2010: A new parametric tropical cyclone wind-profile model: Testing and verification. *29th Conference on Hurricanes and Tropical Meteorology, Tucson, AZ.*
- Wu, L., S.A. Braun, J. Halverson, and G. Heymsfield, 2006: A Numerical Study of Hurricane Erin (2001). Part I: Model Verification and Storm Evolution. *J. Atmos. Sci.*, **63**, 65–86.
- Zhang, Q.-H., Y.-H. Kuo, and S.-J. Chen, 2005: Interaction between concentric eye-walls in super typhoon Winnie (1997). *Q. J. R. Meteorol. Soc.*, **131**, 3183–3204.
- Zhang, H., 2006: On the optimality of Naïve Bayes with dependent binary features. *Pattern Recognition Letters*, **27**, 830–837.
- Zhou, X., and B. Wang, 2009: From concentric eyewall to annular hurricane: A numerical study with the cloud-resolved WRF model. *Geophys. Res. Letts.*, **36**, L03802, doi:10.1029/2008GL036854.

- Zhou, X., and B. Wang, 2011: Mechanism of concentric eyewall replacement cycles and associated intensity change. *J. Atmos. Sci.*, **68**, 972-988, doi:10.1175/2011JAS3575.1.
- Zhu, T., D.-L. Zhang, F. Weng, 2004: Numerical simulation of Hurricane Bonnie (1998). Part 1: Eyewall Evolution and intensity changes. *Mon. Wea. Rev.*, **132**, 225-241.
- Zipser, E. J., R. J. Meitin, M.A. LeMone, 1981: Mesoscale motion fields associated with a slowly moving GATE convective band. *J. Atmos. Sci.*, **38**, 1725-1750.